2017

JOURNAL OF CENTRAL EUROPEAN GREEN INNOVATION

5 (2)

Eszterházy Károly Egyetem

HUNGARY

Chief Editor / Főszerkesztő
Lehoczky Éva

Editor / Felelős szerkesztő
Fodor László

Editor assistant/ Szerkesztőségi referens
Ambrus Andrea

Chair of the Editorial Board / Szerkesztőbizottság elnöke
Liptai Kálmán, rektor

Editorial Board / Szerkesztőbizottság

Bai Attila, Debreceni Egyetem
Baranyai Zsolt, Budapesti Metropolitan Egyetem
Csörgő Tamás, MTA Wigner Fizikai Kutatóközpont, Eszterházy Károly Egyetem
Dazzi, Carmelo, University of Palermo
Dinya László, Eszterházy Károly Egyetem
Fodor László, Eszterházy Károly Egyetem
Fogarassy Csaba, Szent István Egyetem
Helgertné Szabó Ilona Eszter, Eszterházy Károly Egyetem
Horska, Elena, Slovak University of Agriculture in Nitra
Hudáková Monika, School of Economics and Management in Public Administration in Bratislava
Káposzta József, Szent István Egyetem
Kőmíves Tamás, MTA ATK Növényvédelmi Intézet
Majcieczak, Mariusz, Warsaw University of Life Sciences
Mika János, Eszterházy Károly Egyetem
Nagy Péter Tamás, Eszterházy Károly Egyetem
Neményi Miklós, Széchenyi István Egyetem
Németh Tamás, Magyar Tudományos Akadémia, Kaposvári Egyetem
Némethy Sándor, Eszterházy Károly Egyetem
Novák Tamás, Eszterházy Károly Egyetem
Noworól, Alexander, Uniwersytetu Jagiellońskiego, Krakkow
Otepka, Pavol, Slovak University of Agriculture in Nitra
Pavlik, Ivo, Mendel University in Brno
Popp József, Debreceni Egyetem
Renata, Przygodzka, University of Bialystok
Szegedi László, Eszterházy Károly Egyetem
Szlávik János, Eszterházy Károly Egyetem
Takács István, Óbudai Egyetem
Takácsné György Katalin, Óbudai Egyetem
Tomor Tamás, Eszterházy Károly Egyetem

Editorial Office / Szerkesztőség
Líceum Kiadó
3300 Eger, Eszterházy tér 1.

Publisher / Kiadó
Líceum Kiadó
3300 Eger, Eszterházy tér 1.

Responsible Publisher / Felelős kiadó
Liptai Kálmán, rektor

HU ISSN 2064-3004

2017

ELŐSZÓ

Az Eszterházy Károly Egyetem kiemelt figyelmet fordít kutatási eredményeinek, valamint innovációinak a megismertetésére mind szélesebb körben konferenciák, workshopok, nyomtatott és elektronikus folyóiratok formájában egyaránt.

Ez utóbbi megvalósításához nyújt lehetőséget az intézmény számára a TÁMOP-4.2.3-12/1/1KONV-2012-0047 „Kutatási eredmények és innovációk disszeminációja az energetikai biomassza (zöldenergia) termelés, átalakítás, hasznosítás a vidékfejlesztés és a környezeti fenntarthatóság terén a Zöld Magyarországért" program, ennek keretében indult útjára a „**Journal of Central European Green Innovation (JCEGI)**" című elektronikus folyóiratot.

Az Eszterházy Károly Egyetem kutatásainak egyik kiemelt iránya a fizika, azon belül is a nagyenergiás részecske- és magfizika egyik speciális szakterülete, a femtoszkópia, melynek fő célja a távolságmérési módszerek fejlesztése a femtométer, azaz a 10^{-15} m hosszskálákon. 1993-ban *Low-x* elnevezéssel új konferencia sorozat indult Hamburgban, a DESY (**D**eutsches **E**lektronen **SY**nchrotron, Német Elektronszinkrotron) nevű kutatóközpontban. A Low-x konferencia-sorozat célja a nagyenergiás fizika azon legfrissebb eredményeinek áttekintése egy speciális kinematikai tartományban, olyan ütközéseket vizsgálva, amelyekben az ütközések közel rugalmasak, és a relatív energiacsere igen kicsi, és emiatt ezek az ütközések különösen alkalmasak a részecske- és a magfizika kölcsönhatásainak téridőbeli vizsgálatára.

A *Low-x* konferencia sorozat bejárta szinte az egész tudományos világot. Helyszínei a következő városok voltak: Saclay (Franciaország,1994), Cambridge (Anglia, 1995), Durham (Anglia, 1996), Madrid (Spanyolország, 1997), Berlin (Németország, 1998), Tel Aviv (Izrael, 1999), Oxford (Anglia, 2000), Krakkó (Lengyelország, 2001), Antwerpen (Belgium, 2002), Nafplio (Görögország, 2003), Prága (Cseh Köztársaság, 2004), Sinaia (Románia, 2005), Lisszabon (Portugália, 2006), Helsinki (Finnország, 2007), Kréta (Görögország, 2008), Ischia (Olaszország, 2009), Kavala (Görögország, 2010) and Santiago de Compostela (Spanyolország, 2011), Paphos (Görögország, 2012), Rehovot és Eilat (Izrael, 2013), Kiotó (Japán, 2014) és Sandomierz (Lengyelország,2015). A *24. Low-x* konferencia rendezési jogát a Károly Róbert Főiskola, a Magyar Tudományos Akadémia Wigner Fizikai Kutatóközpontja és az Eötvös Lóránd Tudományegyetem kutatói nyerték el, így ennek a rendezvénynek Gyöngyös, Magyarország adhatott otthont 2016. június 6-10. között. A Low-x 2016 konferencia volt a Károly Róbert Főiskolán megrendezett utolsó tudományos rendezvény, mivel a Főiskola 2016 június 30-án jogutóddal megszűnt, átszervezéssel betagozódott az újonnan létrejött Eszterházy Károly Egyetembe. A konferenciánknak 58 résztvevője volt, akik 4 világrész 19 országából jöttek el Magyarországra, közülük 9 fiatal kutató, doktorandusz. Rendezvényünkön 5 nap alatt 57 előadás hangzott el. Kötetünk a válogatás a Low-x 2016 konferencián elhangzott tudományos eredmények közül.

A *Low-x 2016* konferencia szervezése elektronikusan történt, így a rendezvény teljes anyaga (beleértve a résztvevők listáját, az előadások anyagait, illetve a konferenciakötet elektronikus archivumát) megtalálható a konferencia honlapján:

https://indico.cern.ch/event/472823/

A Low-x 2016 konferencia kiadványának szerkesztői voltak:

Csanád Máté	*Csörgő Tamás*	*Novák Tamás*	*Royon, Christophe*
(tudományos titkár)	*(elnök)*	*(társelnök)*	*(elnök)*

A LOW-X 2016 KONRENECIA TÁMOGATÓI

Ezúton is szeretnénk köszönetet mondani támogatóinknak a segítségnyújtásukért, mely nagyban hozzájárult ahhoz, hogy a *Low-x 2016* egy valóban sikeres, inspiráló és hasznos konferencia legyen. Külön szeretnénk köszönetet mondani az alábbiaknak

- Berze Secondary/Middle School, and Berze Science Club Gyöngyös, Magyarország;
- CERN, Genf, Svájc;
- Eötvös University, Budapest, Hungary;
- Hungarian Academy of Sciences, Budapest, Magyarország;
- Károly Róbert College, Gyöngyös, Magyarország;
- OTKA, Budapest, Magyarország;
- TÁMOP 4.1.1.C-12/1/KONV-2012-0001 "KEZEK – Észak-Magyarország felsőoktatási intézményeinek együttműködése"
- TÁMOP-4.1.1.C-12/1/KONV - 2012-0012 "Zöld Energia Felsőoktatási Együttműködés"
- TÁMOP-4.2.3-12/1/1KONV-2012-0047 „Kutatási eredmények és innovációk disszeminációja…”
- Széchenyi 2020 fund by the Europan Union and the Government of Hungary;
- US Department of Energy, USA;
- MTA Wigner Fizikai Kutatóközpont, Budapest, Magyarország;
- anonim magánvállalkozások Gyöngyös környékéről, Magyarországról;
- anonim magánszemélyek Gyöngyös környékéről, Magyarországról.

Ez a lista a konferenciakötet zárásakor készült.

INTRODUCTION

Eszterházy Károly University pays a special attention to disseminate its research results and innovations increasingly and as widely as reasonably possible. These results are presented in conferences and workshops as well as published in printed and electronic journals.

The dissemination of our results in the field of rese and innovation is aided by the TÁMOP-4.2.3-12/1/1KONV-2012-0047 program "dissemination of research results and innovations in the field of biomass energy (green energy) production, transformation and utilization in the field of rural development and environmental sustainability for a Green Hungary". This program provides the framework and background in which the electronic version of the "**Journal of Central European Green Innovation**" has been launched.

One of the highlighted research direction of the Eszterházy Károly University is focussing on physics, in particular on a special area of high energy particle and nuclear physics, called femtoscopy. The main goal of this field is to develop methods to precisely measure distances on the femtometer or 10^{-15} m length-scales. In 1993, a new conference series called *Low-x* was started in the research center DESY (from **D**eutsches **E**lektronen **Sy**nchrotron, located Hamburg, Germany). The goal of the Low-x conference series was to review the annual progress in high energy physics in a special kinematic range, investigating the elastic or nearly elastic high energy collisions, where the relative energy transfer to the internal excitations of the colliding particles is small compared to the total energy of the collisions. Due to this particular kinematics, the Low-x conferences include topics that deal with methods to measure or determine spatial distributions inside the colliding particles or nuclei.

By now, the *Low-x* conference series travelled almost all over the world. The conference locations included the following cities: Saclay (France,1994), Cambridge (England, 1995), Durham (England, 1996), Madrid (Spain, 1997), Berlin (Germany, 1998), Tel Aviv (Israel, 1999), Oxford (England, 2000), Cracow (Poland, 2001), Antwerp (Belgium, 2002), Nafplio (Greece, 2003), Prague (Czech Republic, 2004), Sinaia (Romania, 2005), Lisbon (Portugal, 2006), Helsinki (Finnland, 2007), Crete (Greece, 2008), Ischia (Italy, 2009), Kavala (Greece, 2010) and Santiago de Compostela (Spain, 2011), Paphos (Greece, 2012), Rehovot and Eilat (Israel, 2013), Kyoto (Japan, 2014) and Sandomierz (Poland, 2015). The right to organize the *24th Low-x* conference has been awarded to a consortium of researchers from the Károly Róbert University College (the legal predecessor of the current Eszterházy Károly University, formed by re-organization on July 1, 2016), the Wigner Research Centre of Physics of the Hungarian Academy of Sciences, the Eötvös Lóránd University. Thus the 24th Low-x meeting was organized in the city of Gyöngyös, Hungary, between June 6 – 10, 2016. This meeting attracted 58 participants from 19 countries of 4 continents, including 9 young researchers or PhD students. During 5 days, we have listened to 57 scientific presentations.

This proceedings includes selected results from the talks that were presented at the *Low-x 2016* meeting. The organization of the *Low-x 2016* conference was almost fully electronic, and all the conference materials (including list of participants, transparencies of the talks and an electronic version of the proceedings) are archived at the web-page of the meeting:

https://indico.cern.ch/event/472823/

This Special Topics on High Energy Physics volume of the electronic journal JCEGI, including the proceedings of Low-x 2016 has been edited by the Low-x 2016 Organizers:

M. Csanád	*T. Csörgő*	*T. Novák*	*Ch. Royon*
(scientific secretary, LOC)	*(chair, LOC)*	*(co-chair, LOC)*	*(chair, IAC)*

SUPPORTERS OF LOW-X 2016

We would like to sincerely thank for the various contributions from our supporters and sponsors, that helped us to organize *Low-x 2016* as a gateway to knowledge and to create an inspiring and useful, successful meeting in Gyöngyös, Hungary. In particular, we would like to express our gratitude to:

- Berze Secondary/Middle School, and Berze Science Club Gyöngyös, Hungary;
- CERN, Geneva, Switzerland;
- Eötvös University, Budapest, Hungary;
- Hungarian Academy of Sciences, Budapest, Hungary;
- Károly Róbert College, Gyöngyös, Hungary;
- OTKA, Hungarian National Science Fund, Budapest, Hungary
- TÁMOP 4.1.1.C-12/1/KONV-2012-0001 "KEZEK – Észak-Magyarország felsőoktatási intézményeinek együttműködése"
- TÁMOP-4.1.1.C-12/1/KONV - 2012-0012 "Zöld Energia Felsőoktatási Együttműködés"
- TÁMOP-4.2.3-12/1/1KONV-2012-0047 „Kutatási eredmények és innovációk disszeminációja…”
- Széchenyi 2020 fund by the Europan Union and the Government of Hungary;
- US Department of Energy, USA;
- Wigner Research Centre, Hungarian Academy of Sciences, Budapest, Hungary;
- an anonymous private company from Gyöngyös region, Hungary;
- some anonymous private persons from Gyöngyös region, Hungary.

This is the full list of *Low-x 2016* supporters and patrons, at the time of finalizing the proceedings of the conference.

A Low-x 2016 konferencia volt a Károly Róbert Főiskolán megrendezett utolsó tudományos rendezvény, mivel a Főiskola 2016 június 30-án jogutóddal megszűnt, átszervezéssel betagozódott az újonnan létrejött Eszterházy Károly Egyetembe.

TARTALOMJEGYZÉK / TABLE OF CONTENTS

TANULMÁNYOK – SCIENTIFIC PAPERS

Diffractive processes at the LHC within kt -factorization approach

Marta Łuszczak[1], Antoni Szczurek[1,2]

[1]University of Rzeszów, PL-35-959 Rzeszów, Poland
[2]Institute of Nuclear Physics PAN, PL-31-342 Kraków, Poland

August 9, 2017

Abstract

We discuss the single diffractive production of $c\bar{c}$ pairs and charmed mesons at the LHC. In addition to standard collinear approach, for a first time we propose a k_t-factorization approach to the diffractive processes. The transverse momentum dependent (the unintegrated diffractive parton distributions) in proton are obtained with the help of the Kimber-Martin-Ryskin prescription where collinear diffractive PDFs are used as input. In this calculation the transverse momentum of the pomeron is neglected with respect to transverse momentum of partons entering the hard process. The results of the new approach are compared with those of the standard collinear one. Significantly larger cross sections are obtained in the k_t-factorization approach where some part of higher-order effects is effectively included. Some correlation observables, like azimuthal angle correlation between c and $\bar{c}$, and $c\bar{c}$ pair transverse momentum distribution were obtained for the first time.

1 Introduction

Diffractive hadronic processes were studied theoretically in the so-called resolved pomeron model [1]. This model, previously used to describe deep-inelastic diffractive processes must be corrected for absorption effects related to hadron-hadron interactions. In theoretical models this effect is taken into account approximately by multiplying the diffractive cross section calculated using HERA diffractive PDFs

by a kinematics independent factor called the gap survival probability – S_G. Two theoretical groups specialize in calculating such probabilities [2, 3].

In this study we consider diffractive production of charm for which rather large cross section at the LHC are expected, even within the leading-order (LO) collinear approach [4]. On the other hand, it was shown that for the inclusive non-diffractive charm production the LO collinear approach is a rather poor approximation and higher-order corrections are crucial. Contrary, the k_t-factorization approach, which effectively includes higher-order effects, gives a good description of the LHC data for inclusive charm production at $\sqrt{s} = 7$ TeV (see *e.g.* Ref. [5]). This strongly suggests that application of the k_t-factorization approach to diffractive charm production is useful. Besides, the dipole approach is also often used to calculate cross section for diffractive processes. However, as we discussed in Ref. [6], it gives only a small fraction of the diffractive cross section for the charm production. This presentation is based on our recent study presented in [7]. Here we present only results at the quark/antiquark level.

2 A sketch of the theoretical formalism

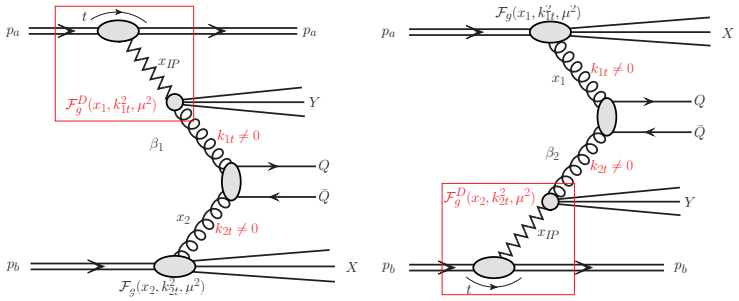

Figure 1: A diagrammatic representation for single-diffractive production of heavy quark pairs within the k_t-factorization resolved pomeron approach.

A sketch of the theoretical formalism is shown in Fig. 1. Here, extension of the standard resolved pomeron model based on the LO collinear approach by adopting a framework of the k_t-factorization is proposed as an effective way to include higher-order corrections. According to this model the cross section for a single-diffractive production of charm quark-antiquark pair, for both considered diagrams (left and right panel of Fig. 1), can be written as:

$$d\sigma^{SD(a)}(p_a p_b \to p_a c\bar{c}\, XY) = \int dx_1 \frac{d^2k_{1t}}{\pi} dx_2 \frac{d^2k_{2t}}{\pi}\, d\hat{\sigma}(g^* g^* \to c\bar{c}) \times \mathcal{F}_g^D(x_1, k_{1t}^2, \mu^2) \cdot \mathcal{F}_g(x_2, k_{2t}^2, \mu^2), \quad (1)$$

$$d\sigma^{SD(b)}(p_a p_b \to c\bar{c} p_b\, XY) = \int dx_1 \frac{d^2k_{1t}}{\pi} dx_2 \frac{d^2k_{2t}}{\pi}\, d\hat{\sigma}(g^* g^* \to c\bar{c}) \times \mathcal{F}_g(x_1, k_{1t}^2, \mu^2) \cdot \mathcal{F}_g^D(x_2, k_{2t}^2, \mu^2), \quad (2)$$

where $\mathcal{F}_g(x, k_t^2, \mu^2)$ are the "conventional" unintegrated (k_t-dependent) gluon distributions (UGDFs) in the proton and $\mathcal{F}_g^D(x, k_t^2, \mu^2)$ are their diffractive counter-

parts. The latter can be interpreted as a probability of finding a gluon with longitudinal momentum fraction x and transverse momentums k_t at the factorization scale μ^2 assuming that the proton which lost a momentum fraction x_{IP} remains intact.

Details of our new calculations can be found in Ref. [7].

3 Selected results

First, we show some selected examples of the results of the k_T-factorization calculation in Fig. 2. In Fig. 2 we show rapidity (left panel) and transverse momentum (right panel) distribution of c quarks (antiquarks) for single diffractive production at $\sqrt{s} = 13$ TeV. Distributions calculated within the LO collinear factorization (black long-dashed lines) and for the k_t-factorization approach (red solid lines) are shown separately. We see significant differences between results of the both approaches, that are consistent with the conclusions from similar studies of standard non-diffractive charm production (see *e.g.* Ref. [5]). Here we confirm that the higher-order corrections are very important also for the diffractive production of charm quarks.

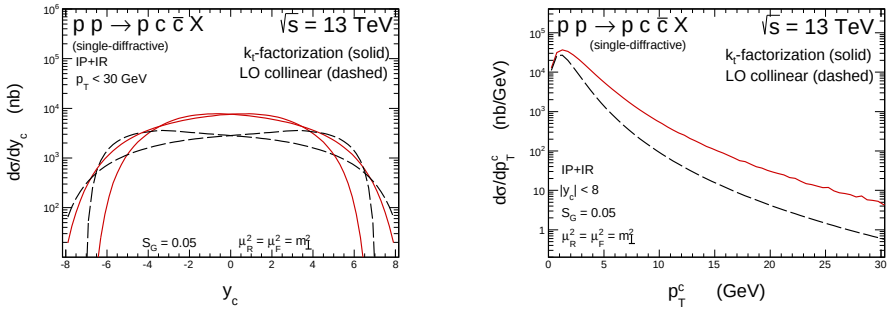

Figure 2: Rapidity (left panel) and transverse momentum (right panel) distributions of c quarks (antiquarks) for a single-diffractive production at $\sqrt{s} = 13$ TeV. Components of the $g(IP)$ - $g(p)$, $g(p)$ - $g(IP)$, $g(IR)$ - $g(p)$, $g(p)$ - $g(IR)$ mechanisms are shown.

Figure 3 shows the differential cross section as a function of $\log_{10}(x)$ where x is defined as the longitudinal momentum fraction of proton carried by the gluon from non-diffractive side (left panel) or as the longitudinal momentum fraction of proton carried by the diffractive gluon emitted from pomeron/reggeon on diffractive side (right panel). In the case of non-diffractive gluon (left panel) we see that for extremely small values of x the LO collinear predictions strongly exceed the ones of the k_t-factorization. This effect also affects the rapidity spectra in the very forward/backward regions (see Fig. 2) and is partially related to a very poor theoretical control of the collinear PDFs in the range of x below 10^{-5}.

In Fig. 4 we show again the rapidity (left panel) and transverse momentum (right panel) distributions of c quarks (antiquarks) calculated in the k_t-factorization approach. Here contributions from the pomeron and the reggeon exchanges are shown separately. The estimated sub-leading reggeon contribution is of similar size as the one of the leading pomeron. In the single-diffractive case the maxima of rapidity distributions for $g(IP)$ - $g(p)$ and $g(p)$ - $g(IP)$ (or $g(IR)$ - $g(p)$ and $g(p)$ - $g(IR)$)

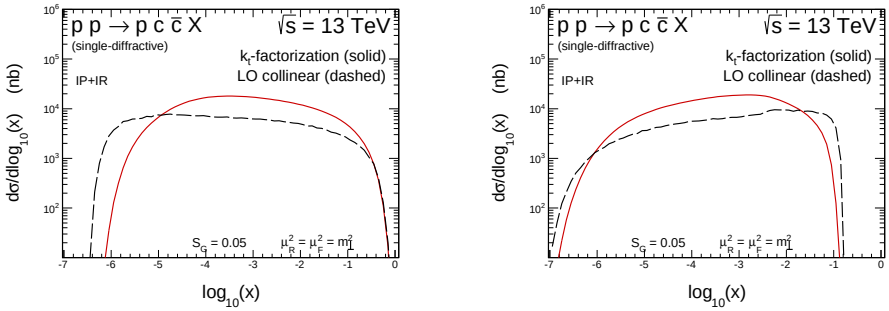

Figure 3: The differential cross section as a function of $\log_{10}(x)$ with x being the non-diffractive gluon longitudinal momentum fraction (left panel) and the diffractive gluon longitudinal momentum fraction with respect to the proton (right panel) for single-diffractive production at $\sqrt{s} = 13$ TeV. Results for the LO collinear (black long-dashed) and the k_t-factorization (red solid) approaches are compared.

mechanisms are shifted to forward and backward rapidities with respect to the non-diffractive case. This is related to the upper limit on diffractive gluon longitudinal momentum fraction ($x \leq x_{IP}$).

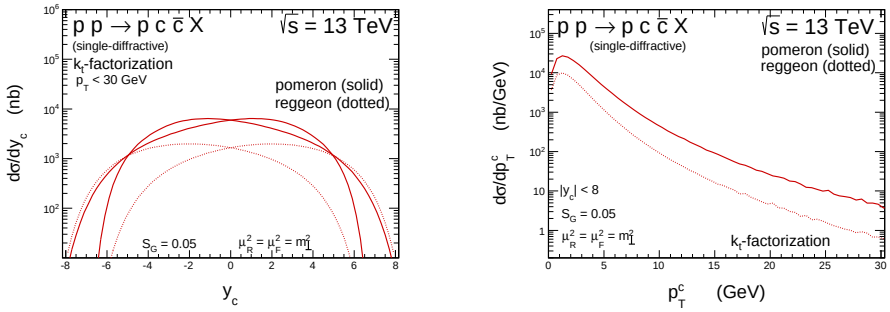

Figure 4: Rapidity (left panel) and transverse momentum (right panel) distributions of c quarks (antiquarks) for single-diffractive production at $\sqrt{s} = 13$ TeV calculated with the k_t-factorization approach. Contributions of the $g(IP)$ - $g(p)$, $g(p)$ - $g(IP)$, $g(IR)$ - $g(p)$, $g(p)$ - $g(IR)$ mechanisms are shown separately.

The correlation observables cannot be calculated within the LO collinear factorization but can be directly obtained in the k_t-factorization approach. The distribution of azimuthal angle $\varphi_{c\bar{c}}$ between c quarks and $\bar{c}$ antiquarks is shown in the left panel of Fig. 5. The $c\bar{c}$ pair transverse momentum distribution $p_T^{c\bar{c}} = |\vec{p_t^{\,c}} + \vec{p_t^{\,\bar{c}}}|$ is shown in the right panel. Results of the full phase-space calculations illustrate that the quarks and antiquarks in the $c\bar{c}$ pair are almost uncorrelated in the azimuthal angle between them and are often produced in the configuration with quite large pair transverse momenta.

Figures 6 and 7 show the double differential cross sections as a functions of transverse momenta of incoming gluons (k_{1T} and k_{2T}) and transverse momenta of outgoing c and $\bar{c}$ quarks (p_{1T} and p_{2T}), respectively. We observe quite large incident gluon transverse momenta. The major part of the cross section is concentrated in the region of small k_t's of both gluons but long tails are present. Transverse

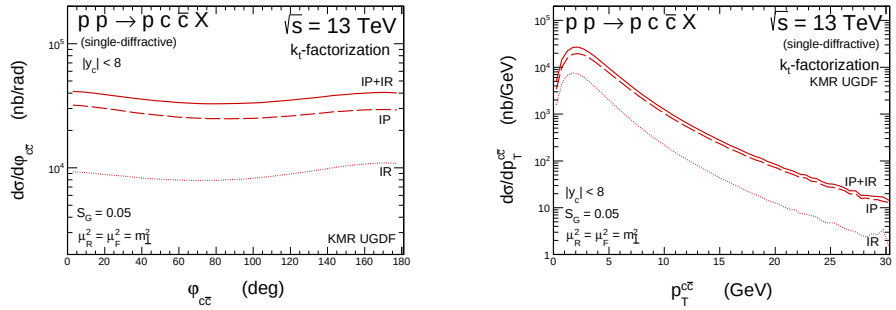

Figure 5: The distribution in $\phi_{c\bar{c}}$ (left panel) and distribution in $p_T^{c\bar{c}}$ (right panel) in the k_t-factorization approach at $\sqrt{s} = 13$ TeV.

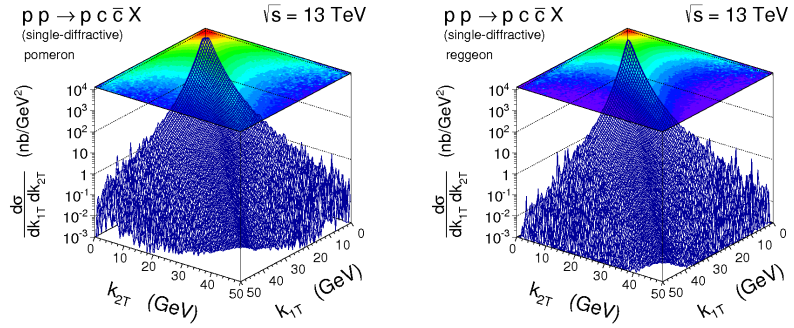

Figure 6: Double differential cross sections as a function of initial gluons transverse momenta k_{1T} and k_{2T} for single-diffractive production of charm at $\sqrt{s} = 13$ TeV. The left and right panels correspond to the pomeron and reggeon exchange mechanisms, respectively.

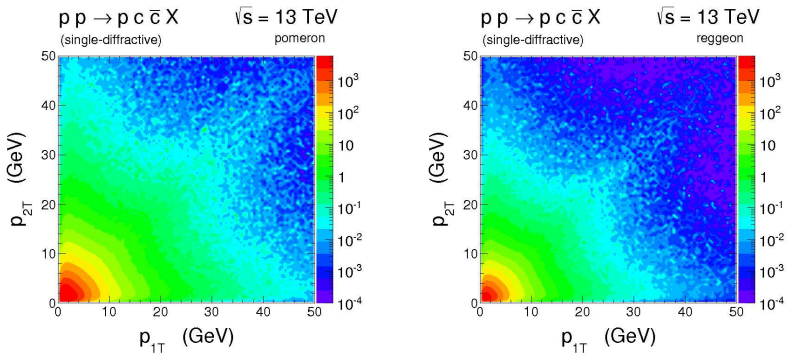

Figure 7: Double differential cross sections as a function of transverse momenta of outgoing c quark p_{1T} and outgoing $\bar{c}$ antiquark p_{2T} for single-diffractive production of charm at $\sqrt{s} = 13$ TeV. The left and right panels correspond to the pomeron and reggeon exchange mechanisms, respectively.

momenta of the outgoing particles are not balanced as they were in the case of the LO collinear approximation.

4 Conclusions

Charm production is a good example where the higher-order effects are very important. For the inclusive charm production we have shown that these effects can be effectively included in the k_t-factorization approach [5]. In our approach we decided to use the so-called KMR method to calculate unintegrated diffractive gluon distribution (UDGD). Having obtained the UDGD we have performed calculations of several single-particle and correlation distributions. In general, the k_t-factorization approach leads to larger cross sections. However, the K-factor is strongly dependent on phase space point. Some correlation observables, like azimuthal angle correlation between c and $\bar{c}$, and $c\bar{c}$ pair transverse momentum distributions were obtained in [7] for the first time.

Acknowledgments

This work was partially supported by the Polish National Science Centre grant DEC-2013/09/D/ST2/03724 as well as by the Centre for Innovation and Transfer of Natural Sciences and Engineering Knowledge in Rzeszów.

References

[1] G. Ingelman, P.E. Schlein, Phys. Lett. B **152**, 256 (1985).

[2] V. A. Khoze, A. D. Martin and M. G. Ryskin, Eur. Phys. J. C **18**, 167 (2000) [hep-ph/0007359].

[3] E. Gotsman, E. Levin, U. Maor, E. Naftali and A. Prygarin, arXiv:0511060 [hep-ph].

[4] M. Luszczak, R. Maciula and A. Szczurek, Phys. Rev. D **91** (2015) no.5, 054024 [arXiv:1412.3132 [hep-ph]].

[5] R. Maciula and A. Szczurek, Phys. Rev. D **87**, 094022 (2013) [arXiv:1301.3033 [hep-ph]].

[6] M. Luszczak, W. Schafer and A. Szczurek, Phys. Lett. B **729** (2014) 15 [arXiv:1305.4727 [hep-ph]].

[7] M. Luszczak, R. Maciula, A. Szczurek and M. Trzebinski, arXiv:1606.06528 [hep-ph].

New exact solutions of hydrodynamics for rehadronizing fireballs with lattice QCD equation of state

T. Csörgő[1,2] and G. Kasza[3],

[1]Wigner RCP, H - 1525 Budapest 114, P.O.Box 49, Hungary,
[2]EKU KRC, H-3200 Gyöngyös, Mátrai út 36, Hungary,
[3]Eötvös Loránd University, H-1117 Budapest, Pázmány P. s. 1/A, Hungary

August 9, 2017

Abstract

We describe fireballs that rehadronize from a perfectly fluid quark matter to a chemically frozen, multi-component hadron gas. In the hydrodynamics of these fireballs, we utilize the lattice QCD equation of state, however, we also apply non-relativistic kinematics for simplicity and clarity. Two new classes of exact, analytic solutions of fireball hydrodynamics are presented: the first class describes triaxially expanding, non-rotating ellipsoidal fireballs, while the second class of exact solutions corresponds to spheroidally symmetric, rotating fireballs. In both classes of solutions, we find evidence for a secondary explosion, that happens just after hadrochemical freeze-out. A realistic, linear mass scaling of the slope parameters of the single particle spectra of various hadronic species is obtained analytically, as well as an also realistic, linear mass scaling of the inverse of the squared HBT radius parameters of the Bose-Einstein correlation functions.

1 Introduction

The equations of hydrodynamics contain no internal scale, and the applications of hydrodynamics range from the largest, cosmological distances to the

smallest experimentally accessible distances. Hydrodynamical type of equations characterize the time evolution of our Universe that started from a Big Bang. Hydrodynamics is also applied to the study of the time evolution on the smallest, femtometer distances, where the Little Bangs of high energy heavy ion collisions also create hydrodynamically evolving fireballs. Our Universe about 14 billion years after the Big Bang expands with an approximately spherically symmetric Hubble flow. The hadronic final states of heavy ion collisions about a few times 10^{-23} sec after the Little Bangs expand with directional Hubble flows and possibly also with significant angular momentum, due to the typically non-central nature of high energy heavy ion collisions.

As early as in 1978, Zimányi, Bondorf and Garpman found an exact solution of hydrodynamics that described a non-relativistic, finite fireball with a Hubble flow, expanding to vacuum [1]. Keeping the spherical symmetry and the Hubble flow profile, the Zimányi-Bondorf-Garpman solution was generalized in 1998, after 20 years, to a spatially Gaussian density and a spatially homogeneous temperature profile, while maintaining the same equations for the time evolution of the scales as in the Zimányi-Bondorf-Garpman solution [2]. Soon it was realized that these solutions can be generalized to arbitrary, but matching temperature and density profile functions, while still maintaining spherical [3] symmetry. Within a few years, the first, spherically symmetric solutions were successfully generalized to include ellipsoidal symmetries [4, 5]. About at the same time, the Gaussian solutions were utilized to evaluate the final state hadronic observables and their relation to the initial conditions, as it turned out that these solutions provided exact results for the single particle spectra, elliptic and higher order flows, as well as for the Bose-Einstein correlation functions [6]. In this class of solutions, a non-vanishing initial angular momentum and the corresponding rotation of the expanding fireball can also be taken into account analytically. The first exact solution of rotating fireball hydrodynamics was found in the relativistic kinematic region [7]. This spheroidally symmetric, relativistic rotating solution was subsequently generalized to the non-relativistic kinematic domain [8, 9, 10], including not only spheroidally but also triaxially expanding and rotating solutions of fireball hydrodynamics. In these solutions, the hadronic final state was typically containing only a given type of particle with mass m, and the observables like the slope parameters of the single particle spectra were investigated as a function of this mass, considered to be a parameter of the solution.

This conference presentation details the first steps towards generalizing some of the recently found expanding as well as rotating, spheroidally and ellipsoidally symmetric solutions of fireball hydrodynamics [8, 9, 10] to a more realistic hadro-chemical and kinetic freeze-out stage. These final states contain a mixture of hadrons, with different hadronic masses denoted as m_i. In this work, we explore two classes of exact solutions. The first class describes triaxially expanding, non-rotating ellipsoidal fireballs, the second class of exact solutions corresponds to spheroidally symmetric, rotating fireballs. In both classes of exact solutions, lattice QCD calculations provide the data for the equations of state. This allows us to take into account the temperature dependence of the speed of sound, following refs. [6, 11]. After rehadronization, a subsequent hadrochemical freeze-out is shown to have a significant effect on the expansion dynamics, corresponding to a secondary explosion, which is seen in in both classes of exact solutions. The properties and the criteria of such a secondary

explosion are clarified here in an exact and analytic manner.

2 Perfect fluid hydrodynamics for two different stages

Experimental results of the NA44 [12] as well as the PHENIX collaborations [13] indicate, for example, that the so called inverse slope parameter of the single particle spectra is a linear function of the mass m of the observed hadrons:

$$T = T_f + m\langle u_t\rangle^2, \tag{1}$$

where $\langle u_t\rangle$ stands for the average radial flow and the freeze-out temperature is denoted by T_f. This relationship has been derived even for non-central heavy ion collisions in ref. [6], taking into account a chemically frozen, *single component* hadronic matter (HM). However, the experimental data were taken in heavy ion collisions where actually several different kind of hadrons are produced simultaneously. If we introduce an index "i" to distinguish the different particle types in a multi-component hadron gas, then the experimental data indicate that the slope parameters depend on the particle type only through the mass m_i of particle type i, but the radial flow $\langle u_t\rangle$ and the kinetic freeze-out temperature T_f are both independent of the type of the particles:

$$T_i = T_f + m_i\langle u_t\rangle^2. \tag{2}$$

In this work, we analytically derive these relations, for a fireball of a strongly interacting Quark Gluon Plasma that hadronizes to a *multi-component,* chemically frozen hadronic matter or HM.

The basic equations of perfect fluid hydrodynamics are given by the continuity and the Euler equation together with the energy equation, corresponding to local conservation of entropy, momentum and energy. In the strongly coupled Quark-Gluon Plasma, also called as perfect fluid of Quark Matter or QM, and at vanishing baryochemical potential, the number of quarks, anti-quarks and gluons is not conserved individually, only the local conservation of entropy drives the expansion. However, at a certain temperature various hadrons are produced due to rehadronization from a QM and we assume in this manuscript that the inelastic reactions that may transform one hadron to another are negligible, so we study here the scenario that corresponds to a chemically frozen, multi-component Hadronic Matter (HM). In this chemically frozen, multi-component HM phase the number of each type of hadrons is locally conserved.

The equations of motion for these two different forms of matter are summarized in Table 1. These equations generalize the equations of motion for a chemically frozen, *single component* hadronic matter equations of (13-16) of ref. [8] to the case of the chemically frozen, *multi-component* scenario of HM. The local momentum and energy conservation, as well as the entropy conservation is valid in both phases, but in the HM phase, local continuity equations are also obeyed for all hadronic species. We utilize the $\epsilon = \kappa p$ equation of state (EoS), where $\kappa \equiv \kappa(T)$ is a temperature dependent function, that is directly taken from lattice QCD calculations of ref. [14]. We note that in Table 1 the energy equations are rewritten for the temperature field. We also note that due to the additional local conservation laws in the HM phase the coefficient of the

co-moving time derivative of the temperature field changes in the temperature equation in Table 1. It turnes out that this leads to a dynamical effect, a modification for the time evolution of the temperature. This modification corresponds to a secondary explosion that starts at the chemical freeze-out temperature T_{chem}.

QM $(T_i \geq T \geq T_{chem})$	**HM** $(T_{chem} > T \geq T_f)$
$\partial_t \sigma + \nabla (\sigma \mathbf{v}) = 0$	$\partial_t n_i + \nabla (n_i \mathbf{v}) = 0, \quad \forall i$
$T\sigma (\partial_t + \mathbf{v}\nabla) \mathbf{v} = -\nabla p$	$\sum_i m_i n_i (\partial_t + \mathbf{v}\nabla) \mathbf{v} = -\nabla p$
$\frac{1+\kappa}{T} \left[\frac{d}{dT} \frac{\kappa T}{1+\kappa} \right] (\partial_t + \mathbf{v}\nabla) T + \nabla \mathbf{v} = 0$	$\frac{1}{T} \left[\frac{d(\kappa T)}{dT} \right] (\partial_t + \mathbf{v}\nabla) T + \nabla \mathbf{v} = 0$
$p = \sigma T/(1+\kappa)$	$p = \sum_i p_i = T \sum_i n_i$

Table 1: Hydrodynamical equations for strongly interacting Quark Gluon Plasma or Quark Matter (QM) and chemically frozen, multi-component Hadronic Matter (HM) that drive the fireball expansion from the initial temperature T_i to the chemical freeze-out temperature $(T_i \geq T \geq T_{chem})$. This chemical freeze-out temperature T_{chem} characterizes both hadronization and simultaneous hadrochemical freeze-out in the present manuscript. Below this chemical freeze-out temperature but above the kinetic freeze-out temperature $(T_{chem} > T \geq T_f)$, a multi-component hadronic matter is characterized by local conservation laws for each hadronic species.

In Table 1, $\sigma \equiv \sigma(\mathbf{r}, t)$ stands for the entropy density, $n_i \equiv n_i(\mathbf{r}, t)$ is the density of hadron type i that is locally conserved in the HM phase, the velocity field is denoted by $\mathbf{v} \equiv \mathbf{v}(\mathbf{r}, t)$, while $p \equiv p(\mathbf{r}, t)$ stands for the pressure, and $T \equiv T(\mathbf{r}, t)$ for the temperature field, and the mass of hadron type i is denoted as m_i.

As discussed in ref. [8], these equations were derived in the non-relativistic limit of the equations of relativistic hydrodynamics, assuming that the entalphy density (that characterizes the inertia of the motion for pressure gradients) is dominated by the entropy density above the chemical freeze-out temperature, while it is dominated by the mass terms of the hadrons at lower temperatures:

$$\varepsilon + p = \sum_i \mu_i n_i + T\sigma, \tag{3}$$

$$\varepsilon + p \approx T\sigma, \qquad (T_i \geq T \geq T_{chem}), \tag{4}$$

$$\varepsilon + p \approx \sum_i m_i n_i \qquad (T_{chem} > T \geq T_f). \tag{5}$$

The dynamical equations, summarized in Table 1, can be solved if the usual initial and freeze-out conditions as well as the chemical freeze-out conditions are given. In the present work, we characterize these conditions by the initial temperature T_i, the chemical freeze-out temperature T_{chem} and by the kinetic freeze-out temperature T_f.

In this manuscript, we also assume that the initial temperature distribution is locally homogeneous, and its value is given by a coordinate independent T_i value at the initial time $t_i = 0$, and we also assume that the HM freezes

out at a locally homogeneous freeze-out temperature T_f. In addition to these usual initial and final boundary conditions, in these solutions we also have to specify a matching boundary conditions that specifies the transition from QM to HM, which we characterize by the locally homogeneous chemical freeze-out temperature T_{chem}.

We suppose that rehadronization happens almost simultaneously with the hadrochemical freeze-out at the time $t = t_c$, and at this temperature the local velocity fields transfer smoothly:

$$T_B(t_c) = T_A(t_c) = T_{chem}, \quad (6)$$

$$\mathbf{v}_B(t_c, \mathbf{r}) = \mathbf{v}_A(t_c, \mathbf{r}). \quad (7)$$

The medium before the rehadronization is in the QM phase, its parameters are indicated by B that stands for Before. After the rehadronization, we use the A index, it indexes the medium that is converted to the HM phase. We follow Landau's proposal, who suggested that at the time of rehadronization a conversion takes place between entropy density and particle density [15]. Therefore we assume that

$$\frac{\sigma(\mathbf{r}, t_c)}{\sigma(\mathbf{r} = 0, t_c)} = \frac{n_i(\mathbf{r}, t)}{n_i(\mathbf{r} = 0, t_c)}. \quad (8)$$

We look for parametric solutions of the hydrodynamical equations, summarized in Table 1, and we assume that the principal axes of a triaxially expanding, ellipsoidal fireball are be given by $X \equiv X(t)$, $Y \equiv Y(t)$ and $Z \equiv Z(t)$ that functions depend only on the time t.

In this manuscript, we discuss two classes of parametric, exact solutions of fireball hydrodynamics. The first class is a triaxial, non-rotating class of solutions, while the second class corresponds to a spheroidally symmetric, rotating class of exact solutions of fireball hydrodynamics. In the triaxial case, all the principal axis (X, Y, Z) can be different, but the initial angular velocity ω_0 has to vanish. For the rotating solutions of fireball hydrodynamics with non-vanishing initial angular velocity, we assume spheroidal symmmetry and introduce the notation $X(t) = Y(t) = R(t)$.

All of the scale functions (X, Y, Z) as well as R are continuous at t_c, and it turns out that we can follow the lines of derivations described in refs. [5, 8, 9] even for an QM that rehadronizes to a HM, without introducing a particle species dependence of the scale parameters (X, Y, Z) after the rehadronization. The details of these calculations are not given here, but the main results are summarized in Table 2 for a tri-axially expanding, non-rotating ellipsoidal fireball, and Table 3 for a spheroidal, rotating and expanding fireball. These results indicate that the rather complicated partial differential equations that govern the dynamics of the fireball expansion can be solved exactly, when the hydrodynamical fields are given in terms of the scale parameters of the solutions. Thus these solutions are parametric solutions, the scale parameters (X, Y, Z) satisfy a system of coupled and non-linear but ordinary differential equations, listed also in Tables 2 and 3. These differential equations can be readily solved with currently available numerical packages like MATHEMATICA or MATLAB .

For a triaxially expanding ellipsoid, the volume of the fireball is given by that of a 3d Gaussian with widths X, Y and Z:

$$V(t) = (2\pi)^{3/2} XYZ, \quad (9)$$

QM ($T_i \geq T \geq T_{chem}$)	**HM** ($T_{chem} > T \geq T_f$)
$\mathbf{v} = (\frac{\dot{X}}{X} r_x, \frac{\dot{Y}}{Y} r_y, \frac{\dot{Z}}{Z} r_z)$	$\mathbf{v} = (\frac{\dot{X}}{X} r_x, \frac{\dot{Y}}{Y} r_y, \frac{\dot{Z}}{Z} r_z)$
$\sigma = \sigma_0 \frac{V_0}{V} \exp\left(-\frac{r_x^2}{2X^2} - \frac{r_y^2}{2Y^2} - \frac{r_z^2}{2Z^2}\right)$	$n_i = n_{i,c} \frac{V_c}{V} \exp\left(-\frac{r_x^2}{2X^2} - \frac{r_y^2}{2Y^2} - \frac{r_z^2}{2Z^2}\right)$
$(1+\kappa)\left[\frac{d}{dT}\frac{\kappa T}{1+\kappa}\right]\frac{\dot{T}}{T} + \frac{\dot{V}}{V} = 0$	$\frac{d(\kappa T)}{dT}\frac{\dot{T}}{T} + \frac{\dot{V}}{V} = 0$
$X\ddot{X} = Y\ddot{Y} = Z\ddot{Z} = \frac{1}{1+\kappa(T)}$	$X\ddot{X} = Y\ddot{Y} = Z\ddot{Z} = \frac{T}{\langle m \rangle}$

Table 2: Parametric solution of fireball hydrodynamics for a tri-axially expanding, non-rotating ellipsoidal fireball, where the volume V and the average mass $\langle m \rangle$ are defined by eqs. (9) and (12). The first two rows give the parametric form of the density and the velocity fields. Note that in these solutions, the corresponding temperature field is homogeneous, $T(t, \mathbf{r}) \equiv T(t)$. The time evolution of the temperature is determined by an ordinary differential equation, that depends on the Equation of State through the function $\kappa \equiv \kappa(T)$ which for a spatially homogeneous temperature field is a function of time only, $\kappa \equiv \kappa(T(t))$. The acceleration of the scales X, Y, Z is driven also by the equation of state, but on the QM side the value of the constant of proportionality, $\frac{1}{1+\kappa(T)}$ is in general different from the value of constant of proportionality in the HM phase, $\frac{T}{\langle m \rangle}$.

QM ($T_i \geq T \geq T_{chem}$)	**HM** ($T_{chem} > T \geq T_f$)
$\mathbf{v} = (\frac{\dot{R}}{R} r_x - \omega r_y, \frac{\dot{R}}{R} r_y + \omega r_x, \frac{\dot{Z}}{Z} r_z)$	$\mathbf{v} = (\frac{\dot{R}}{R} r_x - \omega r_y, \frac{\dot{R}}{R} r_y + \omega r_x, \frac{\dot{Z}}{Z} r_z)$
$\sigma = \sigma_0 \frac{V_0}{V} \exp\left(-\frac{r_x^2}{2R^2} - \frac{r_y^2}{2R^2} - \frac{r_z^2}{2Z^2}\right)$	$n_i = n_{i,c} \frac{V_c}{V} \exp\left(-\frac{r_x^2}{2R^2} - \frac{r_y^2}{2R^2} - \frac{r_z^2}{2Z^2}\right)$
$(1+\kappa)\left[\frac{d}{dT}\frac{\kappa T}{1+\kappa}\right]\frac{\dot{T}}{T} + \frac{\dot{V}}{V} = 0$	$\frac{d(\kappa T)}{dT}\frac{\dot{T}}{T} + \frac{\dot{V}}{V} = 0$
$R\ddot{R} - R^2\omega^2 = Z\ddot{Z} = \frac{1}{1+\kappa(T)}$	$R\ddot{R} - R^2\omega^2 = Z\ddot{Z} = \frac{T}{\langle m \rangle}$

Table 3: Parametric solution of fireball hydrodynamics for a spheroidally expanding, and rotating fireball. Notation is the similar to that of Table 2, but the volume V is defined by eq. (10) and the time evolution of the angular velocity ω is given by eq. (11).

while for a spheroidally expanding ellipsoid, $X = Y = R$ and the volume is given by

$$V(t) = (2\pi)^{3/2} R^2 Z. \tag{10}$$

In the considered class of exact, rotating spheroidal solution the angular velocity is driven by the radial expansion as follows:

$$\omega(t) = \omega_0 \frac{R_0^2}{R(t)^2}. \tag{11}$$

In this expression ω_0 and R_0 are the initial values of the corresponding functions at the initial time t_0. As the equations of motion for the scales are indepenent from the type of particle i in the HM phase, it is easy to see that the fireball expands collectively to the vacuum, for all particle types i.

Instead of the mass m of a single type of particle in the dynamical equations of a *single component*, chemically frozen HM phase, the average mass $\langle m \rangle$ appears in the dynamics of a *multi-component*, chemically frozen HM phase. The typical value for $\langle m \rangle$ 200 GeV Au+Au collisions at RHIC is given approximately [16] as

$$\langle m \rangle = \frac{\sum\limits_i m_i n_{i,c}}{\sum\limits_i n_{i,c}} \approx 280\, MeV. \tag{12}$$

The same analysis [16] indicated chemical freeze-out temperatures in the range of T_{chem} 150−170 MeV. At the chemical freeze-out ($T \approx T_{chem}$), the acceleration changes due to the change of the coefficients that determine $\ddot{X}X$ and similar quantities. To quantify this, we evaluate the right hand side of the acceleration equations at T_{chem}, both in the QM and in the HM phases, using the lattice QCD equation of state, and we find the following relation:

$$\frac{1}{1+\kappa(T_{chem})} \simeq 0.11 - 0.15 < \frac{T_{chem}}{\langle m \rangle} \simeq 0.55 - 0.63. \tag{13}$$

This inequality is thus valid in a broad range of T_{chem}, independently from the actual value of the chemical freeze-out temperature, if this is varied in the reasonable range of $150 < T_{chem} < 175$ MeV [16].

As a consequence, the acceleration of the scales (X, Y, Z) starts to *increase* as the temperature cools just below T_{chem}, for any reasonable value of T_{chem}, not due to the change of the pressure but due to the change of the dynamical equations, that include new conservation laws. This increased acceleration leads to a secondary explosion of the medium, which starts just after the conversion from quark matter to the chemically frozen hadronic matter.

A novel feature of the secondary explosion is that actually this happens at temperatures where the $\kappa = \varepsilon/p$ ratio is close to its maximum in lattice QCD calculations, hence the corresponding speed of sound is nearly minimal. This temperature is usually called the “softest point" of the equation of state, and it is usually associated with a slowing down of the transverse flows, see for example the exact solutions of T. S. Biró for a first order phase transition of a massless gas of quarks and gluons to a massless pion gas [17, 18]. In particular if the pressure could become a constant during a first order phase transition, its gradiends would approach vanishing values, hence the acceleration terms would vanish. However, when we take into account a lattice QCD equation of

state, that lacks a first order phase transition at small baryochemical potentials, the pressure gradients do not vanish. Furthermore, at T_{chem}, additional local hadronic conservation laws start to play a role and modify the dynamics. As a consequence of inequality in eq. (13), instead of slowing down, the expansion starts actually to accelerate faster at T_{chem}, as compared to the case when hadronization and hadrochemical freeze-out does not happen!

Another novel and rather surprising feature of this secondary explosion is related to the relative position of the chemical freeze-out to the softest point of the lQCD Equation of State. If the chemical freeze-out temperature T_{chem} is less than $T_{max} \approx 151$ MeV, the temperature where $d\kappa/dT(T = T_{max}) = 0$, this second explosion generated by the hadrochemical freeze-out leads to *faster expansion* as well as *slower cooling*, as compared to an expansion where hadrochemical freeze-out does not happen. This is a rather unusual scenario, as normally faster expansion leads to faster cooling. Such a more usual behaviour is described by the same equations if $T_{chem} > T_{max} = 151$ MeV. As this is the expected range for the chemical freeze-out temperatures [16], we expect that when the secondary, hadrochemical explosion happens, and the fireball starts to expand faster, the cooling of the temperature as a function of time actually becomes also faster.

3 Observables

The observables for a single-component hadronic matter (HM) were already evaluated in refs. [4] and [9]. In this manuscript we present the generalization of these earlier results for the multi-component hadronic matter scenario. The results are summmarized in Tables 4 and 5, corresponding to the solutions in Table 2 and 3, respectively. These results summarize only some of the key, the selected hadronic observables, such as the inverse slope parameters and the HBT-radii. The relation of these key observables to the single particle spectra, elliptic or higher order flows or to the Bose-Einstein correlation functions is the same, as in refs. [6, 9], respectively. In these calculations, the freeze-out temperature is denoted by T_f and subscript f indicates quantities that are evaluated at the time of the kinetic feeze-out.

The inverse slopes and the squared inverse HBT-radii are linear functions of m_i. Recent experimental results of for example the PHENIX collaboration correspond well to these linear relations [19]. As these data were taken in high energy heavy ion collisions, where the hadronic final state contains a mixture of various hadrons (referred to as the multi-component Hadronic Matter scenario), it is a non-trivial result that such simple replacement rules: $m \to \langle m \rangle$ in the dynamical equations and $m \to m_i$ in the observables can be utilized to obtain the new exact solutions of the hydrodynamical equations and the evaluation of the obsverables.

4 A new parametrization for lattice QCD EoS

In the earlier sections of this manuscript we presented the transition of a Quark Matter to Hadronic Matter that contained a mixture of various hadrons. These solutions, however, were limited by the assumption of a homogeneous ini-

HM (one kind of hadron only, with mass m)	**HM** (mixture of various hadrons, with masses m_i)
$T_x = T_f + m\dot{X_f}^2$ $T_y = T_f + m\dot{Y_f}^2$ $T_z = T_f + m\dot{Z_f}^2$	$T_{x,i} = T_f + m_i\dot{X_f}^2$ $T_{y,i} = T_f + m_i\dot{Y_f}^2$ $T_{z,i} = T_f + m_i\dot{Z_f}^2$
$R_x^{-2} = X_f^{-2}\left[1 + \frac{m}{T_f}\dot{X}_f^2\right]$ $R_y^{-2} = Y_f^{-2}\left[1 + \frac{m}{T_f}\dot{Y}_f^2\right]$ $R_z^{-2} = Z_f^{-2}\left[1 + \frac{m}{T_f}\dot{Z}_f^2\right]$	$R_{x,i}^{-2} = X_f^{-2}\left[1 + \frac{m_i}{T_f}\dot{X}_f^2\right]$ $R_{y,i}^{-2} = Y_f^{-2}\left[1 + \frac{m_i}{T_f}\dot{Y}_f^2\right]$ $R_{z,i}^{-2} = Z_f^{-2}\left[1 + \frac{m_i}{T_f}\dot{Z}_f^2\right]$

Table 4: Inverse slope parameters for a single component and a multi-component hadronic matter as well as HBT-radii for a triaxially expanding, non-rotating, ellipsoidal fireball, corresponding to the hydrodynamical solution in Table 2. The relation to the single particle spectra and Bose-Einstein correlation functions is the same, as in ref. [6], but instead of the mass m of a single kind of hadron for each hadronic species i their mass m_i appears in the observables.

tial temperature profile. In this section we prepare the ground for new solutions where the initial temperature and density profile may be inhomogeneous.

Recently, ref. [8] explored new, exact, parametric solutions of non-relativistic, rotating fireballs, using a lattice QCD equation of state, similarly to our previous studies, but using a single mass m in the hadron gas phase. That work explored two kinds of exact solutions: the first class of solutions had homogeneous temperature profiles, where the local temperature was a function of time only, $T \equiv T(t)$. That class of solutions were generalized to the multi-component hadronic matter in the previous sections of this manuscript. The second class of solutions in ref. [8] allowed for inhomogeneous temperature profiles if the density profiles had a corresponding, matching shape. This second class of solutions was obtained for a special equation of state, where the $\kappa(T) \equiv \kappa_c$ function was a temperature independent constant. We are not interested here in this scenario, as the lattice QCD Equation of State indicates that $\kappa = \varepsilon/p$ is not a temperature independent constant. However, in a footnote of ref. [8], a third class of solutions was also mentioned, noting that solutions exist also for the case of inhomogeneous temperature profiles also in the case of a temperature dependent $\kappa(T)$ functions, if a special differential equation is statisfied by $\kappa(T)$ functions, however, this class was not investigated in detail.

Here we follow up that line of research by demonstrating that the lattice QCD equation of state can be parameterized by $\kappa(T)$ functions that allow for exact solutions of fireball hydrodynamics with inhomogeneous temperature profiles. The criteria to find such hydrodynamical solutions is that the coefficient of the logarithmic comoving derivative of the temperature fields be a constant both in the QM and in the HM phase, as detailed below.

From the temperature equation for high temperatures ($T_i \geq T \geq T_{chem}$), corresponding to the dynamical equations that describe the evolution of QM in Table 1, this criteria leads to the following constraint on the possible shape of the $\kappa(T)$ function:

HM (single component, with mass m)	**HM** (multi-component, with masses m_i)
$T_x = T_f + m\left(\dot{R_f}^2 + \omega_f^2 R_f^2\right)$ $T_y = T_f + m\left(\dot{R_f}^2 + \omega_f^2 R_f^2\right)$ $T_z = T_f + m\dot{Z_f}^2$	$T_{x,i} = T_f + m_i\left(\dot{R_f}^2 + \omega_f^2 R_f^2\right)$ $T_{y,i} = T_f + m_i\left(\dot{R_f}^2 + \omega_f^2 R_f^2\right)$ $T_{z,i} = T_f + m_i\dot{Z_f}^2$
$R_x^{-2} = R_f^{-2}\left[1 + \frac{m}{T_f}\left(\dot{R}_f^2 + R_f^2\omega_f^2\right)\right]$ $R_y^{-2} = R_f^{-2}\left[1 + \frac{m}{T_f}\left(\dot{R}_f^2 + R_f^2\omega_f^2\right)\right]$ $R_z^{-2} = Z_f^{-2}\left[1 + \frac{m}{T_f}\dot{Z}_f^2\right]$	$R_{x,i}^{-2} = R_f^{-2}\left[1 + \frac{m_i}{T_f}\left(\dot{R}_f^2 + R_f^2\omega_f^2\right)\right]$ $R_{y,i}^{-2} = R_f^{-2}\left[1 + \frac{m_i}{T_f}\left(\dot{R}_f^2 + R_f^2\omega_f^2\right)\right]$ $R_{z,i}^{-2} = Z_f^{-2}\left[1 + \frac{m_i}{T_f}\dot{Z}_f^2\right]$

Table 5: Inverse slope parameters for a single component and a multi-component hadronic matter as well as HBT-radii for a rotating and expanding spheroidal fireball, corresponding to the hydrodynamical solution in Table 3. The relation to the single particle spectra and Bose-Einstein correlation functions is the same, as in ref. [9], but the results for the single component hadron mass are generalized for the multi-component scenario. The new results can be obtained simply, with the help of an $m \to m_i$ replacement .

$$\frac{d}{dT}\left[\frac{T\kappa(T)}{1+\kappa(T)}\right] = \frac{\kappa_Q}{1+\kappa(T)}, \qquad (T \geq T_{chem}), \tag{14}$$

where $\kappa_Q = \lim_{T\to\infty}\kappa(T)$ stands for the high temperature limit of the $\kappa(T)$ function.

As the coefficient of the temperature equation in Table 1 is modified at lower temperatures ($T_{chem} > T > T_f$), corresponding to a multi-component, chemically frozen Hadronic Matter, in this temperature range a modified constraint is obtained for the $\kappa(T)$ function:

$$\frac{d}{dT}\left[T\kappa(T)\right] = \frac{\kappa_c T_c - \kappa_f T_f}{T_c - T_f}. \qquad (T_{chem} > T \geq T_f), \tag{15}$$

where $T_c = T_{chem} = 175 MeV$ corresponds to the upper limit of the chemical freeze-out temperatures obtained from experimental data on particle ratios in $\sqrt{s_{NN}}$ = 200 GeV Au+Au collisions at RHIC [16]. In the above equations, we have assumed that at the kinetic freeze-out the non-relativistic ideal gas approximation can be used i.e. $\kappa_f = \kappa(T_f) = 3/2$, however higher values of κ_f can also be used if one intends to match lattice QCD calculations at lower temperatures closely. In any case, after freeze-out we assume that hadrons propagate to the detectors with free streaming and post kinetic freeze-out their energy density to pressure ratio thus decreases or jumps to the value of 3/2.

For the QM phase the analytic solution of the constraint (14) is

$$\kappa_{QM}(T) = \frac{\kappa_Q\left(\frac{T}{T_c}\right)^{1+\kappa_Q} + \frac{\kappa_c - \kappa_Q}{\kappa_c + 1}}{\left(\frac{T}{T_c}\right)^{1+\kappa_Q} - \frac{\kappa_c - \kappa_Q}{\kappa_c + 1}}, \tag{16}$$

and in this function κ_c stands for $\kappa(T_c)$. For the HM phase, the solution to

the constraint of eq. (15) yields the following form for $\kappa(T)$:

$$\kappa_{HM}(T) = \frac{\kappa_c T_c - \kappa_f T_f}{T_c - T_f} - \frac{\kappa_c - \kappa_f}{T_c - T_f}\frac{T_c T_f}{T}. \quad (17)$$

These solutions are matched at the critical temperature $T_c = 175$ MeV and we have assumed that the chemical freeze-out temperature is the same as the critical temperature, $T_{chem} = T_c$. We made fits to simulated data from lattice QCD [14] using κ_Q as a fitting parameter, for $T_c = 175$ MeV fixed and using various values of the kinetic freeze-out temperature T_f. The quality of these fits is summarized in Table 6 and on Figure 1.

In the QM phase, a satisfactory fit is found, as indicated by the red curve and summarized also in Table 6. We could also obtain reasonably good fits in the HM range of temperatures, however, with some constaints on the possible value of the kinetic freeze-out temperature T_f: A reasonable value of the freeze-out temperature is the pion mass, $T_f \approx 140$ MeV (continuous, blue line) but in this case κ falls down too steeply with temperature due to our additional requirement of $\kappa(T_f) = 3/2$ and it is reflected very well by the unsatisfactory confidence level of this fit. However, fits with freeze-out temperature $T_f \leq 100$ MeV and $\kappa(T_f) = 3/2$ are statistically acceptable.

Curves	χ^2/NDF	CL [%]
lQCD parametrization	0.12/5	> 99.9
$\kappa_Q = 3.833$	6.48/4	16.6
$T_f = 140\ MeV$	86.56/6	$1.6{\cdot}10^{-14}$
$T_f = 100\ MeV$	7.71/6	26.0

Table 6: Confidence levels of parametrizations of the lattice QCD Equation of State, for various values of the freeze-out temperature T_f. Note that in these parameterizations, $\kappa(T_f) = 3/2$, so at freeze-out a non-interacting, ideal gas equation of state is reached.

This section prepares the ground for new exact analytic solutions of hydrodynamics where the initial temperature profile is spatially inhomogeneous. Although such solutions can be obtained by straight-forward generalizations of the exact solutions of ref. [8] with spatially inhomogeneous temperature profiles both in the high temperature QM and in the low temperature HM phases, even for a multi-component hadronic matter scenario, their matching at the chemical freeze-out temperature is an open research question hence these solutions are not detailed here.

5 Conclusions

We described two new classes of exact solutions of fireball hydrodynamics, for a rehadronizing and expanding fireball, using lattice QCD Equation of State. In the first class of solutions, the expaning ellipsoid is triaxial, but the fireball is not rotating, $(X \neq Y \neq Z, \omega = 0)$. In the second class of solutions, although the expansion is spheroidal, the fireball is rotating, $(X = Y = R \neq Z, \omega \neq 0)$. In both cases, we found that the fireball expands to the vacuum as a whole,

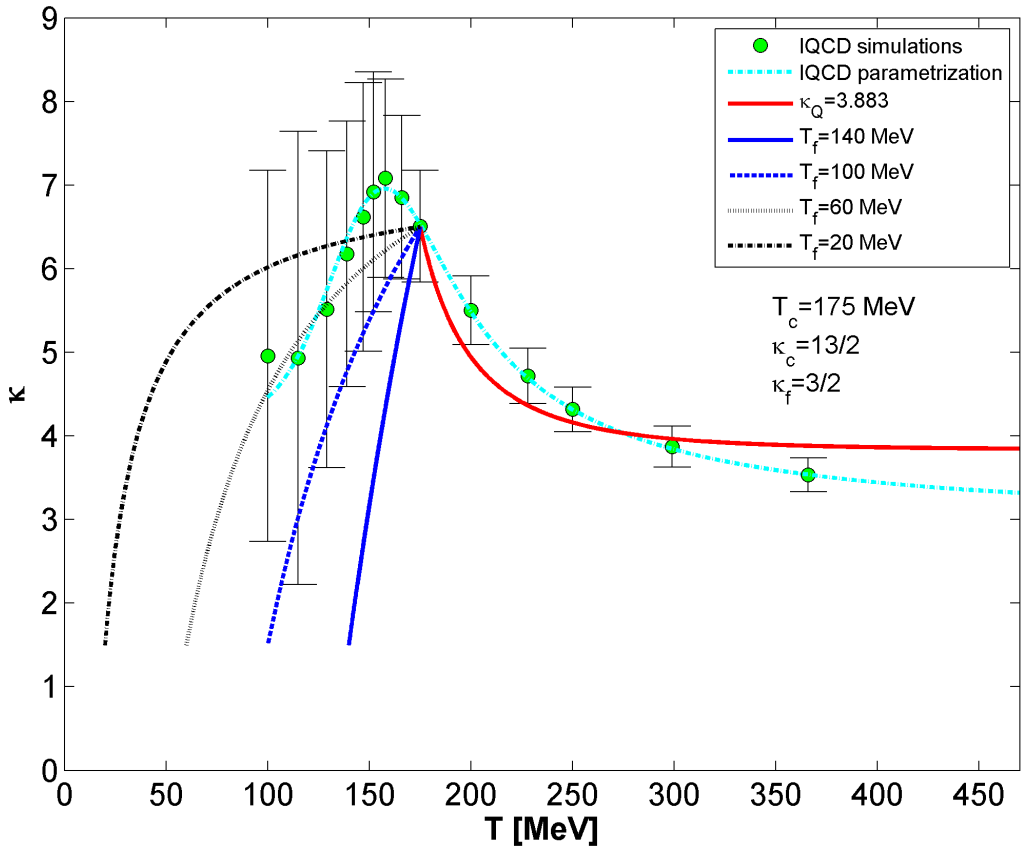

Figure 1: Fits of the hydrodynamically motivated parameterizations above and below T_{chem} to the lattice QCD data points on $\kappa(T) = \varepsilon/p$. In these fits, we required that at freeze-out, a non-relativistic ideal gas limit is approached so that $\kappa(T_f) = 3/2$ and varied the freeze-out temperature from 20 to 140 MeV.

although the quark matter rehadronizes to a hadronic matter that includes various hadronic components (for example pions, kaons, protons and all the other measured hadronic species). In both classes of the presented new solutions, the same length and temperature scales characterize the fireball dynamics for all the hadronic types in the final state, $(X \neq X_i, Y \neq Y_i, Z \neq Z_i)$, so the fireball keeps on expanding as a whole, instead of developing non-equilibrium features such as separate lenght-scales for each observable hadrons.

We have obtained a surprising analytic insight to the effects of hadrochemical freeze-out on the expansion dynamics. If rehadronization is immediately followed by a hadrochemical freeze-out, this leads to a modification of the dynamical equations, which in turn leads to a second, violent, hadrochemical explosion. Instead of slowing down the radial flows at the softest point where p/ε is minimal, the expansion dynamics does not slow down, but it actually accelerates. We have found that the expansion dynamics starts to accelerate at the chemical freeze-out temperature due to the inequality (13) which is a

consequences of the application of lattice QCD EoS when evaluating the expansion dynamics in Tables 2 and 3. In this hadrochemical explosion, all the length-scales (X, Y, Z) and R start to accelerate faster, when the temperature drops just below $T = T_{chem}$, as compared to a scenario without hadrochemical freeze-out, so in this sense the dynamics becomes "hardest" at the "softest point" of the lattice QCD Equation of State.

In the last section, we have also shown that the lattice QCD equation of state $\kappa(T)$ can be parametrized in a new way, which is suitable for the development of exact and analytic, parametric solutions of fireball hydrodynamics even for an initially inhomogenous temperature profile. The details of this solution with inhomogeneous temperature profile, as well as the extension of the presented solutions to the relativistic kinematic region are important issues that go beyond the scope of the limitations of this conference contribution.

Acknowledgments

We thank Y. Hatta, D. Klabucar, T. Kunihiro, S. Nagamiya and K. Ozawa for enlightening and useful discussions. T. Cs. would like to thank S. Nagamiya and K. Ozawa for their kind hospitality at KEK, Tsukuba, Japan. This research was supported by the Hungarian OTKA grant NK 101438 as well as by a 2016 KEK Visitor Fund.

References

[1] J. P. Bondorf, S. I. A. Garpman, and J. Zimányi. *Nucl. Phys.*, A296:320–332, 1978.

[2] P. Csizmadia, T. Csörgő, and B. Lukács. *Phys. Lett.*, B443:21–25, 1998.

[3] T. Csörgő. *Central Eur. J. Phys.*, 2:556–565, 2004.

[4] S.V. Akkelin, T. Csörgő, B. Lukács, Yu.M. Sinyukov, and M. Weiner. *Phys. Lett.*, B505:64–70, 2001.

[5] T. Csörgő. *Acta Phys. Polon.*, B37:483–494, 2006.

[6] T. Csörgő, S.V. Akkelin, Y. Hama, B. Lukács, and Yu.M. Sinyukov. *Phys. Rev.*, C67:034904, 2003.

[7] M. I. Nagy, T. Csörgő, and M. Csanád. *Phys. Rev.*, C77:024908, 2008.

[8] T. Csörgő and M.I. Nagy. *Phys.Rev.*, C89(4):044901, 2014.

[9] T. Csörgő, M. I. Nagy, and I. F. Barna. *Phys. Rev.*, C93(2):024916, 2016.

[10] M. I. Nagy and T. Csörgő. `arXiv:1606.0916`, submitted for a publication (2016).

[11] M. Csanád, M. I. Nagy, and S. Lökös. *Eur. Phys. J.*, A48:173, 2012.

[12] I. G. Bearden et al, NA44 Collaboration. *Phys. Rev. Lett.*, 78:2080–2083, 1997.

[13] S. S. Adler et al, PHENIX Collaboration. *Phys. Rev.*, C69:034909, 2004.

[14] Sz. Borsányi, G. Endrődi, Z. Fodor, A. Jakovác, S. D. Katz, et al. *JHEP*, 1011:077, 2010.

[15] S. Z. Belenkij and L. D. Landau. *Nuovo Cim. Suppl.* **3S10**, 15 (1956) [*Usp. Fiz. Nauk* **56**, 309 (1955)].

[16] M. Kaneta and N. Xu, `nucl-th/0405068` .

[17] T. S. Biró, Phys. Lett. B **474**, 21 (2000) [nucl-th/9911004].

[18] T. S. Biró, Phys. Lett. B **487**, 133 (2000) [nucl-th/0003027].

[19] D. Kincses, for the PHENIX Collaboration: *Acta Phys. Polon. Supp.*, 9:243, 2016.

Probing BFKL dynamics in Mueller-Navelet jet production at the LHC

B. Ducloué[1,2], L. Szymanowski[3], S. Wallon[4,5]

[1]Department of Physics, University of Jyväskylä,
P.O. Box 35, 40014 University of Jyväskylä, Finland
[2]Helsinki Institute of Physics, P.O. Box 64,
00014 University of Helsinki, Finland
[3]National Centre for Nuclear Research,
Hoża 69, 00-681 Warsaw, Poland
[4]Laboratoire de Physique Théorique, UMR 8627, CNRS,
Univ. Paris Sud, Université Paris-Saclay, 91405 Orsay, France
[5]UPMC Univ. Paris 06, Faculté de Physique,
4 place Jussieu, 75252 Paris Cedex 05, France

August 9, 2017

Abstract

We review the results of our studies on the production of two jets with a large interval of rapidity at hadron colliders, which was proposed by Mueller and Navelet as a possible test of the high energy dynamics of QCD, within the next-to-leading logarithm framework. The application of the Brodsky-Lepage-Mackenzie procedure to fix the renormalization scale leads to a very good description of the available CMS data at the LHC for the azimuthal correlations of the jets. We show that the inclusion of next-to-leading order corrections to the jet vertex significantly reduces the importance of energy-momentum non-conservation which is inherent to the BFKL approach, for an asymmetric jet configuration.

One of the most famous testing grounds for BFKL physics [1] are the Mueller Navelet jets [2], illustrated in Fig. 1. Besides the cross section also a more exclusive observable within this process drew the attention, namely the azimuthal correlation between these jets. Considering hadron-hadron scattering in the common parton model to describe two jet production at LO, one deals with a back-to-back reaction and expects the azimuthal angles of the two jets always to be π and hence completely correlated. This corresponds in Fig. 1 to $\phi_{J,1} = \phi_{J,2} - \pi$. But when we increase the rapidity difference between these jets, the phase space allows for more and more emissions leading to an angular decorrelation between the jets.

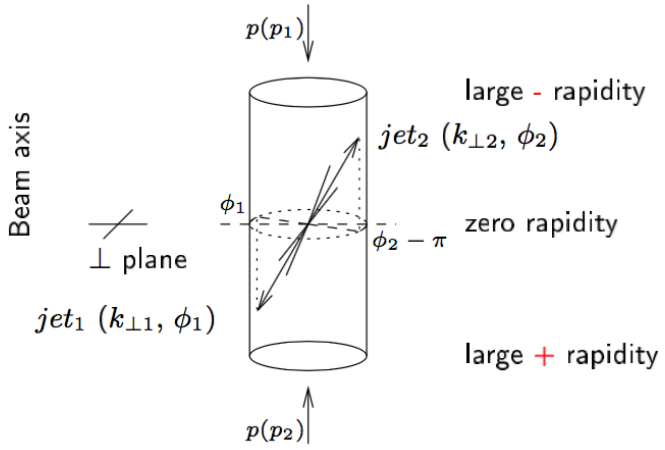

Figure 1: Mueller Navelet jets production.

The production of two jets of transverse momenta $\mathbf{k}_{J,1}$, $\mathbf{k}_{J,2}$ and rapidities $y_{J,1}$, $y_{J,2}$ is described by the differential cross-section

$$\frac{\mathrm{d}\sigma}{\mathrm{d}|\mathbf{k}_{J,1}|\,\mathrm{d}|\mathbf{k}_{J,2}|\,\mathrm{d}y_{J,1}\,\mathrm{d}y_{J,2}} = \sum_{\mathrm{a,b}} \int_0^1 \mathrm{d}x_1 \int_0^1 \mathrm{d}x_2\, f_{\mathrm{a}}(x_1) f_{\mathrm{b}}(x_2) \frac{\mathrm{d}\hat{\sigma}_{\mathrm{ab}}}{\mathrm{d}|\mathbf{k}_{J,1}|\,\mathrm{d}|\mathbf{k}_{J,2}|\,\mathrm{d}y_{J,1}\,\mathrm{d}y_{J,2}}, \tag{1}$$

where $f_{\mathrm{a,b}}$ are the usual collinear partonic distributions (PDF). In the BFKL framework, the partonic cross-section reads

$$\frac{\mathrm{d}\hat{\sigma}_{\mathrm{ab}}}{\mathrm{d}|\mathbf{k}_{J,1}|\,\mathrm{d}|\mathbf{k}_{J,2}|\,\mathrm{d}y_{J,1}\,\mathrm{d}y_{J,2}} = \int \mathrm{d}\phi_{J,1}\,\mathrm{d}\phi_{J,2} \int \mathrm{d}^2\mathbf{k}_1\,\mathrm{d}^2\mathbf{k}_2\, V_{\mathrm{a}}(-\mathbf{k}_1, x_1)\, G(\mathbf{k}_1, \mathbf{k}_2, \hat{s})\, V_{\mathrm{b}}(\mathbf{k}_2, x_2), \tag{2}$$

where $V_{\mathrm{a,b}}$ and G are respectively the jet vertices and the BFKL Green's function. At present, they are known with the next-to-leading logarithm accuracy [3, 4, 5, 6, 7]. The cross sections (1, 2) are the basic blocks of the calculations presented in [9, 10, 11] of the decorrelation coefficients $\langle \cos m(\pi - \Delta\phi) \rangle$, $\Delta\phi = \phi_{J,1} - \phi_{J,2}$, $m \in N$,

which are observables which can be measured at experiments performed at the LHC. At present the measurements of the CMS collaboration are done for the so called the symmetric configuration of produced jets, i.e. jets in which the lower limit on transverse momentum is the same for both jets.The theoretical estimates obtained in this case for $\langle \cos m(\pi - \Delta\phi)\rangle$ with the use of the Brodsky-Lepage-Mackenzie method to fix the renormalization scale [12], turns out to be in good agreement with the measurement reported recently by the CMS collaboration [8]. This fact is

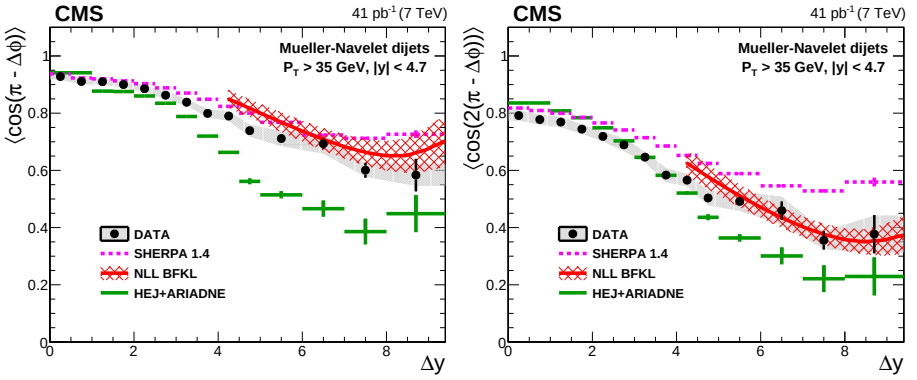

Figure 2: The comparison of the results of the theoretical calculation of Ref. [11] for $\langle \cos(\pi - \Delta\phi)\rangle$ (left panel) and $\langle \cos 2(\pi - \Delta\phi)\rangle$ (right panel), with the measurements by CMS@LHC presented in [8].

clearly illustrated in Fig. 2 and the left panel of Fig. 3 shown in Ref. [8], which also shows the comparison of measurements with various Monte Carlo simulations. The observables which are more robust against theoretical uncertainties, in particular which are more stable against a choice of renormalization and factorization scales, are the ratios of decorrelation coefficients. Fig. 4 shows a good agreeement of results of calculation with the CMS data. The CMS collaboration also measured

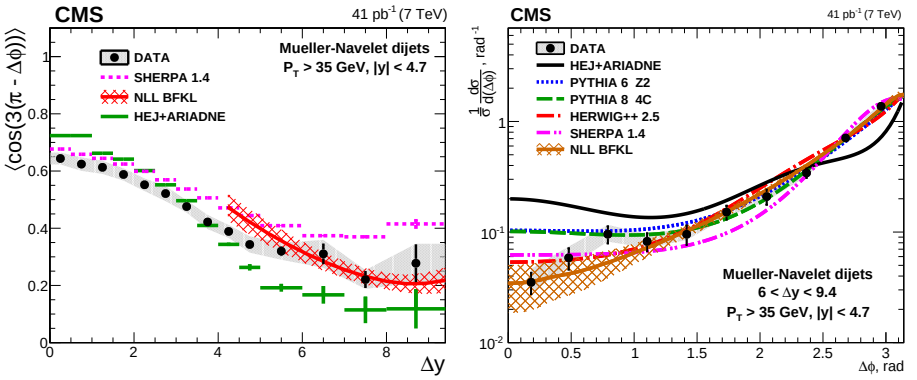

Figure 3: The comparison of theoretical calculation of Ref. [11] for $\langle \cos 3(\pi - \Delta\phi)\rangle$ (left panel) and $\frac{1}{\sigma}\frac{d\sigma}{d\varphi}$ (right panel), with the measurements by CMS@LHC presented in [8].

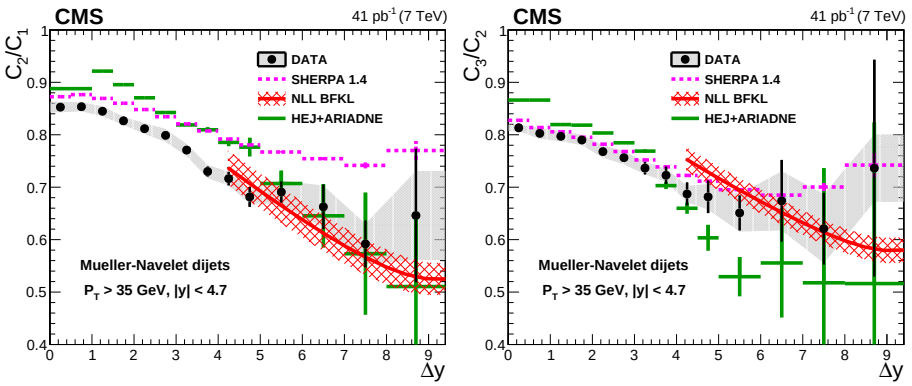

Figure 4: The comparison of theoretical predictions of Ref. [11] for the ratio $\frac{\cos 2\varphi}{\cos \varphi}$ (left panel) and the ratio $\frac{\cos 3\varphi}{\cos 2\varphi}$ (right panel), with the measurements by CMS@LHC presented in [8].

the azimuthal distribution of the jets, defined as

$$\frac{1}{\sigma}\frac{d\sigma}{d\varphi} = \frac{1}{2\pi}\left\{1 + 2\sum_{n=1}^{\infty}\cos(n\varphi)\,\langle\cos(n\varphi)\rangle\right\}, \quad \varphi = \Delta\phi - \pi\,. \tag{3}$$

The good agreement between theoretical estimates of [11] and measurements of this observable is shown in the right panel of Fig. 3.

Up to now we discussed production of jets in the symmetric configuration. From theoretical point of view the Monte Carlo simulations suffer in this case from instabilities which makes difficult the comparison of theoretical results based on BFKL method with the fixed order calculation. Such comparison of different theoretical predictions can be made in the case of jet production in the asymmetric configuration, in which two jets have very different transverse momenta. In the Fig. 5 and

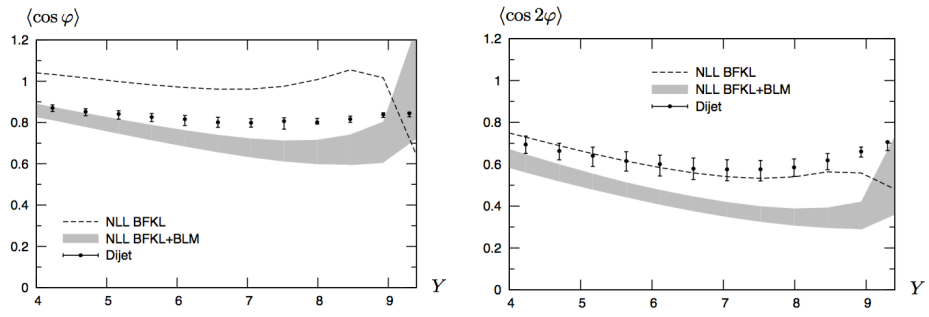

Figure 5: Asymmetric configuration. Variation of $\langle\cos\varphi\rangle$ and $\langle\cos 2\varphi\rangle$ as a function of rapidity difference Y at NLL accuracy compared with a fixed order treatment.

in the left panel of Fig. 6 we present our theoretical predictions for decorrelation coefficients and their ratio confronted with the result of the fixed order calculation

of Ref. [13]. It seems that specially in the case of the ratio $\frac{\cos 2\varphi}{\cos \varphi}$ a measurement of this observable could discriminate between two different mechanisms. Unfortunately, for now experimental measurements in such asymmetric configurations, although very desirable, are not available.

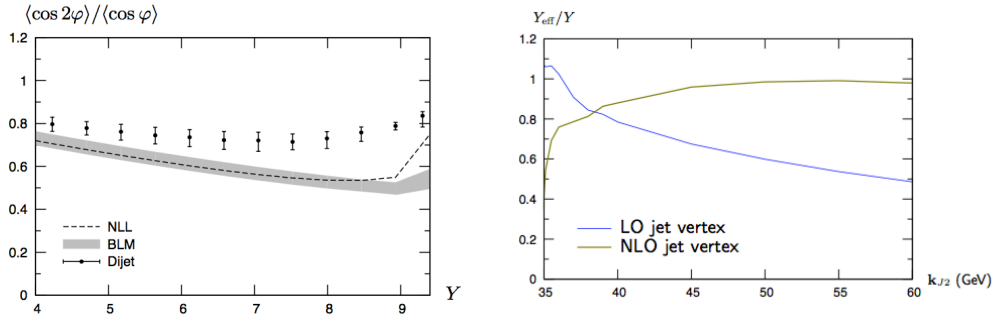

Figure 6: Left panel: Asymmetric configuration. Variation of the ratio $\frac{\langle \cos 2\varphi \rangle}{\langle \cos \varphi \rangle}$ as a function of rapidity difference Y at NLL accuracy compared with a fixed order treatment. Right panel: Variation of the ratio $\frac{Y_{eff}}{Y}$ as a function of jet momentum $\mathbf{k}_{J,2}$ for fixed $\mathbf{k}_{J,1} = 35\,\mathrm{GeV}$ for $Y = 8$ and $s = 7\,\mathrm{TeV}$ at leading logarithmic (blue) and next-to-leading logarithmic (brown) accuracy

The important drawback of the BFKL method is the fact that it does not respect exact energy-momentum conservation. This fact can lead to sizable numerically effects, although formally it represents a non-leading correction. In the Ref. [14] we studied the violation of energy-momentum conservation for asymmetric configuration using the method proposed by Del Duca nd Schmidt in [15]. In consist in introduction of the effective rapidity Y_{eff} defined as

$$Y_{\mathrm{eff}} \equiv \; Y \frac{\mathcal{C}_0^{2\to 3}}{\mathcal{C}_0^{\mathrm{BFKL},\mathcal{O}(\alpha_s^3)}} \tag{4}$$

in [14], where $\mathcal{C}_0^{2\to 3}$ is the amplitude for $2 \to 3$ partonic process (contributing to the cross section) calculated up to $\mathcal{O}(\alpha_s^3)$ accuracy without any approximations and $\mathcal{C}_0^{\mathrm{BFKL},\mathcal{O}(\alpha_s^3)}$ is the amplitude of the same process obtained within BFKL method. If the violation of energy-momentum conservation is not numerically important the ratio $\frac{Y_{\mathrm{eff}}}{Y}$ should take values close to one. In the right panel of Fig. 6 we show our result for the ratio $\frac{Y_{\mathrm{eff}}}{Y}$ estimated by taking into account NLO BFKL corrections to the jet production vertex . We see that for very asymmetric jet momenta this ratio takes values close to 1, which justifies our conclusion that the predictions obtained for production of jets in asymmetric configuration should not be affected by violation of energy-momentum conservation.

This work is partly supported by grant No 2015/17/B/ST2/01838 of the National Science Center in Poland, by the French grant ANR PARTONS (Grant No. ANR-12-MONU-0008-01), by the Academy of Finland, project 273464, by the COPIN-IN2P3 agreement, by the Labex P2IO and by the Polish-French collaboration agreement Polonium.

References

[1] V.S. Fadin, E. Kuraev, L. Lipatov, Phys. Lett. **B60**, 50 (1975); Sov. Phys. JETP **44**, 443 (1976); E. Kuraev, L. Lipatov, V.S. Fadin, Sov. Phys. JETP **45**, 199 (1977); I. Balitsky, L. Lipatov, Sov. J. Nucl. Phys. **28**, 822 (1978)

[2] A.H. Mueller, H. Navelet, Nucl. Phys. **B282**, 727 (1987)

[3] V.S. Fadin, L.N. Lipatov, Phys. Lett. **B429**, 127 (1998), hep-ph/9802290

[4] M. Ciafaloni, G. Camici, Phys. Lett. **B430**, 349 (1998), hep-ph/9803389

[5] J. Bartels, D. Colferai, G.P. Vacca, Eur. Phys. J. **C24**, 83 (2002), hep-ph/0112283

[6] J. Bartels, D. Colferai, G.P. Vacca, Eur. Phys. J. **C29**, 235 (2003), hep-ph/0206290

[7] F. Caporale, D. Y. Ivanov, B. Murdaca, A. Papa and A. Perri, JHEP **1202** (2012) 101, hep-ph/1112.3752

[8] V. Khachatryan *et al.* [CMS Collaboration], JHEP **1608** (2016) 139, hep-ex/1601.06713

[9] D. Colferai, F. Schwennsen, L. Szymanowski, S. Wallon, JHEP **1012**, 026 (2010), 1002.1365

[10] B. Ducloué, L. Szymanowski, S. Wallon, JHEP **1305**, 096 (2013), 1302.7012

[11] B. Ducloué, L. Szymanowski, S. Wallon, Phys. Rev. Lett. **112**, 082003 (2014), 1309.3229

[12] S.J. Brodsky, G.P. Lepage, P.B. Mackenzie, Phys. Rev. **D28**, 228 (1983)

[13] P. Aurenche, R. Basu, M. Fontannaz, Eur. Phys. J. **C57**, 681 (2008), 0807.2133

[14] B. Ducloué, L. Szymanowski, S. Wallon, Phys. Lett. **B738**, 311 (2014), 1407.6593

[15] V. Del Duca, C.R. Schmidt, Phys. Rev. **D51**, 2150 (1995), hep-ph/9407359

Exclusive production of two and four pions in proton-proton scattering

P. Lebiedowicz[1], O. Nachtmann[2], A. Szczurek[1] *

[1]Institute of Nuclear Physics Polish Academy of Sciences, Radzikowskiego 152, PL-31342 Kraków, Poland
[2]Institut für Theoretische Physik, Universität Heidelberg, Philosophenweg 16, D-69120 Heidelberg, Germany

August 9, 2017

Abstract

We consider exclusive $pp \to pp\pi^+\pi^-$ and $pp \to pp\pi^+\pi^-\pi^+\pi^-$ reactions at high energies. The calculation is based on a tensor pomeron model and the amplitudes for the processes are formulated in an effective field-theoretic approach. In the case of $pp \to pp\pi^+\pi^-$ process we consider both diffractive and photoproduction mechanisms and we include the non-resonant $\pi^+\pi^-$ continuum and the resonance $f_0(500)$, $f_0(980)$, $f_2(1270)$, $\rho(770)$ contributions. We discuss how two pomerons couple to tensor meson $f_2(1270)$ and the interference effects of resonance and dipion continuum. We find that the relative contribution of resonances $\rho(770)$, $f_2(1270)$ and dipion continuum strongly depends on the cut on proton transverse momenta. In the case of exclusive central 4π production we include the contribution via the intermediate $\sigma\sigma$ and $\rho\rho$ states. For both processes the theoretical results have been compared with the experimental data and predictions for planned or being carried out experiments (e.g. STAR, ATLAS-ALFA) are presented.

*Also at University of Rzeszów, PL-35959 Rzeszów, Poland.

1 Introduction

Central production mediated by the "fusion" of two exchanged pomerons [1, 2] is an important diffractive process for the investigation of properties of dipion resonances, in particular, for search of gluonic bound states (glueballs). The experimental groups at the CERN-ISR [4], COMPASS [3], STAR [5], CDF [6], ALICE [7], and CMS [8] all show visible structures in the $\pi^+\pi^-$ invariant mass. The LHCb experiment is also well suited to measuring central exclusive production processes [9].

Some time ago two of us have formulated a Regge-type model of the dipion continuum for the exclusive reaction $pp \to pp\pi^+\pi^-$ with parameters fixed from phenomenological analysis of total and elastic NN and πN scattering [12]. The model was extended to include rescattering corrections due to pp nonperturbative interaction [13, 10]. The exclusive reaction $pp \to pp\pi^+\pi^-$ constitutes an irreducible background to the scalar $f_0(1500)$ [11] and χ_{c0} [13] mesons production. These model studies were extended to the exclusive $pp \to ppK^+K^-$ reaction [14]. The largest uncertainties in the model are due to the unknown off-shell pion form factor and the absorption effects; see Ref. [15]. Such an approach gives correct order of magnitude cross sections, however, does not include resonance contributions which interfere with the continuum contribution.

First calculations of central exclusive diffractive production of $\pi^+\pi^-$ continuum together with the dominant scalar $f_0(500)$, $f_0(980)$, and tensor $f_2(1270)$ resonances was performed in Ref. [1]. Here we use the tensor-pomeron model formulated in [16]; see also [17]. In this model pomeron exchange is effectively treated as the exchange of a rank-2 symmetric tensor. In [18] we show that the tensor pomeron is consistent with the STAR experimental data on polarised high-energy pp elastic scattering [19]. In Ref. [20] the model was applied to the diffractive production of several scalar and pseudoscalar mesons in the reaction $pp \to ppM$. The corresponding pomeron-pomeron-meson coupling constants are not known and have been fitted to existing WA102 experimental data. In most cases one has to add coherently amplitudes for two pomeron-pomeron-meson couplings with different orbital angular momentum and spin of two "pomeron particles". [1] In [21] an extensive study of the photoproduction reaction $\gamma p \to \pi^+\pi^- p$ was presented. The resonant ($\rho^0 \to \pi^+\pi^-$) and non-resonant (Drell-Söding) photon-pomeron/reggeon $\pi^+\pi^-$ production in pp collisions was studied in [22].

The identification of glueballs can be very difficult. The studies of different decay channels in central exclusive production would be very valuable in this context. One of the possibilities is the $pp \to pp\pi^+\pi^-\pi^+\pi^-$ reaction being analysed at the RHIC and LHC. In Ref. [23] we analysed the exclusive diffractive production of four-pion via the intermediate $\sigma\sigma$ and $\rho\rho$ states within the tensor-pomeron model.

2 Sketch of the formalism

The Born-level diagrams for the continuum and resonant $\pi^+\pi^-$ production are shown in Fig. 1. The purely diffractive amplitude is a sum of continuum amplitude

[1] We wish to emphasize that the tensorial pomeron can equally well describe the WA102 experimental data on the exclusive meson production as the less theoretically justified vectorial pomeron frequently used in the literature. The existing low-energy experimental data do not allow to clearly distinguish between the two approaches as the presence of subleading reggeon exchanges is at low energies very probable for many $pp \to ppM$ reactions.

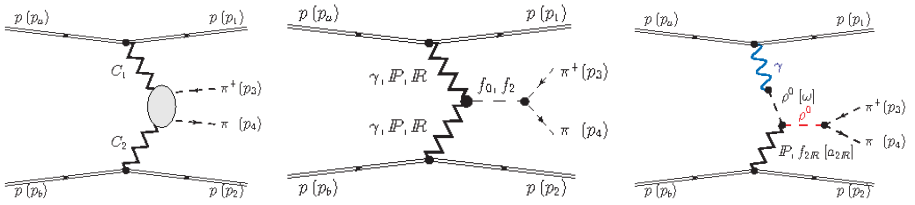

Figure 1: Generic Born-level diagrams for central exclusive production of continuum $\pi^+\pi^-$ and resonances in proton-(anti)proton collisions. Here we labelled the exchanged objects by their charge conjugation numbers C_1, $C_2 \in \{+1, -1\}$.

and the amplitudes with the s-channel scalar and tensor resonances:

$$\mathcal{M}_{pp\to pp\pi^+\pi^-} = \mathcal{M}^{\pi\pi-\text{continuum}}_{pp\to pp\pi^+\pi^-} + \mathcal{M}^{(I\!P I\!P\to f_0\to\pi^+\pi^-)}_{\lambda_a\lambda_b\to\lambda_1\lambda_2\pi^+\pi^-} + \mathcal{M}^{(I\!P I\!P\to f_2\to\pi^+\pi^-)}_{\lambda_a\lambda_b\to\lambda_1\lambda_2\pi^+\pi^-} . \quad (1)$$

The Born amplitude, for instance, for the process $pp \to pp(f_2 \to \pi^+\pi^-)$ can be written in the effective tensor pomeron approach as

$$\begin{aligned}\mathcal{M}^{(I\!P I\!P\to f_2\to\pi^+\pi^-)}_{\lambda_a\lambda_b\to\lambda_1\lambda_2\pi^+\pi^-} = (-i)\,\bar{u}(p_1,\lambda_1) i\Gamma^{(I\!P pp)}_{\mu_1\nu_1}(p_1,p_a) u(p_a,\lambda_a)\, i\Delta^{(I\!P)\,\mu_1\nu_1,\alpha_1\beta_1}(s_1,t_1) \\ \times i\Gamma^{(I\!P I\!P f_2)}_{\alpha_1\beta_1,\alpha_2\beta_2,\rho\sigma}(q_1,q_2)\; i\Delta^{(f_2)\,\rho\sigma,\alpha\beta}(p_{34})\, i\Gamma^{(f_2\pi\pi)}_{\alpha\beta}(p_3,p_4) \\ \times i\Delta^{(I\!P)\,\alpha_2\beta_2,\mu_2\nu_2}(s_2,t_2)\; \bar{u}(p_2,\lambda_2) i\Gamma^{(I\!P pp)}_{\mu_2\nu_2}(p_2,p_b) u(p_b,\lambda_b)\,, \quad (2)\end{aligned}$$

where $t_1 = q_1^2 = (p_1 - p_a)^2$, $t_2 = q_2^2 = (p_2 - p_b)^2$, $s_1 = (p_a + q_2)^2 = (p_1 + p_{34})^2$, $s_2 = (p_b + q_1)^2 = (p_2 + p_{34})^2$, $p_{34} = p_3 + p_4$. $\Delta^{(I\!P)}$ and $\Gamma^{(I\!P pp)}$ denote the effective pomeron propagator and proton vertex function, respectively. For the explicit expressions, see Sec. 3 of [16]. In Ref. [1] (see Appendix A) we have considered all possible tensorial structures for the $I\!P I\!P f_2$ coupling. For a more details, as form of form factors, the tensor-meson propagator $\Delta^{(f_2)}$ and the $f_2\pi\pi$ vertex, see Refs. [16, 1].

We consider also the production of $\rho(770)$ resonance and the non-resonant (Drell-Söding) $\pi^+\pi^-$ continuum produced by photon-pomeron and photon-$f_{2I\!R}$ mechanisms studied in detail in [22]. The $I\!P\rho\rho$ vertex is given in [16] by formula (3.47). The coupling parameters of Regge exchanges was fixed based on the HERA experimental data for the $\gamma p \to \rho^0 p$ reaction. In [22] we showed that the ρ^0 term interfere with the non-resonant terms producing a skewing of the ρ^0-meson line shape. Due to the photon propagators occurring in diagrams we expect these processes to be most important when at least one of the protons undergoes only a very small $|t_{1,2}|$.

3 Selected results

We start from a discussion of some dependences for the central exclusive production of the $f_2(1270)$ meson. For a detailed study of $f_2(1270)$ production see Ref. [1]. In Fig. 2 we present results for individual pomeron-pomeron-f_2 coupling terms (there are 7 possible terms [1]) at $\sqrt{s} = 200$ GeV and $|\eta_\pi| < 1$. The different predictions differ considerably which could be checked experimentally. We show that only in two cases ($j = 2$ and 5) the cross section $d\sigma/d|t_{1,2}|$ vanishes when $|t_{1,2}| \to 0$.

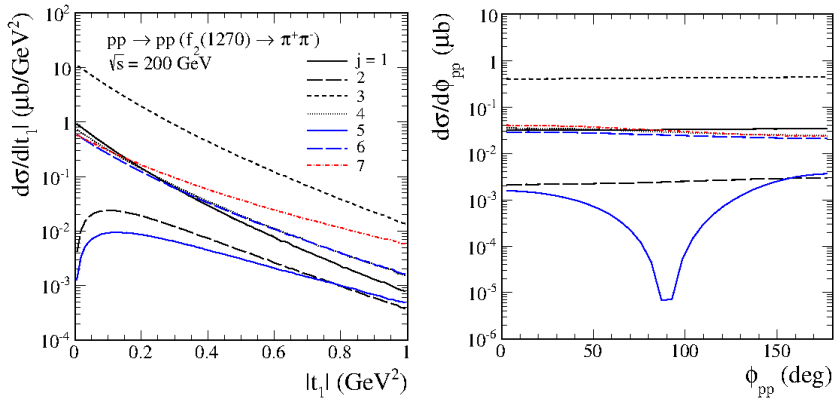

Figure 2: The (Born-level) distribution in transferred four-momentum squared between the initial and final protons (left panel) and the distribution in azimuthal angle between the outgoing protons (right panel) at $\sqrt{s} = 200$ GeV and $|\eta_\pi| < 1$. We show the individual contributions of the different pomeron-pomeron-$f_2(1270)$ couplings. For illustration the results have been obtained with coupling constants fixed at $g^{(j)}_{I\!P I\!P f_2} = 1.0$.

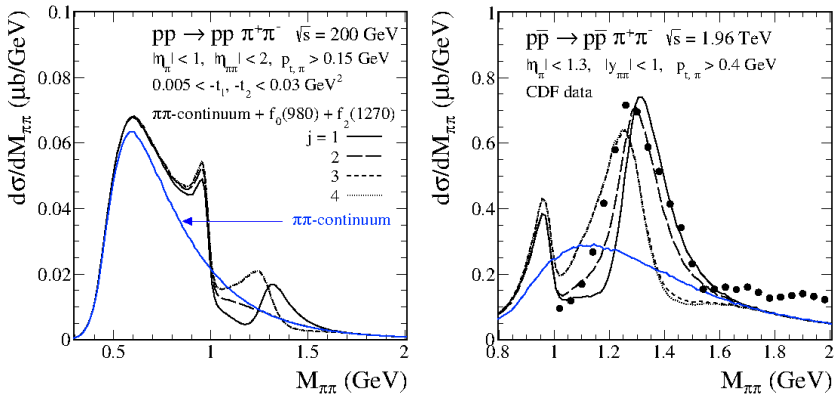

Figure 3: Two-pion invariant mass distribution for the STAR [5] (left) and CDF [6] (right) kinematics. The individual contributions of different $I\!P I\!P f_2$ couplings ($j = 1, ..., 4$) are compared with the CDF data [6]. The Born calculations for $\sqrt{s} = 200$ GeV and $\sqrt{s} = 1.96$ TeV were multiplied by the gap survival factors $\langle S^2 \rangle = 0.2$ and $\langle S^2 \rangle = 0.1$, respectively. The blue solid lines represent the non-resonant continuum contribution only ($\Lambda_{off,M} = 0.7$ GeV) while the black lines represent a coherent sum of non-resonant continuum, $f_0(980)$ and $f_2(1270)$ resonant terms.

In [1] we tried to understand whether one can approximately describe the dipion invariant mass distribution observed by different experiments assuming only one of the seven possible $I\!P I\!P f_2$ tensorial couplings. We found that the feature of the $\pi^+\pi^-$ distribution depends on the cuts used in a particular experiment (usually the t cuts are different for different experiments). As can be clearly seen from Fig. 3 different $I\!P I\!P f_2$ couplings generate different interference patterns around $M_{\pi\pi} \sim 1.27$ GeV. A sharp drop around $M_{\pi\pi} \sim 1$ GeV is attributed to the interference of $f_0(980)$ and continuum. We can observe that the $j = 2$ coupling gives results close to those observed by the CDF Collaboration [6]. In this preliminary study we did not try to fit the existing data [6] by mixing different couplings because the CDF data are not fully exclusive (the outgoing p and $\bar{p}$ were not measured). The calculations were done at Born level and the absorption corrections were taken into account by multiplying the cross section by a common factor $\langle S^2 \rangle$ obtained from [15]. The two-pion continuum was fixed by choosing a form factor for the off-shell pion $\hat{F}_\pi(k^2) = \frac{\Lambda^2_{off,M} - m^2_\pi}{\Lambda^2_{off,M} - k^2}$ and $\Lambda_{off,M} = 0.7$ GeV.

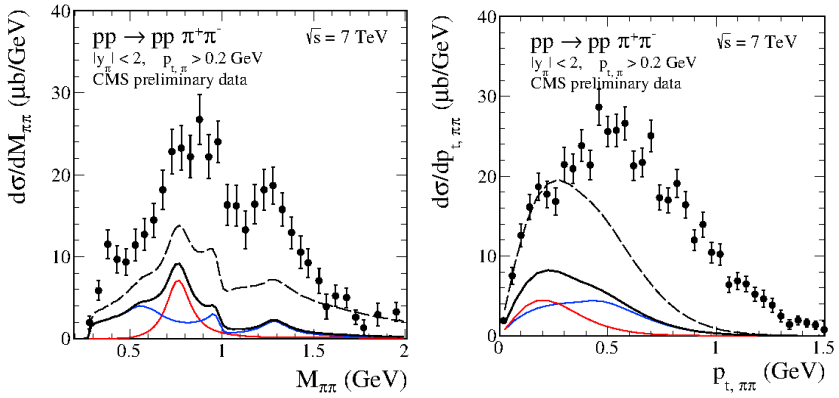

Figure 4: The distributions for two-pion invariant mass (left panel) and transverse momentum of the pion pair (right panel) for the CMS kinematics at $\sqrt{s} = 7$ TeV. Both photoproduction (red line) and purely diffractive (blue line) contributions multiplied by the factors $\langle S^2 \rangle = 0.9$ and $\langle S^2 \rangle = 0.1$, respectively, are included. The complete results correspond to the black solid line ($\Lambda_{off,M} = 0.7$ GeV) and the dashed line ($\Lambda_{off,M} = 1.2$ GeV). The CMS preliminary data scanned from [8] are shown for comparison.

In Fig. 4 we show results including in addition to the non-resonant $\pi^+\pi^-$ continuum, the $f_2(1270)$ and the $f_0(980)$ resonances, the contribution from photoproduction ($\rho^0 \to \pi^+\pi^-$, Drell-Söding mechanism), as well as the $f_0(500)$ resonant contribution. Our predictions are compared with the CMS preliminary data [8]. Here the absorption effects lead to huge damping of the cross section for the purely diffractive term (the blue lines) and relatively small reduction of the cross section for the photoproduction term (the red lines). Therefore we expect one could observe the photoproduction contribution. The CMS measurement [8] is not fully exclusive and the $M_{\pi\pi}$ and $p_{t,\pi\pi}$ spectra contain contributions associated with other processes, e.g., when one or both protons undergo dissociation. In addition, the dashed line corresponds to results with $\Lambda_{off,M} = 1.2$ GeV and better describe the preliminary CMS data. If we used the set of parameters adjusted to the CDF data [8] for the

STAR or CDF measurements our theoretical results there would be above the preliminary STAR data [5] at $M_{\pi\pi} > 1$ GeV and in complete disagreement with the CDF data from [6]. Only purely central exclusive data expected from CMS-TOTEM and ATLAS-ALFA will allow to draw definite conclusions.

In Fig. 5 we show the four-pion invariant mass distributions for the the reaction $pp \to pp\pi^+\pi^-\pi^+\pi^-$ proceeding via the intermediate $\sigma\sigma$ and the $\rho\rho$ states. The results for processes with the exchange of heavy mesons (compared to pion) strongly depend on the details of the hadronic form factors. By comparing the theoretical results and the cross sections found in the CERN-ISR experiment [24] we fixed the parameters of the off-shell meson form factor and the $I\!P\sigma\sigma$ and $f_{2I\!R}\sigma\sigma$ couplings. In the case of $\sigma\sigma$ contribution we use two sets of the coupling constants; standard (set A) and enhanced (set B) ones, see (2.11) and (2.12) of [23], respectively. [2] In the case of $\rho\rho$ contribution the ρ meson reggeization suppresses large masses of $M_{4\pi}$ distributions. This is also the case when the separation in rapidity between the two ρ mesons increases, see Fig. 4 of [23]. [3]

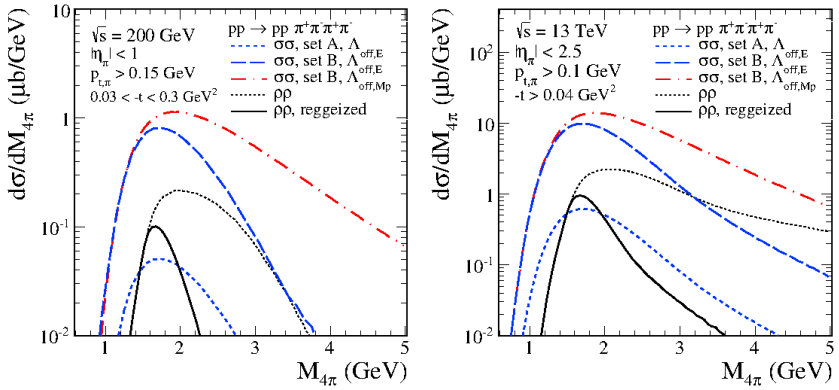

Figure 5: The 4π invariant mass distributions (for different experimental cuts) multiplied by the factors $\langle S^2 \rangle = 0.30$ (for $\sqrt{s} = 200$ GeV) and 0.23 (for $\sqrt{s} = 13$ TeV) estimated within the eikonal approximation (only the pp rescattering). The blue and red lines for the $\sigma\sigma$ contribution for the exponential off-shell meson form factors ($\Lambda_{off,E} = 1.6$ GeV) and the monopole ones ($\Lambda_{off,M} = 1.6$ GeV), respectively. The black lines represent results for the $\rho\rho$ contribution without (the dotted line) and with (the solid line) the ρ meson reggeization.

4 Conclusions

In our recent paper [1] we have analysed the exclusive central production of dipion continuum and resonances contributing to the $\pi^+\pi^-$ pair production in proton-(anti)proton collisions in an effective field-theoretic approach with tensor pomerons

[2] There is quite a good agreement between our $\sigma\sigma$ result with a monopole form factor and the 4π ($J = 0$, phase space) data from [24]. Note that this implies that the set B of couplings, which are larger than the corresponding pion couplings, seems to be preferred.

[3] We have found that the diffractive mechanism in pp collisions considered by us leads to the cross section for the $\rho\rho$ final state more than three orders of magnitude larger than the corresponding cross section for $\gamma\gamma \to \rho\rho$ and double scattering photon-pomeron (pomeron-photon) mechanisms considered in [25].

and reggeons as proposed in [16]. We have included the scalar ($f_0(500)$, $f_0(980)$) and tensor $f_2(1270)$ resonances as well as the vector $\rho(770)$ resonance in a consistent way. In the case of $f_2(1270)$-meson production via "fusion" of two tensor pomerons we have found (see Appendix A of [1]) the seven possible $I\!P I\!P f_2$ tensorial couplings. The different couplings give different results due to different interference effects of the f_2 resonance and the dipion continuum contributions. We have shown that the resonance structures in the measured two-pion invariant mass spectra depend on the cut on proton transverse momenta and/or on four-momentum transfer squared $t_{1,2}$ used in experiment. The model parameters of the optimal $I\!P I\!P f_2$ coupling ($j = 2$) have been roughly adjusted to the recent CDF and preliminary STAR experimental data and then used for the predictions for the ALICE, and CMS experiments. We have made estimates of cross sections for both the diffractive and photoproduction contributions. We have shown some differential distributions related to produced pions as well as some observables related to final state protons, e.g., different dependence on proton transverse momenta and azimuthal angle correlations between outgoing protons could be used to separate the photoproduction term, see [1]. The absorption effects due to pp and πp interactions, discussed in [15], lead to a significant modification of the shape of the distributions in ϕ_{pp}, $p_{t,p}$, $t_{1,2}$ and it would therefore be useful to study such observables experimentally when measuring forward protons (STAR, ATLAS-ALFA, CMS-TOTEM).
To summarize: We have given a consistent treatment of the exclusive $\pi^+\pi^-$ and $\pi^+\pi^-\pi^+\pi^-$ production in pp collisions in an effective field-theoretic approach. A measurable cross section of order of a few μb was obtained for both processes which should provide experimentalists interesting challenges to check and explore it.

Acknowledgement. This work was partially supported by the MNiSW Grant No. IP2014 025173 (Iuventus Plus) and the Polish National Science Centre grants DEC-2014/15/B/ST2/02528 and DEC-2015/17/D/ST2/03530.

References

[1] P. Lebiedowicz, O. Nachtmann, A. Szczurek, Phys. Rev. D **93**, 054015 (2016).

[2] R. Fiore, L. Jenkovszky, R. Schicker, Eur. Phys. J. C **76**, 38 (2016).

[3] A. Austregesilo (COMPASS Collaboration), AIP Conf. Proc. **1735**, 030012 (2016).

[4] T. Åkesson *et al.*, (AFS Collaboration), Nucl. Phys. B **264**, 154 (1986); A. Breakstone *et al.* (ABCDHW Collaboration), Z. Phys. C **31**, 185 (1986); A. Breakstone *et al.* (ABCDHW Collaboration), Z. Phys. C **42**, 387 (1989); Erratum: Z. Phys. C **43**, 522 (1989); A. Breakstone *et al.* (ABCDHW Collaboration), Z. Phys. C **48**, 569 (1990).

[5] L. Adamczyk, W. Guryn, J. Turnau, Int. J. Mod. Phys. A **29**, 1446010 (2014).

[6] T. Aaltonen *et al.* (CDF Collaboration), Phys. Rev. D **91**, 091101 (2015).

[7] R. Schicker (ALICE Collaboration), arXiv:1205.2588 [hep-ex].

[8] CMS Collaboration, Report No. CMS-PAS-FSQ-12-004.

[9] R. McNulty, PoS(DIS2016)181, arXiv:1608.08103 [hep-ex].

[10] R. Staszewski, P. Lebiedowicz, M. Trzebiński, J. Chwastowski, A. Szczurek, Acta Phys. Polon. B **42**, 1861 (2011).

[11] A. Szczurek and P. Lebiedowwicz, Nucl. Phys. A **826**, 101 (2009).

[12] P. Lebiedowicz and A. Szczurek, Phys. Rev. D **81**, 036003 (2010).

[13] P. Lebiedowicz, R. Pasechnik, A. Szczurek, Phys. Lett. B **701**, 434 (2011) .

[14] P. Lebiedowicz and A. Szczurek, Phys. Rev. D **85**, 014026 (2012).

[15] P. Lebiedowicz and A. Szczurek, Phys. Rev. D **92**, 054001 (2015).

[16] C. Ewerz, M. Maniatis, O. Nachtmann, Annals Phys. **342**, 31 (2014).

[17] O. Nachtmann, Annals Phys. **209**, 436 (1991).

[18] C. Ewerz, P. Lebiedowicz, O. Nachtmann, A. Szczurek, arXiv:1606.08067 [hep-ph].

[19] L. Adamczyk *et al.* (STAR Collaboration), Phys. Lett. B **719**, 62 (2013).

[20] P. Lebiedowicz, O. Nachtmann, A. Szczurek, Annals Phys. **344**, 301 (2014).

[21] A. Bolz, C. Ewerz, M. Maniatis, O. Nachtmann, M. Sauter, A. Schöning, JHEP **1501**, 151 (2015).

[22] P. Lebiedowicz, O. Nachtmann, A. Szczurek, Phys. Rev. D **91**, 074023 (2015).

[23] P. Lebiedowicz, O. Nachtmann, A. Szczurek, Phys. Rev. D **94**, 034017 (2016).

[24] A. Breakstone *et al.* (ABCDHW Collaboration), Z. Phys. C **58**, 251 (1993).

[25] V.P. Goncalves, B.D. Moreira, F.S. Navarra, Eur. Phys. J C **76**, 388 (2016).

High energy effects in multi-jet production at LHC

F. Caporale[1,2], F.G. Celiberto[1,2,3,4]*, G. Chachamis[1,2],
D. Gordo Gómez[1,2], B. Murdaca[4], A. Sabio Vera[1,2]

[1]Instituto de Física Teórica UAM/CSIC,
Nicolás Cabrera 15, Madrid, Spain
[2]Universidad Autónoma de Madrid, 28049 Madrid, Spain
[3]Dipartimento di Fisica, Università della Calabria,
Arcavacata di Rende, 87036 Cosenza, Italy
[4]Istituto Nazionale di Fisica Nucleare, Gruppo Collegato di Cosenza,
Arcavacata di Rende, 87036 Cosenza, Italy

August 9, 2017

Abstract

We study differential cross sections for the production of three and four jets in multi-Regge kinematics, the main interest lying on azimuthal angle dependences. The theoretical setup is the jet production from a single BFKL ladder with a convolution of two/three BFKL Green functions, where two forward/backward jets are always tagged in the final state. Furthermore, we require the tagging of one/two further jets in more central regions of the detectors with a relative separation in rapidity. We found, as result, that the dependence on transverse momenta and rapidities of the central jets can be considered as a distinct signal of the onset of BFKL dynamics.

*Speaker.

1 Introduction

The study of semi-hard processes in the high-energy (Regge) limit represents an ultimate research field for perturbative QCD, the Large Hadron Collider (LHC) providing with an abundance of data. Multi-Regge kinematics (MRK), which prescribes final state objects strong ordered in rapidity, is the key point for the study of multi-jet production at LHC energies. In this kinematical regime, the Balitsky-Fadin-Kuraev-Lipatov (BFKL) approach, at leading (LL) [1, 2, 3, 4, 5, 6] and next-to-leading (NLL) [7, 8] accuracy, is the most powerful tool to perform the resummation of large logarithms in the colliding energy to all orders of the perturbative expansion. This formalism was successfully applied to lepton-hadron Deep Inelastic Scattering at HERA (see, *e.g.* [9, 10]) in order to study quite inclusive processes which are not that suitable though to discriminate between BFKL dynamics and other resummations. The high energies reachable at the LHC, however, allow us to investigate processes with much more exclusive final states which could, in principle, be only described by the BFKL framework, making it possible to disentangle the applicability region of the approach. So far, Mueller–Navelet jet production [11] has been the most studied process. Interesting observables associated to this reaction are the azimuthal correlation momenta which, however, are strongly affected by collinear contaminations. Therefore, new observables independent from the conformal contribution were proposed in [12, 13] and calculated at NLL in [14, 15, 16, 17, 18, 19, 20, 21], showing a very good agreement with experimental data at the LHC. Nevertheless, Mueller-Navelet configurations are still too inclusive to perform MRK precision studies. Pursuing the goal to further and deeply probe the BFKL dynamics by studying azimuthal decorrelations where the transverse momenta of extra particles introduces a new dependence, we proposed new observables for semi-hard processes which can be thought as a generalization of Mueller-Navelet jets[1]. These processes are inclusive three-jet [24, 25] and four-jet production [26, 27].

2 Multi-jet production

The class of processes under exam is the inclusive hadroproduction of n jets in the final state, well separated in rapidity so that $y_i > y_{i+1}$ according to MRK, and with their transverse momenta $\{k_i\}$ lying above the experimental resolution scale, together with an undetected gluon radiaton emission. With the aim to generalize the azimuthal ratios R_{nm} defined in the Mueller–Navelet jet configuration, we propose new, generalized azimuthal observables by taking the projection of the differential cross section $d\sigma^{n-\mathrm{jet}}$ on all angles, so having the general expression given in Eq. (3) of [28]:

$$\mathcal{C}_{M_1 \cdots M_{n-1}} = \left\langle \prod_{i=1}^{n-1} \cos\left(M_i\, \phi_{i,i+1}\right) \right\rangle = \int_0^{2\pi} d\theta_1 \cdots \int_0^{2\pi} d\theta_n \prod_{i=1}^{n-1} \cos\left(M_i\, \phi_{i,i+1}\right) d\sigma^{n-\mathrm{jet}} \tag{1}$$

[1] Another interesting and novel possibility, the detection of two charged light hadrons: $\pi^{\pm}$, $K^{\pm}$, p, $\bar{p}$ having high transverse momenta and separated by a large interval of rapidity, together with an undetected soft-gluon radiaton emission, was suggested in [22] and studied in [23].

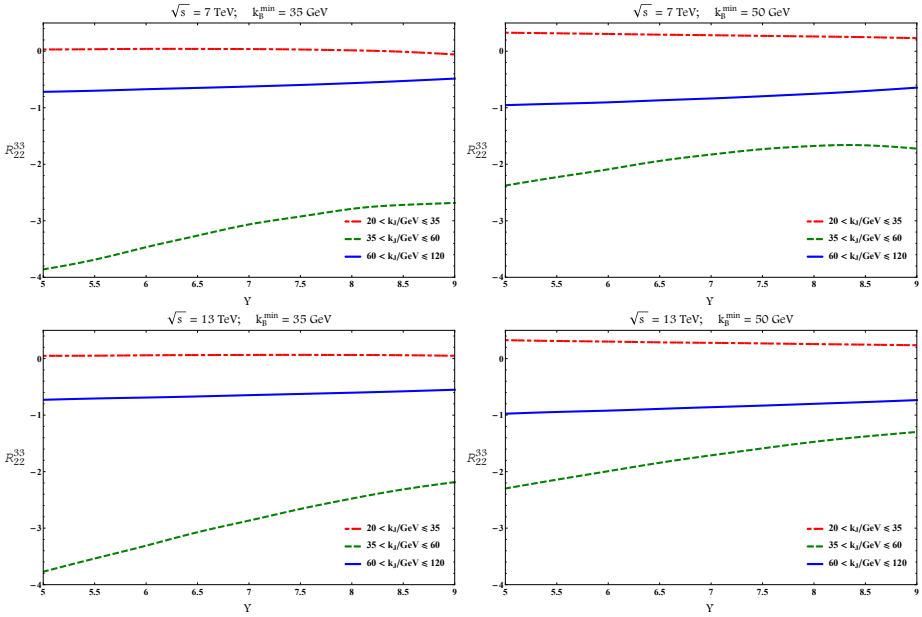

Figure 1: Y-dependence of R_{12}^{33} for $\sqrt{s} = 7, 13$ TeV and $k_{B,\min} = 35$ GeV (left column) and $k_{B,\min} = 50$ GeV (right column). $k_{A,\min}$ is equal to 35 GeV, while the rapidity of the central jet is fixed to $y_J = (y_A + y_B)/2$.

where $\phi_{i,i+1} = \theta_i - \theta_{i+1} - \pi$, and θ_i is the azimuthal angle of the jet i. From a phenomenological perspective, we want to provide predictions compatible with the current and future experimental data. To this purpose, we introduce the kinematical cuts already in place at the LHC by integrating $\mathcal{C}_{M_1 \cdots M_{n-1}}$ over the momenta of all tagged jets in the form

$$C_{M_1 \cdots M_{n-1}} = \int_{y_{1,\min}}^{y_{1,\max}} dy_1 \int_{y_{n,\min}}^{y_{n,\max}} dy_n \int_{k_{1,\min}}^{\infty} dk_1 \cdots \int_{k_{n,\min}}^{\infty} dk_n \delta\left(y_1 - y_n - Y\right) \mathcal{C}_n \quad (2)$$

where the most forward and the most backward jet rapidities are taken in the range delimited by $y_1^{\min} = y_n^{\min} = -4.7$ and $y_1^{\max} = y_n^{\max} = 4.7$, keeping their difference $Y = y_1 - y_n$ fixed. From a theoretical point of view, it is important to improve the stability of our predictions (see [29] for a related discussion). This can be done by removing the zeroth conformal spin contribution responsible for any collinear. For this reason, we introduce the ratios

$$R_{N_1 \cdots N_{n-1}}^{M_1 \cdots M_{n-1}} \equiv \frac{C_{M_1 \cdots M_{n-1}}}{C_{N_1 \cdots N_{n-1}}} \quad (3)$$

where $\{M_i\}$ and $\{N_i\}$ are positive integers.

We performed the numerical computation of the ratios $\mathcal{R}_{PQ}^{MN}$ both in FORTRAN and in MATHEMATICA (mainly for cross-checks). The NLO MSTW 2008 PDF sets [30] were used and for the strong coupling α_s we chose a two-loop running coupling setup with $\alpha_s(M_Z) = 0.11707$. We made extensive use of the integration routine `Vegas` [31] as implemented in the `Cuba` library [32, 33]. Furthermore, we used the `Quadpack` library [34] and a slightly modified version of the `Psi` [35] routine.

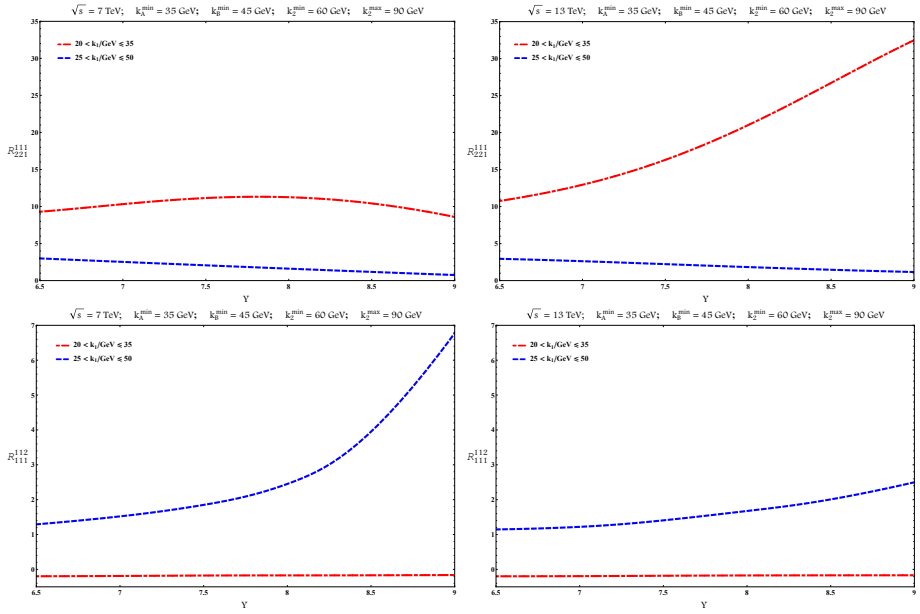

Figure 2: Y-dependence of R^{111}_{221} and R^{112}_{111} for $\sqrt{s} = 7$ TeV (left column) and for $\sqrt{s} = 13$ TeV (right column). The rapidity interval between a jet and the closest one is fixed to $Y/3$.

In Fig. 1 we show the dependence on Y of the R^{33}_{22} ratio, characteristic of the 3-jet process, for $\sqrt{s} = 7$ and 13 TeV, for two different kinematical cuts on the transverse momenta $k_{A,B}$ of the external jets and for three different ranges of the transverse momentum k_J of the central jet.

In Fig. 2 we show the dependence on Y of R^{111}_{221} and R^{112}_{111} ratios, characteristic of the 4-jet process, for $\sqrt{s} = 7$ and 13 TeV, for asymmetrical cuts on the transverse momenta $k_{A,B}$ of the external jets and for two different configurations of the central jet transverse momenta $k_{1,2}$.

A comparison with predictions for these observables from fixed order analyses as well as from the BFKL inspired Monte Carlo `BFKLex` [36, 37, 38, 39, 40, 41, 42] is underway.

3 Conclusions & Outlook

We studied ratios of correlation functions of products of azimuthal angle difference cosines in order to study three- and four-jet production at hadron colliders. The dependence on the transverse momenta and rapidities of the central jet(s) represent a clear signal of the BFKL dynamics. For future works, more accurate analyses are needed: higher order effects and study of different configurations for the rapidity range of the two central jets, together with the analysis of the effect of using different PDF parametrizations. It would be also interesting to calculate our observables using other approaches not based on the BFKL approach and to test how they differ from our predictions. The comparison with experimental data will help to disentangle the region of applicability of the BFKL approach, therefore we strongly encourage

experimental collaborations to study these observables in the next LHC analyses.

Acknowledgements

GC acknowledges support from the MICINN, Spain, under contract FPA2013-44773-P. DGG acknowledges financial support from 'la Caixa'-Severo Ochoa doctoral fellowship. ASV and DGG acknowledge support from the Spanish Government (MICINN (FPA2015-65480-P)) and, together with FC and FGC, to the Spanish MINECO Centro de Excelencia Severo Ochoa Programme (SEV-2012-0249). FGC thanks the Instituto de Física Teórica (IFT UAM-CSIC) in Madrid for warm hospitality.

References

[1] L.N. Lipatov, Sov. Phys. JETP **63** (1986) 904 [Zh. Eksp. Teor. Fiz. **90** (1986) 1536].

[2] I.I. Balitsky and L.N. Lipatov, Sov. J. Nucl. Phys. **28** (1978) 822 [Yad. Fiz. **28** (1978) 1597].

[3] E.A. Kuraev, L.N. Lipatov and V.S. Fadin, Sov. Phys. JETP **45** (1977) 199 [Zh. Eksp. Teor. Fiz. **72** (1977) 377].

[4] E.A. Kuraev, L.N. Lipatov and V.S. Fadin, Sov. Phys. JETP **44** (1976) 443 [Zh. Eksp. Teor. Fiz. **71** (1976) 840] [Erratum-ibid. **45** (1977) 199].

[5] L.N. Lipatov, Sov. J. Nucl. Phys. **23** (1976) 338 [Yad. Fiz. **23** (1976) 642].

[6] V.S. Fadin, E.A. Kuraev and L.N. Lipatov, Phys. Lett. B **60** (1975) 50.

[7] V.S. Fadin and L.N. Lipatov, Phys. Lett. B **429** (1998) 127 [hep-ph/9802290].

[8] M. Ciafaloni and G. Camici, Phys. Lett. B **430** (1998) 349 [hep-ph/9803389].

[9] M. Hentschinski, A. Sabio Vera and C. Salas, Phys. Rev. Lett. **110** (2013) 041601 [arXiv:1209.1353 [hep-ph]].

[10] M. Hentschinski, A. Sabio Vera and C. Salas, Phys. Rev. D **87** (2013) 076005 [arXiv:1301.5283 [hep-ph]].

[11] A.H. Mueller and H. Navelet, Nucl. Phys. B **282** (1987) 727.

[12] A. Sabio Vera, Nucl. Phys. B **746** (2006) 1 [hep-ph/0602250].

[13] A. Sabio Vera and F. Schwennsen, Nucl. Phys. B **776** (2007) 170 [hep-ph/0702158 [HEP-PH]].

[14] B. Ducloue, L. Szymanowski and S. Wallon, Phys. Rev. Lett. **112** (2014) 082003 [arXiv:1309.3229 [hep-ph]].

[15] F. Caporale, D.Y. Ivanov, B. Murdaca and A. Papa, Eur. Phys. J. C **74** (2014) 3084 [arXiv:1407.8431 [hep-ph]].

[16] F. Caporale, D.Y. Ivanov, B. Murdaca and A. Papa, Phys. Rev. D **91** (2015) no.11, 114009 doi:10.1103/PhysRevD.91.114009 [arXiv:1504.06471 [hep-ph]].

[17] F.G. Celiberto, D. Y. Ivanov, B. Murdaca and A. Papa, Eur. Phys. J. C **75** (2015) no.6, 292 [arXiv:1504.08233 [hep-ph]].

[18] F.G. Celiberto, D. Y. Ivanov, B. Murdaca and A. Papa, Eur. Phys. J. C **76** (2016) no.4, 224 [arXiv:1601.07847 [hep-ph]].

[19] R. Ciesielski, arXiv:1409.5473 [hep-ex].

[20] M. Angioni, G. Chachamis, J.D. Madrigal and A. Sabio Vera, Phys. Rev. Lett. **107**, 191601 (2011) [arXiv:1106.6172 [hep-th]].

[21] G. Chachamis, arXiv:1512.04430 [hep-ph].

[22] D.Y. Ivanov and A. Papa, JHEP **1207** (2012) 045 [arXiv:1205.6068 [hep-ph]].

[23] F.G. Celiberto, D.Y. Ivanov, B. Murdaca and A. Papa, Phys. Rev. D **94** (2016) no.3, 034013 doi:10.1103/PhysRevD.94.034013 [arXiv:1604.08013 [hep-ph]].

[24] F. Caporale, G. Chachamis, B. Murdaca and A. Sabio Vera, Phys. Rev. Lett. **116** (2016) no.1, 012001 [arXiv:1508.07711 [hep-ph]].

[25] F. Caporale, F.G. Celiberto, G. Chachamis, D. Gordo Gómez and A. Sabio Vera, Nucl. Phys. B **910** (2016) 374 doi:10.1016/j.nuclphysb.2016.07.012 [arXiv:1603.07785 [hep-ph]].

[26] F. Caporale, F.G. Celiberto, G. Chachamis and A. Sabio Vera, Eur. Phys. J. C **76** (2016) no.3, 165 [arXiv:1512.03364 [hep-ph]].

[27] F. Caporale, F.G. Celiberto, G. Chachamis, D.G. Gomez and A. Sabio Vera, arXiv:1606.00574 [hep-ph].

[28] F.G. Celiberto, arXiv:1606.07327 [hep-ph].

[29] F. Caporale, B. Murdaca, A. Sabio Vera and C. Salas, Nucl. Phys. B **875** (2013) 134 [arXiv:1305.4620 [hep-ph]].

[30] A.D. Martin, W.J. Stirling, R.S. Thorne and G. Watt, Eur. Phys. J. C **63** (2009) 189 [arXiv:0901.0002 [hep-ph]].

[31] G.P. Lepage, J. Comput. Phys. **27** (1978) 192.

[32] T. Hahn, Comput. Phys. Commun. **168** (2005) 78 [arXiv:1408.6373 [hep-ph]].

[33] T. Hahn, J. Phys. Conf. Ser. **608** (2015) 1 [arXiv:hep-ph/0404043].

[34] R. Piessens, E. De Doncker-Kapenga and C.W. Überhuber, Springer, ISBN: 3-540-12553-1, 1983.

[35] W.J. Cody, A.J. Strecok and H.C. Thacher, Math. Comput. **27** (1973) 121.

[36] G. Chachamis, M. Deak, A. Sabio Vera and P. Stephens, Nucl. Phys. B **849** (2011) 28 [arXiv:1102.1890 [hep-ph]].

[37] G. Chachamis and A. Sabio Vera, Phys. Lett. B **709** (2012) 301 [arXiv:1112.4162 [hep-th]].

[38] G. Chachamis and A. Sabio Vera, Phys. Lett. B **717** (2012) 458 [arXiv:1206.3140 [hep-th]].

[39] G. Chachamis, A. Sabio Vera and C. Salas, Phys. Rev. D **87** (2013) 1, 016007 [arXiv:1211.6332 [hep-ph]].

[40] F. Caporale, G. Chachamis, J.D. Madrigal, B. Murdaca and A. Sabio Vera, Phys. Lett. B **724** (2013) 127 [arXiv:1305.1474 [hep-th]].

[41] G. Chachamis and A. Sabio Vera, arXiv:1511.03548 [hep-ph].

[42] G. Chachamis and A. Sabio Vera, JHEP **1602** (2016) 064 doi:10.1007/JHEP02(2016)064 [arXiv:1512.03603 [hep-ph]].

Double-parton scattering effects in double charm production within gluon fragmentation scenario

Rafał Maciuła[1], Antoni Szczurek[1,2],

[1]Institute of Nuclear Physics PAN, PL-31-342 Kraków, Poland
[2]University of Rzeszów, PL-35-959 Rzeszów, Poland

August 9, 2017

Abstract

We discuss charm D^0D^0 meson-meson pair production in the forward rapidity region related to the LHCb experimental studies at $\sqrt{s} = 7$ TeV. We consider double-parton scattering mechanisms of double $c\bar{c}$ production and subsequent standard $cc \to D^0D^0$ scale-independent hadronization as well as new double g and mixed $gc\bar{c}$ production mechanisms with $gg \to D^0D^0$ and $gc \to D^0D^0$ scale-dependent hadronization. The new scenario with gluon fragmentation components results also in a new single-parton scattering mechanism of gg production which is also taken here into account. Results of the numerical calculations are compared with the LHCb data for several correlation observables. The new mechanisms lead to a larger cross sections and to slightly different shapes of the calculated correlation observables.

1 Introduction

Some time ago we have predicted that at large energies, relevant for the LHC, production of double charm should be dominated by the double-parton scattering (DPS) mechanism [1]. Afterwards, those leading-order (LO) collinear predictions were extended to the k_t-factorization approach that effectively includes higher-order QCD effects [2, 3]. The improved studies provide a relatively good description of the LHCb experimental data [4]. Besides, the single-parton scattering (SPS) $gg \to c\bar{c}c\bar{c}$

mechanism was found to be much smaller than the DPS one, and is not able to explain the LHCb double charm data [3, 5].

The theoretical analyses introduced above were based on the standard $c \to D$ hadronization scenario with scale-independent Peterson fragmentation function (FF) [6]. An alternative approach for hadronization effects is to apply scale-dependent FFs of a parton (gluon, $u, d, s, \bar{u}, \bar{d}, \bar{s}, c, \bar{c}$) to D mesons proposed by Kniehl et al. [7, 8], that undergo DGLAP evolution equations. Both prescriptions were found to provide a very good description of the LHC data on inclusive D meson production at not too small transverse momenta (see e.g. Refs. [9, 10]). In the latter approach, a dominant contribution comes from $g \to D$ fragmentation that appears in the evolution of the scale-dependent FFs and the $c \to D$ component is damped with respect to the scale-independent fragmentation scheme.

The presence of the gluonic components modify the overall picture for the double charm production. In the (new) scenario with scale-dependent hadronization the number of contributing DPS processes grows. In addition, a new single-parton scattering mechanism SPS $gg \to DD$ appears. Taking into account gluon fragmentation components there are more processes for single D meson production (two dominant components $g, c \to D$) and as a consequence many more processes for DPS DD production appear. Now there are three classes of DPS contributions. In addition to the coventional DPS $cc \to DD$, discussed very carefully in Refs. [2, 3, 5] there is a double $g \to D$ fragmentation mechanism, called here DPS $gg \to DD$ as well as the mixed DPS $gc \to DD$ contribution.

Here the gluon and digluon production is considered in the k_t-factorization approach with reggeized gluons in the t-channel [11] via subprocesses $RR \to g$ and $RR \to gg$, where R is the reggeized gluon. We use scale-dependent fragmentation functions of Kneesch-Kniehl-Kramer-Schienbein (KKKS08) [12] as implemented in the code available on the Web [13]. All details of the calculations presented here can be found in our original paper [14].

2 A sketch of the theoretical formalism

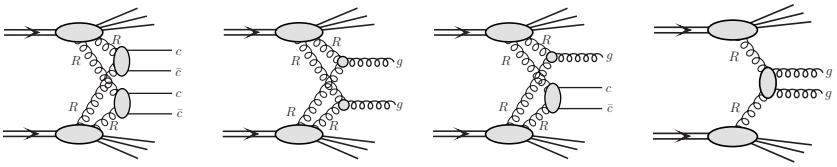

Figure 1: A diagrammatic illustration of the considered mechanisms.

We will compare numerical results for $D^0 D^0$ meson-meson production obtained with the two different fragmentation scenarios. According to the scheme with scale-dependent FFs more processes for single D meson production (c and $g \to D$ components) has to be taken into consideration. This also causes an extension of the standard DPS DD pair production by new mechanisms. In addition to the coventional DPS $cc \to DD$ (left diagram in Fig.1) considered in Refs. [2, 3, 5] there is a double $g \to D$ (or double $g \to \bar{D}$) fragmentation mechanism, called here DPS $gg \to DD$ (middle-left diagram in Fig.1) as well as the mixed DPS $gc \to DD$ contribution (middle-right diagram in Fig.1).

As a consequence of the new approach to fragmentation a new SPS $gg \to DD$ mechanism shows up (right diagram in Fig.1). In this case the two produced gluons are correlated in azimuth and the mechanism will naturally lead to an azimuthal correlation between two D mesons. Such a correlation was actually observed in the LHCb experimental data [4] and so far could not be explained theoretically.

DPS cross section for production of cc, gg or gc system, assuming factorization of the DPS model, can be written as:

$$\frac{d\sigma^{DPS}(pp \to ccX)}{dy_1 dy_2 d^2p_{1,t} d^2p_{2,t}} = \frac{1}{2\sigma_{eff}} \cdot \frac{d\sigma^{SPS}(pp \to c\bar{c}X_1)}{dy_1 d^2p_{1,t}} \cdot \frac{d\sigma^{SPS}(pp \to c\bar{c}X_2)}{dy_2 d^2p_{2,t}}, \quad (1)$$

$$\frac{d\sigma^{DPS}(pp \to ggX)}{dy_1 dy_2 d^2p_{1,t} d^2p_{2,t}} = \frac{1}{2\sigma_{eff}} \cdot \frac{d\sigma^{SPS}(pp \to gX_1)}{dy_1 d^2p_{1,t}} \cdot \frac{d\sigma^{SPS}(pp \to gX_2)}{dy_2 d^2p_{2,t}}. \quad (2)$$

$$\frac{d\sigma^{DPS}(pp \to gcX)}{dy_1 dy_2 d^2p_{1,t} d^2p_{2,t}} = \frac{1}{\sigma_{eff}} \cdot \frac{d\sigma^{SPS}(pp \to gX_1)}{dy_1 d^2p_{1,t}} \cdot \frac{d\sigma^{SPS}(pp \to c\bar{c}X_2)}{dy_2 d^2p_{2,t}}. \quad (3)$$

The often called pocket-formula is a priori a severe approximation. The flavour, spin and color correlations may lead, in principle, to interference effects that result in its violation as discussed e.g. in Ref. [15]. Even for unpolarized proton beams, the spin polarization of the two partons from one hadron can be mutually correlated, especially when the partons are relatively close in phase space (having comparable x's). Moreover, in contrast to the standard single PDFs, the two-parton distributions have a nontrivial color structure which also may lead to a non-negligible correlations effects. Such effects are usually not included in phenomenological analyses. They were exceptionally discussed in the context of double charm production [16]. However, the effect on e.g. azimuthal correlations between charmed quarks was found there to be very small, much smaller than effects of the SPS contribution associated with double gluon fragmentation discussed here. In addition, including perturbative parton splitting mechanism also leads to a breaking of the pocket-formula [17]. This formalism was so far formulated for the collinear leading-order approach which for charm (double charm) may be a bit academic as it leads to underestimation of the cross section. Imposing sum rules also leads to a breaking of the factorized Ansatz but the effect almost vanishes for small longitudinal momentum fractions [18]. Taken the above arguments we will use the pocket-formula in the following.

All the considered mechanisms (see Fig. 1) are calculated in the k_t-factorization approach with off-shell initial state partons and unintegrated (k_t-dependent) PDFs (unPDFs). Fully gauge invariant treatment of the initial-state off-shell gluons and quarks can be achieved in the k_t-factorization approach only when they are considered as Reggeized gluons or Reggeons. We use the LO Kimber-Martin-Ryskin (KMR) unPDFs, generated from the LO set of a up-to-date MMHT2014 collinear PDFs fitted also to the LHC data (for more details see Ref.[14]).

3 Comparison to the LHCb data

We start this section with a revision of inclusive single D^0 meson production measured some time ago by the LHCb collaboration [19]. We compare here corresponding theoretical predictions based on both, the first (only $c \to D$) [9] and the second

$(c + g \to D)$ scenario [10], keeping the same set of α_S, scales, unPDFs and other details. This comparison is crucial for drawing definite conclusions from double D meson production. As shown in Fig. 2, both prescriptions give a very good description of the LHCb experimental data. Some small differences between them can be observed for both very small and large meson transverse momenta. The latter effect can be relatd to the DGLAP evolution which makes the slope of the transverse momentum distribution in the second scenario a bit steeper. In the region of very small p_t's the second scenario gives larger cross sections and slightly overestimates the experimental data points. This may come from the $g \to D$ fragmentation component which approaches a problematic region when $p_t \sim 2m_c$. Then the treatment of charm quarks as massless in the DGLAP evolution of fragmentation function for very small evolution scale can be a bit questionable and may lead to a small overestimation of the integrated cross sections.

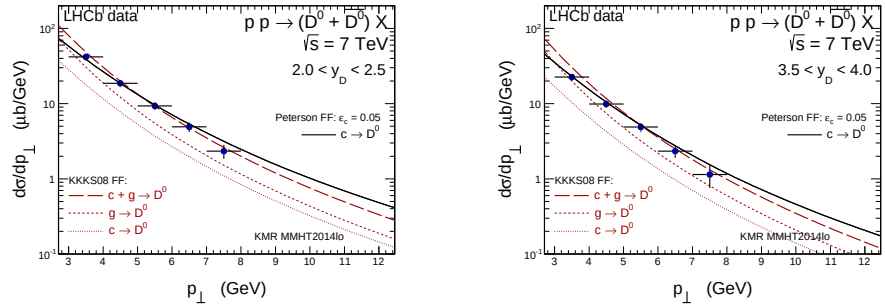

Figure 2: Charm meson transverse momentum distribution within the LHCb acceptance for inclusive single D^0 mesons (plus their conjugates) production. The left and right panels correspond to two different rapidity intervals. Theoretical predictions for the Peterson $c \to D$ fragmentation function (solid lines) are compared to the second scenario calculations with the KKKS08 fragmentation functions (long-dashed lines) with $c \to D$ (dotted) and $g \to D$ (short-dashed) components that undergo DGLAP evolution equation.

Now we go to double charm meson D^0D^0 production. In Fig. 3 we compare results of our calculation with experimental distribution in transverse momentum of one of the meson from the D^0D^0 (or $\bar{D}^0\bar{D}^0$) pair. We show results for the first scenario when standard Peterson FF is used for the $c \to D^0$ (or $\bar{c} \to \bar{D}^0$) fragmentation (left panel) as well as the result for the second scenario when the KKKS08 FFs with DGLAP evolution for $c \to D^0$ (or $\bar{c} \to \bar{D}^0$) and $g \to D^0$ (or $g \to \bar{D}^0$) are used. One can observe that the DPS $cc \to D^0D^0$ contribution in the new scenario is much smaller than in the old scenario. In addition, the slope of the distribution in transverse momentum changes. Both the effects are due to evolution of corresponding fragmentation functions. The different new mechanisms give contributions of similar size. We can obtain an agreement in the second case provided σ_{eff} parameter is increased from conventional 15 mb to 30 mb. Even then we overestimate the LHCb data for $3 < p_T < 5$ GeV. Possible effects that may result in larger value of σ_{eff} and in its transverse momentum dependence are discussed in our original paper [14].

In Fig. 4 we show dimeson invariant mass distribution $M_{D^0D^0}$ again for the two cases considered. In the first scenario we get a good agreement only for small

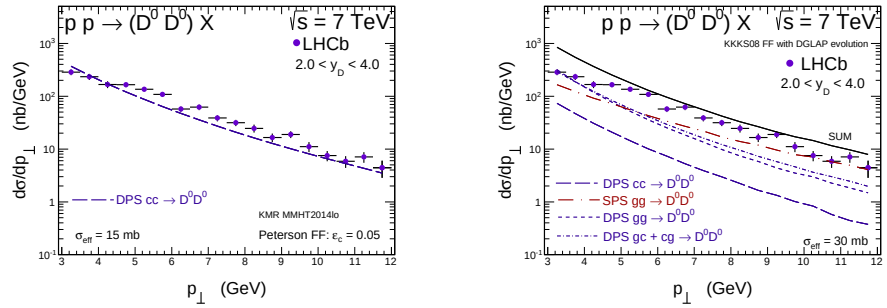

Figure 3: D^0 meson transverse momentum distribution within the LHCb acceptance region. The left panel is for the first scenario and for the Peterson $c \to D$ fragmentation function while the right panel is for the second scenario and for the fragmentation function that undergo DGLAP evolution equation.

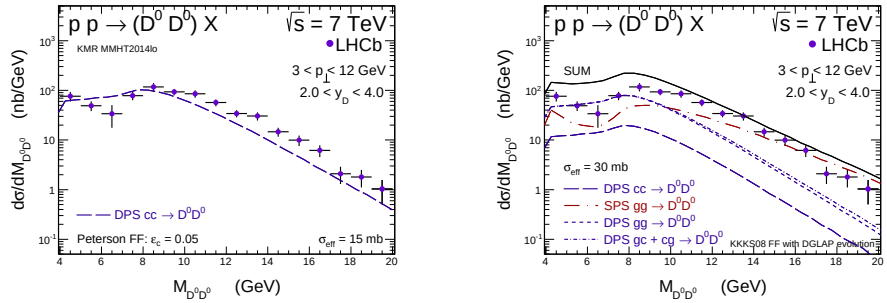

Figure 4: $M_{D^0D^0}$ dimeson invariant mass distribution within the LHCb acceptance region. The left panel is for the first scenario and for the Peterson $c \to D$ fragmentation function while the right panel is for the second scenario and for the fragmentation function that undergo DGLAP evolution equation.

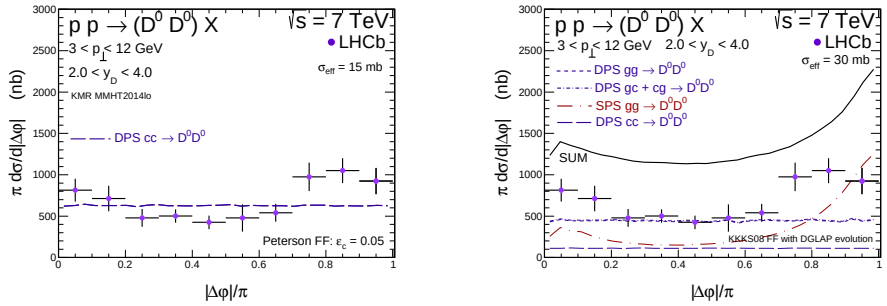

Figure 5: Distribution in azimuthal angle $\varphi_{D^0D^0}$ between the two D^0 mesons within the LHCb acceptance region. The left panel is for the first scenario and for the Peterson $c \to D$ fragmentation function while the right panel is for the second scenario and for the fragmentation function that undergo DGLAP evolution equation.

invariant masses while in the second scenario we get a good agreement only for

large invariant masses. The large invariant masses are strongly correlated with large transverse momenta, so the situation here (for the invariant mass distribution) is quite similar as in Fig. 3 for the transverse momentum distribution.

In Fig. 5 we show azimuthal angle correlation $\varphi_{D^0 D^0}$ between D^0 and D^0 (or $\bar{D}^0$ and $\bar{D}^0$ mesons). While the correlation function in the first scenario is completely flat, the correlation function in the second scenario shows some tendency similar as in the experimental data.

To summarize the present situation for the second scenario, in Fig. 6 we show again the azimuthal angle distribution discussed above for different values of σ_{eff}. Good description can be obtained only for extremely large values of σ_{eff} which goes far beyond the geometrical picture [17] and that are much larger than for other reactions and in this sense is inconsistent with the factorized Ansatz. We think that the solution of the inconsistency is not only in the DPS sector as already discussed in this paper.

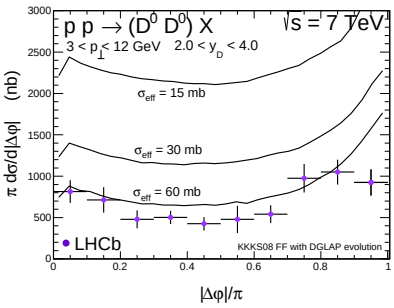

Figure 6: The dependence of the results of the second scenario on the parameter σ_{eff} used in the calculation of the DPS contributions. Here the three lines correspond to σ_{eff} equal to 15, 30, and 60 mb, from top to bottom, respectively.

4 Conclusions

The new scenario with scale-dependent FFs for double D meson production give similar result as the first scenario with one fragmentation subprocess ($cc \to DD$) and fixed (scale-independent) FFs. However, correlation observables, such as dimeson invariant mass or azimuthal correlations between D mesons, are slightly better described in the second scenario as long as we consider only their shapes. However, to get the proper normalization of the cross sections calculated within the second scenario a much larger value of σ_{eff} is needed.

The observed overestimation of the correlation observables in the second scenario comes from the region of small transverse momenta. It may be related to the fact that the fragmentation function used in the new scenario were obtained in the DGLAP formalism with massless c quarks and $\bar{c}$ antiquarks which may be a too severe approximation, especially for low factorization scales (i.e. low transverse momenta) for fragmentation functions. On the other hand, the situation can be also improved when a proper transverse momentum dependence of σ_{eff} and/or when perturbative-parton-splitting mechanisms will be included, but this needs further studies.

Acknowledgments

We thank V. A. Saleev and A. V. Shipilova for collaboration in obtaining results presented here. This study was partially supported by the Polish National Science Center grant DEC-2014/15/B/ST2/02528.

References

[1] M. Łuszczak, R. Maciuła and A. Szczurek, Phys. Rev. D **85**, 094034 (2012)

[2] R. Maciuła and A. Szczurek, Phys. Rev. D **87**, 074039 (2013)

[3] A. van Hameren, R. Maciuła and A. Szczurek, Phys. Rev. D **89**, 094019 (2014)

[4] R. Aaij *et al.* [LHCb Collaboration], JHEP **1206**, 141 (2012); [**03**, 108 (2014)]

[5] A. van Hameren, R. Maciuła and A. Szczurek, Phys. Lett. B **748**, 167 (2015)

[6] C. Peterson *et al.*, Phys. Rev. D **27**, 105 (1983)

[7] B. A. Kniehl and G. Kramer, Phys. Rev. D **71**, 094013 (2005)

[8] B. A. Kniehl and G. Kramer, Phys. Rev. D **74**, 037502 (2006)

[9] R. Maciula and A. Szczurek, Phys. Rev. D **87**, 094022 (2013)

[10] A. Karpishkov *et al.*, Phys. Rev. D **91**, 054009 (2015)

[11] M. A. Nefedov, V. A. Saleev and A. V. Shipilova, Phys. Rev. D **87**, 094030 (2013)

[12] T. Kneesch *et al.*, Nucl. Phys. B **799**, 34 (2008)

[13] KKKS08-package: http://lapth.cnrs.fr/ffgenerator/

[14] R. Maciuła, V. A. Saleev, A. V. Shipilova and A. Szczurek, Phys. Lett. B **758**, 458 (2016)

[15] M. Diehl, D. Ostermeier and A. Schafer, JHEP **1203**, 089 (2012).

[16] M. G. Echevarria, T. Kasemets, P. J. Mulders and C. Pisano, JHEP **1504**, 034 (2015).

[17] J. R. Gaunt, R. Maciula and A. Szczurek, Phys. Rev. D **90**, 054017 (2014).

[18] K. Golec-Biernat, et al., Phys. Lett. B **750**, 559 (2015).

[19] R. Aaij *et al.* [LHCb Collaboration], Nucl. Phys. B **871**, 1 (2013).

Four-jet production in the k_t-factorisation

Antoni Szczurek[1,2], Rafal Maciula[1]

[1]Institute of Nuclear Physics PAN, PL-31-342 Kraków, Poland
[2]University of Rzeszów, PL-35-959 Rzeszów, Poland

August 9, 2017

Abstract

We discuss the single-parton and double-parton scattering (SPS or DPS) effects in four-jet production at the LHC. The calculations of both single-parton and double-parton scattering components are done in the high-energy (or k_T)-factorization approach. Here we follow our recent developments of relevant methods and tools. The calculations are performed for kinematical situations relevant for two experimental measurements (ATLAS and CMS) at the LHC. We compare our results to those reported by the ATLAS and CMS collaborations for different sets of kinematical cuts. A special attention is given to the optimization of kinematical conditions in order to enhance the relative contribution of DPS in four-jet sample. Several differential distributions are calculated and carefully discussed in the context of recent and future searches for DPS effects at the LHC. The dependences of the relative DPS amount is studied as a function of rapidity of jets, rapidity distance, and various azimuthal correlations between jets. The regions with an enhanced DPS contribution are identified.

1 Introduction

So far, complete four-jet production via single-parton scattering (SPS) was discussed only within collinear factorization. Results up to next-to-leading (NLO) precision can be found in [1, 2]. Recently we discussed for the first time production of four jets within high-energy (k_T-)factorization (HEF) approach with $2 \to 4$ subproceses with two off-shell partons [3].

Four-jet production seems a natural case to look for hard double-parton scattering (DPS) effects (see e.g. Ref. [4] and references therein). Some time ago we analyzed how to find optimal conditions for the observation and exploration of DPS effects in four-jet production [5]. In this analysis only the leading-order (LO) collinear approach was applied both to single and double-parton scattering mechanisms.

Very recently, we have performed for the first time a calculation of four-jet production for both single-parton and double-parton mechanism within k_T-factorization [3]. It was shown that the effective inclusion of higher-order effects leads to a substantial damping of the double-scattering contribution with respect to the SPS one, especially for symmetric (identical) cuts on the transverse momenta of all jets.

So far, most practical calculations of DPS contributions were performed within the so-called factorized ansatz. In this approach, the cross section for DPS is a product of the corresponding cross sections for single-parton scatterings (SPS). This is a phenomenologically motivated approximation which is not well under control yet. A better formalism exists in principle, but predictions are not easy, as they require unknown input(s), *e.g.* double-parton distributions that should contain informations about space-configuration, spin, colour or flavour correlations between the two partons in one hadron [6]. These objects are explored to a far lesser extent than the standard single PDFs. However, the factorized model seems to be a reasonable tool to collect empirical facts to draw useful conclusions about possible identification of the DPS effects in several processes.

As discussed in Ref. [5], jets with low cuts on the transverse momenta and a large rapidity separation seem more promissing in exploring DPS effects in four-jet production. In the following we shall show our recent results for SPS and DPS calculations obtained for first time in k_T-factorization approach and concentrate on the study of optimal observables to pin down DPS contributions.

2 A sketch of the theoretical formalism

The theoretical formalism used to obtain the following predictions was discussed in detail in [3]. All details related to the scattering amplitudes with off-shell initial state partons as well as with the Transverse Momentum Dependent or unintegrated parton distribution functions (TMDs) can be found in our original paper.

Here we only very briefly recall the basic high-energy (or k_T)-factorization (HEF) formula for the calculation of the inclusive partonic four-jet cross section:

$$\sigma^B_{4-jets} = \sum_{i,j} \int \frac{dx_1}{x_1}\,\frac{dx_2}{x_2}\,d^2k_{T1} d^2k_{T2}\,\mathcal{F}_i(x_1,k_{T1},\mu_F)\,\mathcal{F}_j(x_2,k_{T2},\mu_F)$$
$$\times \frac{1}{2\hat{s}} \prod_{l=i}^{4} \frac{d^3k_l}{(2\pi)^3 2E_l} \Theta_{4-jet}\,(2\pi)^4\,\delta\left(x_1P_1 + x_2P_2 + \vec{k}_{T\,1} + \vec{k}_{T\,2} - \sum_{l=1}^{4} k_i\right) \overline{\left|\mathcal{M}(i^*,j^* \to 4\,\text{part.})\right|^2}\,. \tag{2.1}$$

Above $\mathcal{F}_i(x_k,k_{Tk},\mu_F)$ is the TMD for a given parton type, x_k are the longitudinal momentum fractions, μ_F is a factorization scale, $\vec{k}_{Tk}$ the parton's transverse momenta. $\mathcal{M}(i^*,j^* \to 4\,\text{part.})$ is the gauge invariant matrix element for $2 \to 4$ particle scattering with two initial off-shell partons. They are evaluated numerically

with the help of the AVHLIB [7] Monte Carlo library. In the calculation, the scales are set to $\mu_F = \mu_R = \frac{\hat{H}_T}{2} = \frac{1}{2}\sum_{l=1}^{4} k_T^l$ [1].

The so-called pocket formula for DPS cross sections (for a four-parton final state) reads:

$$\frac{d\sigma^B_{4-jet,DPS}}{d\xi_1 d\xi_2} = \frac{m}{\sigma_{eff}} \sum_{i_1,j_1,k_1,l_1;i_2,j_2,k_2,l_2} \frac{d\sigma^B(i_1 j_1 \to k_1 l_1)}{d\xi_1} \frac{d\sigma^B(i_2 j_2 \to k_2 l_2)}{d\xi_2}, \tag{2.2}$$

where the $\sigma(ab \to cd)$ cross sections are obtained by restricting (2.1) to a single channel and the symmetry factor m is $1/2$ if the two hard scatterings are identical, to avoid double counting. Finally, ξ_1 and ξ_2 stand for generic kinematical variables for the first and second scattering, respectively. The effective cross section σ_{eff} can be interpreted as a measure of correlation in the transverse plane of the two partons inside the hadrons, whereas the possible longitudinal correlations are usually neglected. In the numerical calculations here we use $\sigma_{eff} = 15$ mb that is a typical value known from the world systematics [8].

3 Selected results

First we show some selected examples of the results of the k_T-factorization calculation in Figs. 1 and 2. In this calculations we used the KMR unintegrated parton distributions. The prediction is consistent with the ATLAS data for all the p_T distributions.

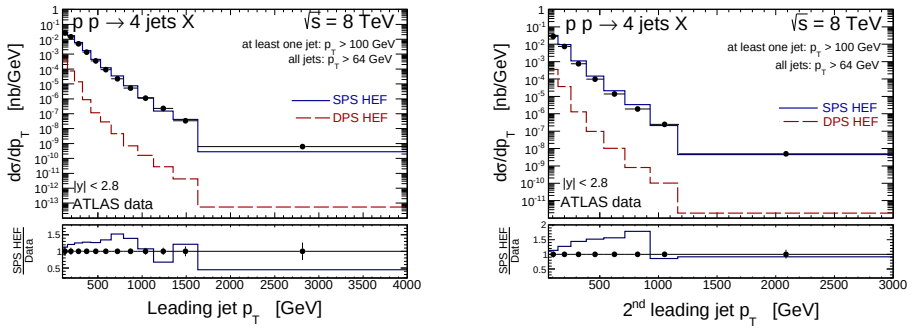

Figure 1: k_T-factorization prediction of the differential cross sections w.r.t. the transverse momenta of the first two leading jets compared to the ATLAS data [11]. The LO calculation describes the data pretty well in this hard regime in which MPIs are irrelevant. In addition we show the ratio of the SPS HEF result to the ATLAS data.

Not only transverse momentum dependence is interesting. The CMS collaboration extracted for instance a more complicated observables [9]. One of them, which involves all four jets in the final state, is the ΔS variable, defined in Ref. [9] as the angle between pairs of the harder and the softer jets,

$$\Delta S = \arccos\left(\frac{\vec{p}_T(j_1^{\text{hard}}, j_2^{\text{hard}}) \cdot \vec{p}_T(j_1^{\text{soft}}, j_2^{\text{soft}})}{|\vec{p}_T(j_1^{\text{hard}}, j_2^{\text{hard}})| \cdot |\vec{p}_T(j_1^{\text{soft}}, j_2^{\text{soft}})|}\right), \tag{3.1}$$

[1] We use the $\hat{H}_T$ notation to refer to the energies of the final state partons, not jets, despite this is obviously the same in a LO analysis.

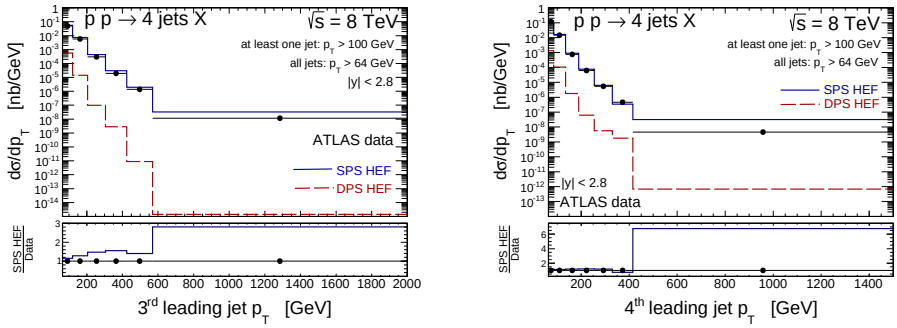

Figure 2: k_T-factorization approach prediction of the differential cross sections w.r.t. the transverse momenta of the 3rd and 4th leading jets compared to the ATLAS data [11]. The LO calculation describes the data pretty well in this hard regime in which MPIs are irrelevant. In addition we show the ratio of the SPS HEF result to the ATLAS data.

where $\vec{p}_T(j_i, j_k)$ stands for the sum of the transverse momenta of the two jets in arguments.

In Fig. 3 we present our HEF prediction for the normalized to unity distribution in the ΔS variable. Our HEF result approximately agrees with the experimental ΔS distribution. In contrast, the LO collinear approach leads to $\Delta S = 0$, i.e. a Kronecker-delta peak at $\Delta S = 0$ for the distribution in ΔS.

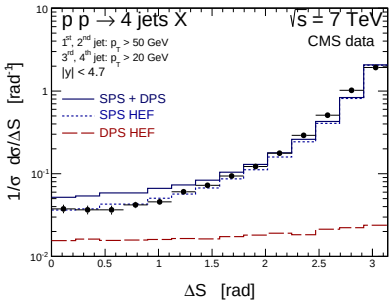

Figure 3: Comparison of the HEF predictions to the CMS data for ΔS spectrum.

Now we wish to show a comparison of our numerical predictions with existing experimental data for relatively low cuts on jet transverse momenta. In this context, the CMS experimental multi-jet analysis [9] is the most relevant as it uses sufficiently soft cuts on the jet transverse momenta. The cuts are in this case $|p_T| > 50$ GeV for the two hardest jets and $|p_T| > 20$ GeV for the third and fourth ones; the rapidity region is defined by $|\eta| < 4.7$ and the constraint on the jet cone radius parameter is $\Delta R > 0.5$. The overall situation is shown in Fig. 4, where we plot rapidity distributions for leading and subleading jets ordered by their p_T's.

The k_T-factorization approach includes higher-order corrections through the resummation in the TMDs. However, within this framework fixed-order loop effects are not taken into account. Therefore, we allow for a K-factor for the calculation

of the SPS component. The NLO K-factors are known to be smaller than unity for 3- and 4-jet production in the collinear approximation case [1]. To describe the CMS data, we also need K-factors smaller than unity for the SPS contributions, as expected. In contrast to the 4-jet case, the NLO predictions for the 2-jet inclusive cross section are further away from the measured value than the LO ones [1]. The 2-jet K-factor is known to be about 1.2, and it enters squared in the case of the DPS calculations. However, in our calculations we ignored the relatively small K-factors for the DPS contribution.

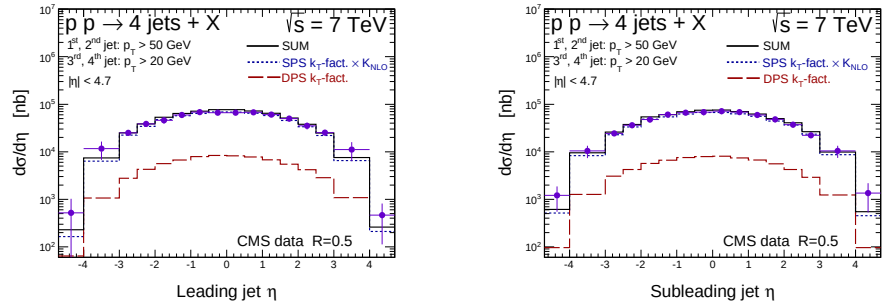

Figure 4: Rapidity distribution of the leading and subleading jets. The SPS contribution is shown by the dotted line while the DPS contribution by the dashed line.

In Refs. [4, 5] we introduced a set of observables that we find particularly convenient to identify DPS effects in four-jet production. Here we present results for completely symmetric cuts, $p_T > 20$ GeV, for all the four leading jets. The cuts on rapidity and jet radius parameter are the same as for the CMS case. In Fig. 5 we show our predictions for the rapidity distributions. In contrast to the previous case (Fig. 4), where harder cuts on the two hardest jets were used, the shapes of the SPS and DPS rapidity distributions are rather similar. There is only a small relative enhancement of the DPS contribution for larger jet rapidities.

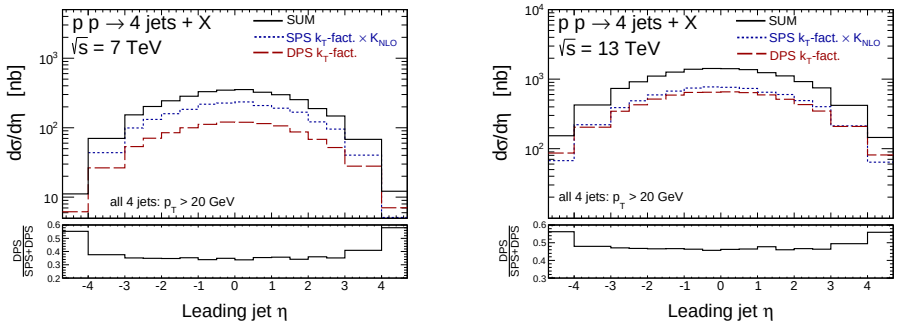

Figure 5: Rapidity distribution of leading jet for $\sqrt{s} = 7$ TeV (left column) and $\sqrt{s} = 13$ TeV (right column) for the symmetric cuts. The SPS contribution is shown by the dotted line while the DPS contribution by the dashed line. The relative contribution of DPS is shown in the extra lower panels.

As it was proposed first in Ref. [10] in the context of Mueller-Navelet jet production, and then repeated in Ref. [5] for four-jet studies in the LO collinear approach,

there are two potentially useful observables for DPS effects, such as the maximum rapidity distance

$$\Delta Y \equiv max_{\substack{i,j\in\{1,2,3,4\}\\ i\neq j}} |\eta_i - \eta_j| \tag{3.2}$$

and the azimuthal correlations between the jets which are most remote in rapidity

$$\varphi_{jj} \equiv |\varphi_i - \varphi_j|\,, \quad \text{for} \quad |\eta_i - \eta_j| = \Delta Y\,. \tag{3.3}$$

One can see in Fig. 6 that the relative DPS contribution increases with ΔY which, for the CMS collaboration is up to 9.4. At $\sqrt{s} = 13$ TeV the DPS component dominates over the SPS contribution for $\Delta Y > 6$. A potential failure of the SPS contribution to describe such a plot in this region would be a signal of the presence of a sizable DPS contribution.

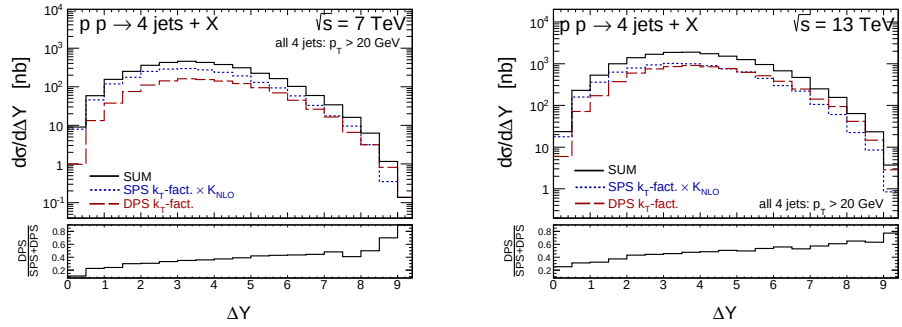

Figure 6: Distribution in rapidity distance between the most remote jets for the symmetric cut with $p_T > 20$ GeV for $\sqrt{s} = 7$ TeV (left) and $\sqrt{s} = 13$ TeV (right). The SPS contribution is shown by the dotted line while the DPS contribution by the dashed line. The relative contribution of DPS is shown in the extra lower panels.

Figure 7 shows azimuthal correlations between the jets most remote in rapidity. While at $\sqrt{s} = 7$ TeV the SPS contribution is always larger than the DPS one, at $\sqrt{s}$ = 13 TeV the DPS component dominates over the SPS contribution for $\varphi_{jj} < \pi/2$.

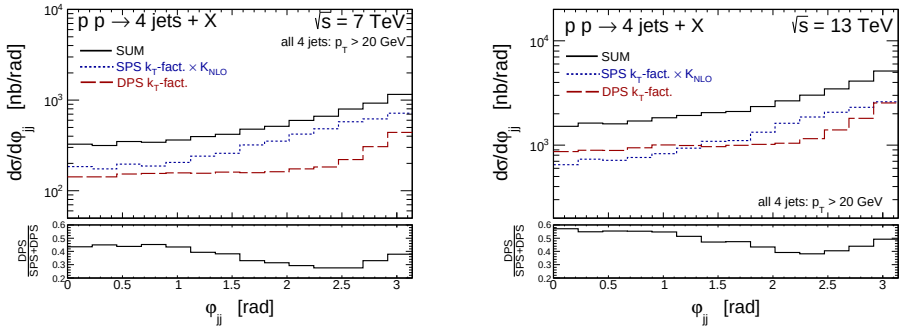

Figure 7: Distribution in relative azimuthal angle between the most remote jets for the symmetric cut with $p_T > 20$ GeV for $\sqrt{s} = 7$ TeV (left) and $\sqrt{s} = 13$ TeV (right). The SPS contribution is shown by the dotted line while the DPS contribution by the dashed line. The relative contribution of DPS is shown in the extra lower panels.

We also find that another variable, introduced in the high transverse momenta analysis of four jets production discussed in Ref. [11], can be very interesting for

the examination of the DPS effects:

$$\Delta\varphi_{3j}^{min} \equiv min_{\substack{i,j,k\in\{1,2,3,4\}\\ i\neq j\neq k}} \left(|\varphi_i - \varphi_j| + |\varphi_j - \varphi_k|\right) . \tag{3.4}$$

As three out of four azimuthal angles are always entering in (3.4), configurations with one jet recoiling against the other three are necessarily characterised by lower values of $\Delta\varphi_{3j}^{min}$ with respect to the two-against-two topology; the minimum, in fact, will be obtained in the first case for i, j, k denoting the three jets in the same hemisphere, whereas no such a case is possible for the second configuration. Obviously, the first case would be allowed only by SPS in a collinear tree-level framework, whereas the second would be enhanced by DPS. In the k_T-factorization approach, this situation is smeared out by the presence of transverse momenta of the initial state partons. For our unintegrated parton distributions, the corresponding distributions are shown in Fig. 8. We do not see such obvious effects in the case of the k_T-factorization.

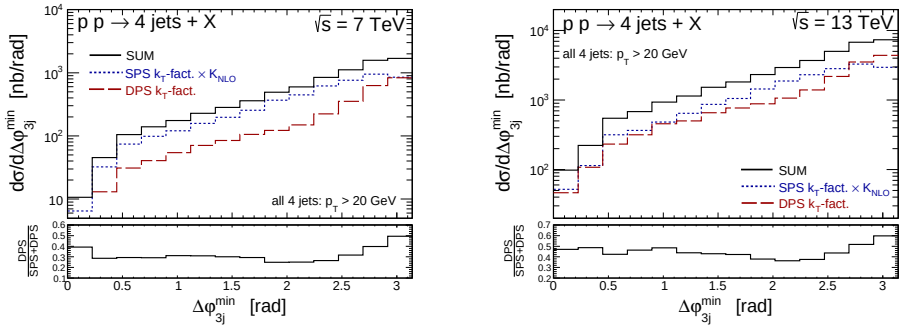

Figure 8: Distribution in $\Delta\varphi_{3j}^{min}$ angle for the symmetric cut with $p_T > 20$ GeV for $\sqrt{s} = 7$ TeV (left) and $\sqrt{s} = 13$ TeV (right). The SPS contribution is shown by the dotted line while the DPS contribution by the dashed line. The relative contribution of DPS is shown in the extra lower panels.

4 Conclusions

We have presented our recent results for four-jet production obtained for the first time within k_T-factorization approach. The calculation of the SPS contribution is a technical achievment. So far only production of the $c\bar{c}c\bar{c}$ final state (also of the 2 $\to$ 4 type) was discussed in the literature.

We have found that both collinear and the (k_T-)factorization approaches describe the data for hard central cuts, relevant for the ATLAS experiment, reasonably well when using the KMR TMDs. For the harder cuts we get both normalization and shape of the transverse momentum distributions. We nicely describe also CMS distribution for a special variable ΔS.

In this presentation we have discussed also how to look at the DPS effects and how to maximize their role in four jet production. We found that, for sufficiently small cuts on the transverse momenta, DPS effects are enhanced relative to the SPS contribution: when rapidities of jets are large, for large rapidity distances between the most remote jets, for small azimuthal angles between the two jets most remote

in rapidity and/or for large values of the $\Delta\varphi_{3j}^{min}$ variable. For more details we refer the interested reader to our regular article [4].

Acknowledgments

The work presented here was done in collaboration with Krzysztof Kutak, Mirko Serino and Andreas van Hameren. We are indebted to them for a friutfull collaboration. This work was partially supported by DEC-2014/15/B/ST2/02528.

References

[1] Z. Bern *et al.*, Phys. Rev. Lett. **109**, 042001 (2012) [arXiv:1112.3940 [hep-ph]].

[2] S. Badger, B. Biedermann, P. Uwer and V. Yundin, Phys. Lett. B **718**, 965 (2013) doi:10.1016/j.physletb.2012.11.029 [arXiv:1209.0098 [hep-ph]].

[3] K. Kutak, R. Maciula, M. Serino, A. Szczurek and A. van Hameren, JHEP **1604**, 175 (2016).

[4] K. Kutak, R. Maciula, M. Serino, A. Szczurek and A. van Hameren, arXiv:1605.08240 [hep-ph].

[5] R. Maciula and A. Szczurek, Phys. Lett. B **749**, 57 (2015) [arXiv:1503.08022 [hep-ph]].

[6] M. Diehl, D. Ostermeier and A. Schafer, JHEP **1203**, 089 (2012) [arXiv:1111.0910 [hep-ph]].

[7] M. Bury and A. van Hameren, Comput. Phys. Commun. **196**, 592 (2015).

[8] H. Jung, D. Treleani, M. Strikman and N. van Buuren, DESY-PROC-2016-01.

[9] S. Chatrchyan *et al.* [CMS Collaboration], Phys. Rev. D **89**, 092010 (2014).

[10] R. Maciula and A. Szczurek, Phys. Rev. D **90**, 014022 (2014) [arXiv:1403.2595 [hep-ph]].

[11] G. Aad *et al.* [ATLAS Collaboration], JHEP **1512**, 105 (2015) [arXiv:1509.07335 [hep-ex]].

Drell-Yan production at forward rapidities: a hybrid factorization approach

Wolfgang Schäfer[1], Antoni Szczurek[1,2]

[1]Institute of Nuclear Physics, Polish Academy of Sciences
Kraków, Poland
[2]University of Rzeszów, Rzeszów, Poland

August 9, 2017

Abstract

We discuss the Drell-Yan production of dileptons at high energies in the forward rapidity region of proton-proton collisions in a hybrid high-energy approach. This approach uses unintegrated gluon distributions in one proton and collinear quark/antiquark distributions in the second proton.

We compute various distributions for the case of low-mass dilepton production and compare to the LHCb and ATLAS experimental data on dilepton mass distributions. In distinction to dipole approaches, we include four Drell-Yan structure functions as well as cuts at the level of lepton kinematics. The impact of the interference structure functions is rather small for typical experimental cuts. We find that both side contributions ($gq/\bar{q}$ and $q/\bar{q}g$) have to be included even for the LHCb rapidity coverage which is in contradiction with what is usually done in the dipole approach. We present results for different unintegrated gluon distributions from the literature. Some of them include saturation effects, but we see no clear hints of saturation even at small M_{ll}.

1 Introduction

Drell-Yan production in the forward direction is dominated by the quark-gluon fusion, where especially at not too large invariant masses of the dilepton system the gluon density is probed at low values of the longitudinal momentum fraction x. One might

therefore probe a kinematic range where gluon saturation effects are potentially large. Consequently the forward Drell-Yan process has been discussed in the Color-Glass Condensate approach in [1]. Recently much attention has also been paid to appplications of the color dipole approach to the Drell-Yan process at the LHC (see e.g. [2, 3, 4, 5])

In this talk we instead present an alternative formulation in momentum space published recently in [6]. In particular, this approach includes all the four structure functions [7] of the Drell-Yan process and allows to put cuts on the momenta of individual leptons (e^+e^- or $\mu^+\mu^-$). This is important if one wants to compare to existing experimental data.

The mechansims considered are shown in the diagrams in Fig.1.

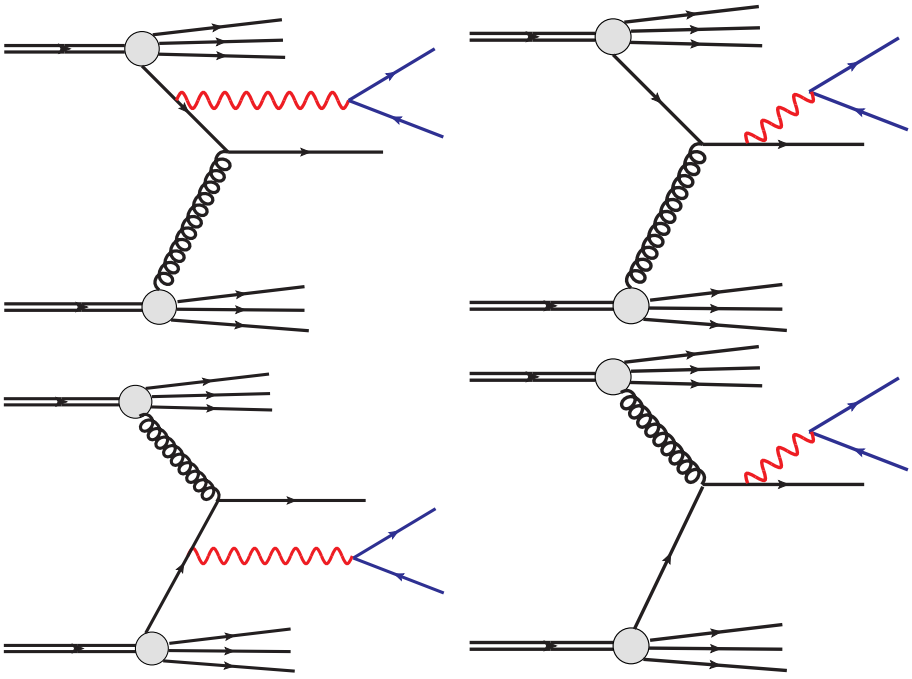

Figure 1: The diagrams relevant for forward and backward production of dilepton pairs.

2 Results

We start by defining the relevant kinematical variables. Below, $x_\pm$ will denote the longitudinal (lightcone-) momentum fractions of leptons, while $\mathbf{k}_\pm$ are their transverse momenta. The heavy virtual photon of mass M^2 then carries the longitudinal momentum fraction $x_F = x_+ + x_-$ and transverse momentum $\mathbf{q} = \mathbf{k}_+ + \mathbf{k}_-$. It is useful to introduce also the light-front relative transverse momentum of l^+ and l^-:

$$\mathbf{l} = \frac{x_+}{x_F}\mathbf{k}_- - \frac{x_-}{x_F}\mathbf{k}_+ \,. \tag{1}$$

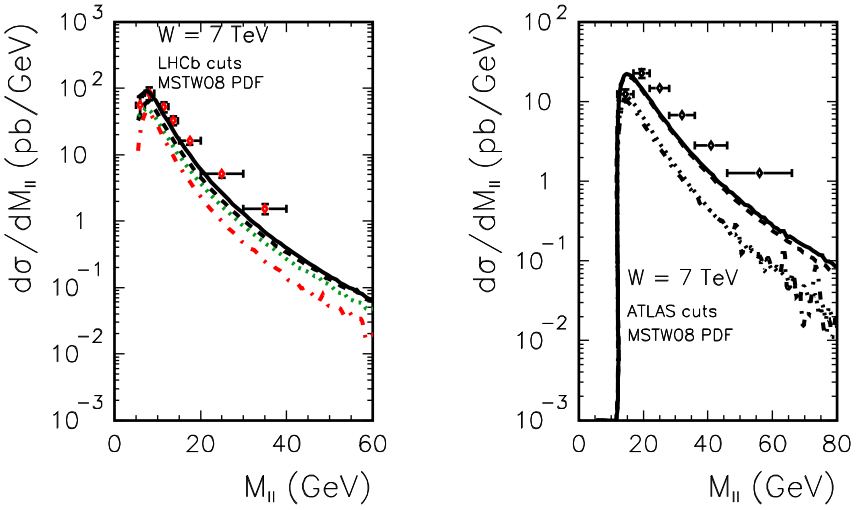

Figure 2: Left panel: Invariant mass distribution (only the dominant component) for the LHCb cuts: $2 < y_+, y_- < 4.5$, $k_{T+}, k_{T-} > 3$ GeV for different UGDFs: KMR (solid), Kutak-Stasto (dashed), AAMS (dotted) and GBW (dash-dotted). Right panel: the same for the ATLAS kinematics: -2.4 $< y_+, y_- < 2.4$, $k_{T+}, k_{T-} > 6$ GeV. Here both $gq/\bar{q}$ and $q/\bar{q}g$ contributions have been included.

Then, the inclusive cross section for lepton pair production can be written in the form:

$$\begin{aligned}\frac{d\sigma(pp \to l^+l^-X)}{dx_+dx_-d^2\mathbf{k}_+d^2\mathbf{k}_-} &= \frac{\alpha_{\rm em}}{(2\pi)^2M^2}\frac{x_F}{x_+x_-}\Big\{\Sigma_T(x_F,\mathbf{q},M^2)D_T\Big(\frac{x_+}{x_F}\Big) \\ &+ \Sigma_L(x_F,\mathbf{q},M^2)D_L\Big(\frac{x_+}{x_F}\Big) \\ &+ \Sigma_\Delta(x_F,\mathbf{q},M^2)D_\Delta\Big(\frac{x_+}{x_F}\Big)\Big(\frac{\mathbf{l}}{|\mathbf{l}|}\cdot\frac{\mathbf{q}}{|\mathbf{q}|}\Big) \\ &+ \Sigma_{\Delta\Delta}(x_F,\mathbf{q},M^2)D_{\Delta\Delta}\Big(\frac{x_+}{x_F}\Big)\Big(2\Big(\frac{\mathbf{l}}{|\mathbf{l}|}\cdot\frac{\mathbf{q}}{|\mathbf{q}|}\Big)^2-1\Big)\Big\}. \quad (2)\end{aligned}$$

The functions $\Sigma_i(x_F,\mathbf{q},M^2)$, $i = T, L, \Delta, \Delta\Delta$ are in a one-to-one correspondence with the four helicity structure functions [7] of inclusive lepton pair production in a Gottfried-Jackson frame. They contain all information of strong dynamics in the production of the virtual photon. The functions D_i and the momentum structures in brackets represent the density matrix of decay of the massive photon into l^+l^-. For explicit expressions, see [6].

Let us concentrate now on one of the partonic subprocesses, where a fast quark from one proton radiates a virtual photon while interacting with a small-x gluon of the other proton. (E.g. the top two diagrams in Fig. 1.) Naturally the large-x quark is described by the collinear quark distribution, while for the low-x gluon it is more appropriate to use the k_T-dependent unintegrated gluon distribution.

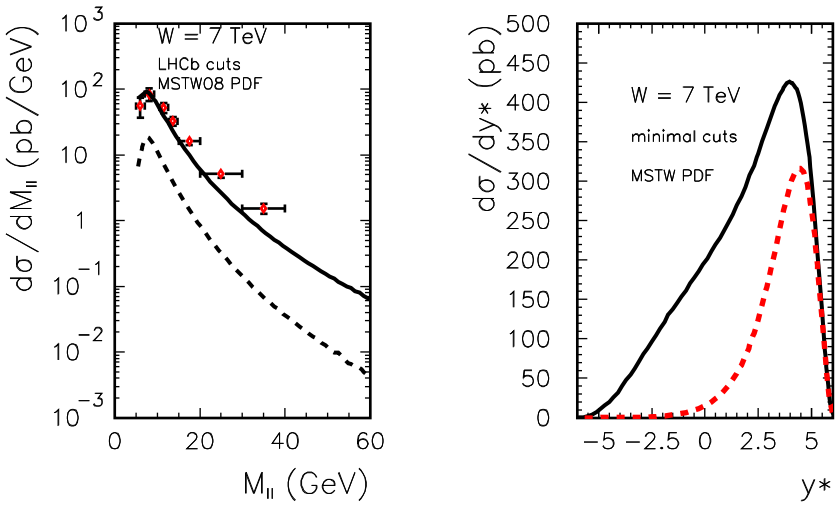

Figure 3: Left Panel: By the dashed line, we show the contributions of the second-side component for the LHCb kinematics: $2 < y_+, y_- < 4.5$, $k_{T+}, k_{T-} > 3$ GeV. KMR UGDF was used here. Right panel: Distribution in rapidity of the dileptons for $\sqrt{s} = 7$ TeV and $k_{T+}, k_{T-} > 3$ GeV for MSTW08 valence quark distributions and KMR UGDFs. The dashed line is the contribution from valence quarks only.

We can then write for the functions Σ_i an impact-factor representation typical of the $k_\perp$-factorization:

$$\begin{aligned}\Sigma_i(x_F, \mathbf{q}, M) &= \sum_f \frac{e_f^2 \alpha_{\rm em}}{2N_c} \int_{x_F}^1 dx_1 \left[q_f(x_1, \mu^2) + \bar{q}_f(x_1, \mu^2)\right] \\ &\times \int \frac{d^2\boldsymbol{\kappa}}{\pi \boldsymbol{\kappa}^4} \mathcal{F}(x_2, \boldsymbol{\kappa}^2) \alpha_S(\bar{q}^2) I_i\Big(\frac{x_F}{x_1}, \mathbf{q}, \boldsymbol{\kappa}\Big)\,. \end{aligned} \tag{3}$$

Here appears the unintegrated gluon distribution

$$\mathcal{F}(x_2, \boldsymbol{\kappa}^2) \propto \frac{\partial x_2 g(x_2, \boldsymbol{\kappa}^2)}{\partial \log(\boldsymbol{\kappa}^2)}\,. \tag{4}$$

The impact factors I_i can be found in [6].

Here an important comment on the longitudinal momentum fractions x_1, x_2 is in order. They must be obtained from the full l^+l^-q final state:

$$\begin{aligned} x_1 &= \sqrt{\frac{\mathbf{k}_+^2}{S}} e^{y_+} + \sqrt{\frac{\mathbf{k}_-^2}{S}} e^{y_-} + \sqrt{\frac{\mathbf{k}_q^2}{S}} e^{y_q}\,, \\ x_2 &= \sqrt{\frac{\mathbf{k}_+^2}{S}} e^{-y_+} + \sqrt{\frac{\mathbf{k}_-^2}{S}} e^{-y_-} + \sqrt{\frac{\mathbf{k}_q^2}{S}} e^{-y_q}\,. \end{aligned} \tag{5}$$

Neglecting the contribution from the final state (anti-)quark leads to a systematic underestimation of x-values, which may artificially enhance saturation effects.

In Fig. 2 we compare our results to recent experimental data. In the left panel we compare our results for the dilepton invariant mass distribution to the data from the LHCb collaboration [8], which cover the forward rapidity region. Here a reasonable description of data can be obtained by an unintegrated gluon distribution constructed by the KMR prescription. Other gluon distributions which include gluon saturation effects do not lead to such a good agreement. In the right panel, we compare our results to the ATLAS data [9]. These data were obtained in the central rapidity region. This kinematical domain is strictly speaking beyond the region of applicability of our approach. The asymmetrical treatment of collinear quarks and k_T-dependent gluons is not warranted here. And indeed, we do not describe the ATLAS data well, especially at large invariant masses.

The results shown in Fig. 3 were obtained in the LHCb kinematics. In the left panel we show by the dashed line the contribution from dileptons emitted from the "other side" proton. As we observe, such a spillover of dileptons emitted into the forward region of "the other" proton is not negligible. It seems to have been generally neglected in dipole model calculations. In the right panel we show the rapidity distribution of the virtual photon. By the red dashed line we show the contribution from valence quarks of the "forward" proton only. We see that within the rapidity coverage of LHCb sea quarks are important.

3 Summary

In this talk at the Low-x meeting, we have presented the main results from our recent paper [6] on the Drell-Yan production of dileptons in the forward rapidity region in a hybrid factorization approach. Here the large-x parton participating in the hard process is described by a collinear parton distribution, while for the low-x parton an unintegrated parton distribution is taken.

We have compared the results of our calculations to recent experimental data for low-mass dilepton production from the LHCb and ATLAS experiments.

Going beyond on previous work in the literature, we have found that emissions from both protons have to be included even for the LHCb configuration.

We find that LHCb data do not require gluon saturation effects at small M_{ll}.

Acknowledgements:
The work reported here was supported by the Polish National Science Centre grant DEC-2014/15/B/ST2/02528.

References

[1] F. Gelis and J. Jalilian-Marian, Phys. Rev. D **66**, 094014 (2002) [hep-ph/0208141]; Phys. Rev. D **76**, 074015 (2007) [hep-ph/0609066].

[2] M. B. G. Ducati, M. T. Griep and M. V. T. Machado, Phys. Rev. D **89**, no. 3, 034022 (2014) [arXiv:1307.6882 [hep-ph]].

[3] K. Golec-Biernat, E. Lewandowska and A. M. Stasto, Phys. Rev. D **82**, 094010 (2010) [arXiv:1008.2652 [hep-ph]].

[4] E. Basso, V. P. Goncalves, J. Nemchik, R. Pasechnik and M. Sumbera, Phys. Rev. D **93**, 034023 (2016) [arXiv:1510.00650 [hep-ph]].

[5] L. Motyka, M. Sadzikowski and T. Stebel, JHEP **1505**, 087 (2015) [arXiv:1412.4675 [hep-ph]].

[6] W. Schäfer and A. Szczurek, Phys. Rev. D **93** (2016) no.7, 074014 doi:10.1103/PhysRevD.93.074014 [arXiv:1602.06740 [hep-ph]].

[7] R. J. Oakes, Nuovo Cimento A **44**, 440 (1966); C. S. Lam and W. K. Tung, Phys. Rev. D **18**, 2447 (1978).

[8] [The LHCb collaboration], "Inclusive low mass Drell-Yan production in the forward region at sqrt(s)=7 TeV ," LHCb-CONF-2012-013; Conference report prepared for XX International Workshop on Deep-Inelastic Scattering and Related Subjects, 26-30, March 2012, Bonn, Germany.

[9] G. Aad *et al.* [ATLAS Collaboration], JHEP **1406**, 112 (2014) [arXiv:1404.1212 [hep-ex]].

Measurements of charged-particle distributions with the ATLAS detector

Valentina Maria Martina CAIRO[12], on behalf of the ATLAS Collaboration

[1]University of Calabria, Arcavacata di Rende, Italy
[2]CERN, Meyrin, Switzerland

August 9, 2017

Abstract

Inclusive charged-particle measurements probe the low-energy region of the non-perturbative quantum chromodynamics. The ATLAS collaboration has recently measured the charged-particle multiplicity and its dependence on transverse momentum and pseudorapidity in special data sets with low LHC beam currents, recorded at centre-of-mass energies of 8 TeV and 13 TeV. The measurements at 8 TeV cover a wide spectrum using charged-particle selections with minimum transverse momentum of both 100 MeV and 500 MeV and in various phase space regions of low and high charged-particle multiplicities, some of which are studied for the first time by ATLAS. The measurements at 13 TeV also present detailed studies with a minimum transverse momentum of both 100 MeV and 500 MeV. The measurements are compared with predictions of various tuned Monte Carlo generators and are found to provide strong constraints on these. None of the Monte Carlo generators with their respective tunes are able to reproduce all the features of the data.

1 Introduction

The measurements of inclusive charged-particle spectra provide insight into the low energy non-perturbative region of quantum chromodynamics (QCD). A description of low-energy processes within a perturbative framework is not possible in this regime, thus charged-particle interactions are typically described by QCD-inspired models implemented in Monte Carlo (MC) event generators. Measurements are used to constrain the free parameters of these models. Furthermore, soft processes, arising from pile-up at high luminosity, which leads to more than one interaction per beam crossing, may also affect the topologies of events triggered by a specific hard-scattering interaction. An understanding of soft QCD processes is therefore important both in its own right and as a means of reducing systematic uncertainties in measurements of high transverse momentum phenomena. Charged-particle distributions have been measured previously in hadronic collisions at various centre-of-mass energies, see Refs. [1, 2, 3, 4, 5, 6, 7] and references therein. This note describes the most recent charged-particle spectra measured by using data collected with the ATLAS detector [8] at the centre-of-mass energy of 13 TeV [9, 10], with a particular emphasis on the tracking-related aspects. Some highlights from the high charged-particle multiplicity regions studied at the 8 TeV [11] centre-of-mass energy are also given. The average primary charged-particle densities at central pseudorapidity are compared to measurements at lower centre-of-mass energies.

2 Methodology

The methodology used in the 8 and 13 TeV analyses is similar to that used at lower centre-of-mass energies in ATLAS [1]. The events collected correspond to minimum-bias datasets based on inelastic pp interactions. The term *minimum bias* is taken to refer to trigger and event selections which are as unrestrictive as possible for the pp-induced final state. The data were recorded during special fills with low beam currents and reduced focusing to give a mean number of interactions per bunch crossing below 0.005. This procedure guarantees that the contribution from pile-up in these analyses is negligible. The measurements use tracks from primary charged-particles, corrected for detector effects to the particle level, and presented as inclusive distributions in a fiducial phase space region. Primary charged-particles are defined as charged-particles with a mean lifetime $\tau > 300$ ps, either directly produced in pp interactions or from subsequent decays of directly produced particles with $\tau < 30$ ps. Particles produced from decays of particles with $\tau > 30$ ps, called secondary particles, are excluded. This definition differs from earlier analyses in which charged-particles with a mean lifetime $30 < \tau < 300$ ps were included. Most of these are charged strange baryons and they have been removed due to the low reconstruction efficiency of their decay products and to large variations in the predicted rates which would lead to a significant model dependence of the results presented here.

The following distributions are presented for data and compared to MC predictions:

$$\frac{1}{N_{\rm ev}} \cdot \frac{{\rm d}N_{\rm ch}}{{\rm d}\eta},\ \frac{1}{N_{\rm ev}} \cdot \frac{1}{2\pi p_{\rm T}} \cdot \frac{{\rm d}^2 N_{\rm ch}}{{\rm d}\eta {\rm d}p_{\rm T}},\ \frac{1}{N_{\rm ev}} \cdot \frac{{\rm d}N_{\rm ev}}{{\rm d}n_{\rm ch}},\ \langle p_{\rm T} \rangle \text{ vs } n_{\rm ch},$$

where $p_{\rm T}$ is the track momentum component that is transverse to the beam direction[1], η is the track pseudorapidity, $n_{\rm ch}$ is the number of primary charged-particles in the bin relevant to the measurement, $N_{\rm ev}$ is the number of selected minimum bias events, $N_{\rm ch}$ is the total number of primary charged-particles in the kinematic acceptance and $\langle p_{\rm T} \rangle$ is the average $p_{\rm T}$ for a given number of charged-particles[2]. In order to make a more complete study of particle properties in minimum-bias events, results are given for different multiplicity and kinematic selections (referred to as *phase spaces*). In the most inclusive phase spaces, a minimum $n_{\rm ch} \geq 2$ or 1 is required and the primary charged-particle must have $\eta < 2.5$ and $p_{\rm T} > 100$ MeV (referred to as *extended phase space*) or 500 MeV (referred to as *nominal phase space*) , respectively. In the 13 TeV case, the spectra are also measured in a phase space that is common to the ATLAS, CMS [12] and ALICE [13] detectors in order to ease comparison between experiments. For this purpose an additional requirement of $\eta < 0.8$ (referred to as *reduced phase space*) is made for all primary charged-particles with $p_{\rm T} > 500$ MeV and the results can be found in [9].

The PYTHIA 8 [14] (used as a baseline), EPOS [15] and QGSJET-II [16] MC models of inclusive hadron–hadron interactions were used to generate event samples and compare their distributions to data. Different parameter settings in the models are used in the simulation to reproduce existing experimental data and are referred to as *tunes*. For PYTHIA 8, the A2 [17] tune is based on the MSTW2008LO PDF [18] while the Monash [19] underlying-event tune uses the NNPDF2.3LO PDF [20] and incorporates updated fragmentation parameters, as well as SPS and Tevatron data to constrain the scaling with energy. For EPOS, the LHC [21] tune is used, while for QGSJET-II the default settings of the generator are applied. Detector effects are simulated using the GEANT4-based [22] ATLAS simulation framework [23]. The simulation also takes into account inactive and inefficient regions of the ATLAS detector. The resulting datasets were used to derive corrections for detector effects, evaluate systematic uncertainties and compare to the data corrected to particle level.

3 Charged-particle measurements at 13 TeV

3.1 Event Selection

Collision events were selected using a trigger which required one or more minimum-bias trigger scintillators counters (MBTS) above threshold on either side of the

[1]The ATLAS reference system is a Cartesian right-handed coordinate system, with the nominal collision point at the origin. The anti-clockwise beam direction defines the positive z-axis, while the positive x-axis is defined as pointing from the collision point to the center of the LHC ring and the positive y-axis points upwards. The azimuth angle ϕ is measured around the beam axis, and the polar angle θ is measured with respect to the z-axis. The pseudorapidity is defined as $\eta = -\ln\tan(\theta/2)$.

[2]The factor $2\pi p_{\rm T}$ in the $p_{\rm T}$ spectrum comes from the Lorentz invariant definition of the cross section in terms of d^3p. Furthermore, the mass-less approximation is used: $y \approx \eta$.

detector. Each event is required to contain a primary vertex, reconstructed from at least two tracks with a minimum p_{T} of 100 MeV, as described in [24]. A veto is applied on additional primary vertices arising from split vertices or secondary interactions. A special configuration of the track reconstruction algorithms was used for this analysis to reconstruct low-momentum tracks with good efficiency and purity. Similar configurations were already used in Run 1, but a more robust and efficient low-p_{T} track reconstruction program is available in Run 2 thanks to the installation of an insertable B-layer, IBL [25], which provides a fourth measurement point in the pixel detector. In the *nominal phase space*, events are required to contain at least one selected track, passing the following criteria: $p_{\mathrm{T}} > 500$ MeV and $|\eta| < 2.5$; at least one pixel hit and at least six SCT hits (two, four or six SCT hits for $p_{\mathrm{T}} < 300$ MeV, $p_{\mathrm{T}} < 400$ MeV or $p_{\mathrm{T}} > 400$ MeV, respectively, in the case of the *extended phase space*), with the additional requirement of an innermost-pixel-layer hit if expected[3] (if a hit in the innermost layer is not expected, the next-to-innermost hit is required if expected); $|d_0^{BL}| < 1.5$ mm, where the transverse impact parameter, d_0^{BL}, is calculated with respect to the measured beam line position; and $|z_0^{BL} \cdot sin\theta| < 1.5$ mm, where $z_0^{BL}$is the difference between the longitudinal position of the track along the beam line at the point where d_0^{BL} is measured and the longitudinal position of the primary vertex, and θ is the polar angle of the track. Finally, in order to remove tracks with mismeasured p_{T} due to interactions with the material or other effects, the track-fit χ^2 probability is required to be greater than 0.01 for tracks with $p_{\mathrm{T}} < 10$ GeV.

Approximately 9 million events are selected, containing a total of ~ 100 million reconstructed tracks. While the overall number of particles in the kinematic acceptance of the *extended phase space* is nearly double that in the *nominal phase space*, the measurements are more difficult for $p_{\mathrm{T}} < 500$ MeV, due to multiple scattering and imprecise knowledge of the material in the detector. These systematic uncertainties at low p_{T} need therefore to be carefully evaluated. The performance of the Inner Detector (ID) track reconstruction in the 13 TeV data and its simulation is described in Ref. [26]. Overall, good agreement between data and simulation is observed.

3.2 Analysis strategy

The main steps of the analysis are related to the trigger, vertex and track reconstruction efficiencies, which need to be evaluated together with their uncertainties. The background contributions to the tracks from primary particles, which include fake tracks (those formed by a random combination of hits), strange baryons and secondary particles, need to be estimated as well. Observables of interest can be evaluated and, by means of an unfolding procedure, can be corrected to account for detector effects. The details can be found in Refs. [9, 10], while, in the next section, a few insights will be given on the track reconstruction efficiency by highlighting the importance of a precise evaluation of the amount of material in the ATLAS ID, which represents the main source of systematic uncertainty for this analysis.

[3] A hit is expected if the extrapolated track crosses a known active region of a pixel module.

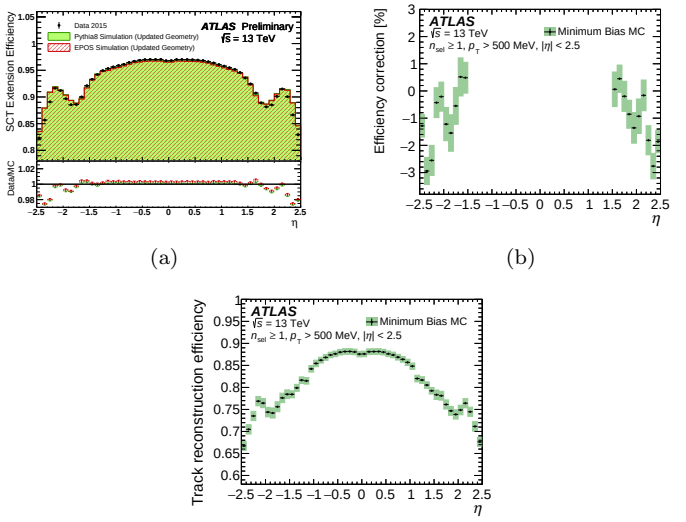

Figure 1: (a) SCT extension efficiency as a function of pseudorapidity η of the pixel track segments in a comparison between data, PYTHIA 8 and EPOS, from Ref. [27]. (b) Data-driven correction to the track reconstruction efficiency as a function of pseudorapidity, η, from Ref. [9]. (c) The track reconstruction efficiency after this correction as a function of η, from Ref. [9]. n_{sel} is defined as the number of tracks passing all of the track selection requirements.

3.3 Track reconstruction efficiency

The analysis is a track-based analysis and the evaluation of the track reconstruction efficiency and of the related systematics is crucial. The dominant uncertainty in the track reconstruction efficiency arises from imprecise knowledge of the amount of material in the ID. The primary track reconstruction efficiency $\varepsilon_{\mathrm{trk}}$ is determined from simulation. The efficiency is parameterised in two-dimensional bins of p_{T} and η, and is defined as:

$$\varepsilon_{\mathrm{trk}}(p_{\mathrm{T}}, \eta) = \frac{N_{\mathrm{rec}}^{\mathrm{matched}}(p_{\mathrm{T}}, \eta)}{N_{\mathrm{gen}}(p_{\mathrm{T}}, \eta)}, \tag{1}$$

where p_{T} and η are defined at generator level, $N_{\mathrm{rec}}^{\mathrm{matched}}(p_{\mathrm{T}}, \eta)$ is the number of reconstructed tracks matched to a generated primary charged-particle and $N_{\mathrm{gen}}(p_{\mathrm{T}}, \eta)$ is the number of generated primary charged-particles in the kinematic region of interest. A track is matched to a generated particle if the weighted fraction of track hits originating from that particle exceeds 50%. In the analysis performed in the *nominal phase space*, a data-driven correction to the efficiency was applied in order to account for material effects in the $|\eta| > 1.5$ region. The track reconstruction efficiency depends on the amount of material in the detector, due to particle interactions that lead to efficiency losses. The relatively large amount of material

between the pixel and SCT detectors in the region $|\eta| > 1.5$ has changed between Run 1 and Run 2 due to the replacement of some pixel services, which are difficult to simulate accurately. The track reconstruction efficiency in this region is corrected using a method, referred to as SCT extension efficiency [27], that compares data and simulation for the efficiency to extend a track reconstructed in the pixel detector (referred to as pixel track segment) into the SCT. Differences in SCT extension efficiency are quite sensitive to differences in the amount of material in this region, as can be seen in Figure 1(a). The correction, together with the systematic uncertainty, coming predominantly from the uncertainty of the particle composition in the simulation used to make the measurement, is shown in Figure 1(b). The uncertainty in the track reconstruction efficiency resulting from this correction is $\pm$0.4% in the region $|\eta| > 1.5$. The resulting reconstruction efficiency as a function of η integrated over p_{T} is shown in Figure 1(c). The track reconstruction efficiency is lower in the region $|\eta| > 1$ due to particles passing through more material in that region. The slight increase in efficiency at $|\eta| \sim 2.2$ is due to particles passing through an increasing number of layers in the end-cap Pixel regions of the ID. The data-driven correction allows for a large reduction of the systematic uncertainty in the measurement with respect to previous studies but it cannot be applied in the *reduced phase space* due to the large uncertainties of this method for low-momentum tracks. In this case, the total uncertainty on the track reconstruction efficiency due to the amount of material is calculated as the linear sum of the contributions of 5% additional material in the entire ID, 10% additional material in the IBL and 50% additional material in the pixel services region for $|\eta| > 1.5$, as described in detail in [28].

The SCT extension efficiency only probes the material between the pixel and SCT detectors in the region $|\eta| > 1.5$, but a good understanding of the material in the other regions of the ID is needed for good description of the track reconstruction efficiency. The material in the ID was studied extensively during Run 1 [29, 30], where the amount of material was known to $\pm$5%. This gives rise to a systematic uncertainty in the track reconstruction efficiency of $\pm$0.6% ($\pm$1.2%) in the most central (forward) region. Between Run 1 and Run 2, the IBL was installed, and its simulation therefore can only be optimised with the Run 2 data. Two data-driven methods are used [27]: a study of secondary vertices from photon conversions and a study of secondary vertices from hadronic interactions, where the radial position of the vertex and the invariant mass of the outgoing particles are measured. Comparisons between data and simulation indicate that the material in the IBL is constrained to within $\pm$10%. This leads to an uncertainty in the track reconstruction efficiency of $\pm$0.1% ($\pm$0.2%) in the central (forward) region. This uncertainty is added linearly to the uncertainty from constraints from Run 1, to cover the possibility of missing material in the simulation in both cases. The resulting uncertainty is added in quadrature to the uncertainty from the data-driven correction.

The total uncertainty on the track reconstruction efficiency due to the imperfect knowledge of the detector material is $\pm$0.7% in the most central region and it grows to $\pm$1.5% in the most forward region. There is a small difference in efficiency, between data and simulation, due to the detector hit requirements described in Section

3.1. This difference is assigned as a further systematic uncertainty, amounting to $\pm$0.5% for $p_{\mathrm{T}} < 10$ GeV and $\pm$0.7% for $p_{\mathrm{T}} > 10$ GeV. The total uncertainty due to the track reconstruction efficiency determination, shown in Figure 1(c), is obtained by adding all effects in quadrature and is dominated by the uncertainty from the material description.

3.4 Corrections and final results

To produce unfolded distributions at particle level, all distributions are first corrected for the loss of events due to the trigger and vertex requirements. The η and p_{T} distributions of selected tracks are then corrected using a track-by-track weight, as described in Refs. [9, 10, 11]. No additional corrections are needed for the η distribution because the resolution is smaller than the bin width. For the p_{T} distribution, an iterative Bayesian unfolding [31] is applied to correct the measured track p_{T} distribution to that for primary particles. After applying the event weight, the Bayesian unfolding is also applied to the multiplicity distribution. The total number of events, N_{ev}, used to normalise the distributions, is defined as the integral of the n_{ch} distribution, after all corrections are applied. The dependence of $\langle p_{\mathrm{T}} \rangle$ on n_{ch} is obtained by first separately correcting the total number of tracks and $\sum_i p_{\mathrm{T}}(i)$ (summing over the p_{T} of all tracks and all events), both versus the number of primary charged-particles. After applying the correction to all events using the event and track weights, both distributions are unfolded separately. The bin-by-bin ratio of the two unfolded distributions gives the dependence of $\langle p_{\mathrm{T}} \rangle$ on n_{ch}.

The corrected distributions for primary charged-particles in events with $n_{\mathrm{ch}} = 1$ in the kinematic range of the *nominal phase space* are shown in Figure 2, while, for the *extended phase space*, they can be seen in Figure 3.

Figures 2(a) and 3(a) show the multiplicity of charged-particles as a function of η. In the *nominal phase space*, the mean particle density is roughly constant at 2.9 for $|\eta| < 1.0$ and decreases at higher values of $|\eta|$. EPOS describes the data well for $|\eta| < 1.0$, and predicts a slightly larger multiplicity at large $|\eta|$ values. QGSJET-II and PYTHIA 8-Monash predict multiplicities that are too large by approximately 15% and 5% respectively. PYTHIA 8-A2 predicts a multiplicity that is 3% too low in the central region, but describes the data well in the forward region. The total systematic uncertainty, dominated by the uncertainty on the track reconstruction efficiency, is below 1.5% in the entire η range. When moving to lower track-p_{T}, the situation changes and PYTHIA 8-Monash, EPOS and QGSJET-II give a good description for $|\eta| < 1.5$. The prediction from PYTHIA 8-A2 has the same shape as the predictions from the other generators, but lies below the data. It can be immediately noticed that much bigger systematic uncertainties affect the distribution in the high η region in the *extended phase space* (up to $\sim$ 7% with respect to $\sim$ 1.5% in the *nominal phase space*). They mainly come from the uncertainty in the amount of material in the ID, which was differently treated in the two phase spaces, as described above.

Figures 2(b) and 3(b) show the charged-particle transverse momentum distributions. EPOS describes the data well for $p_{\mathrm{T}} > 300$ MeV. The PYTHIA 8 tunes describe the data reasonably well, but they are below the data in the low-p_{T} region.

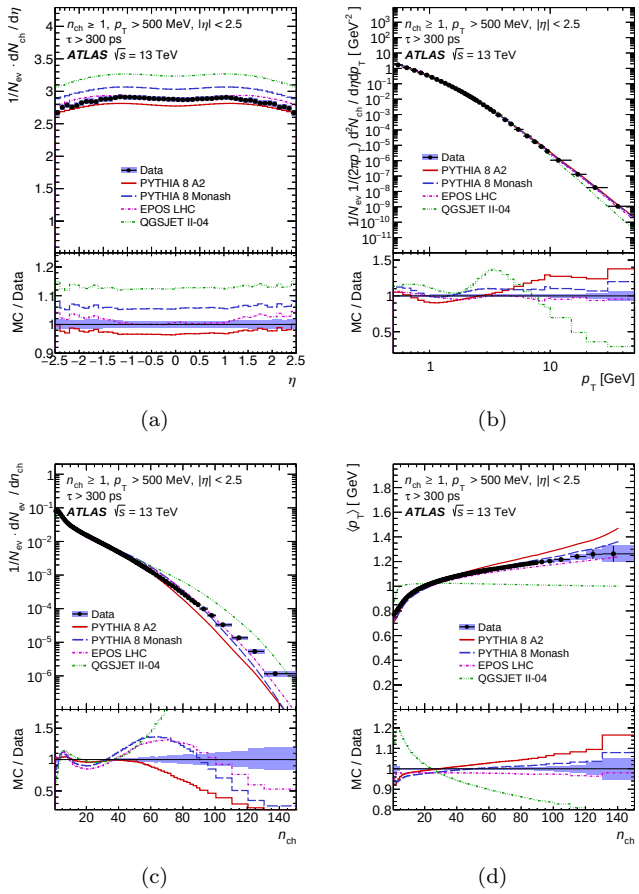

Figure 2: 13 TeV data, from Ref. [9]: Primary charged-particle multiplicities as a function of (a) pseudorapidity η and (b) transverse momentum p_{T}, (c) the primary charged-particle multiplicity n_{ch} and (d) the mean transverse momentum $\langle p_{\mathrm{T}} \rangle$ versus n_{ch} for events with at least one primary charged-particles with $p_{\mathrm{T}} > 500$ MeV, with $|\eta| < 2.5$, and with a lifetime $\tau > 300$ ps.

QGSJET-II gives a poor prediction over the entire spectrum, overshooting the data in the low-p_{T} region.

Figures 2(c) and 3(c) show the charged-particle multiplicity. PYTHIA 8-A2 describes the data reasonably well in the low-n_{ch} region, but predicts too few events at larger n_{ch} values. PYTHIA 8-Monash, EPOS and QGSJET-II describe the data reasonably well in the low-n_{ch} region but predict too many events in the mid-n_{ch} region, with PYTHIA 8-Monash and EPOS predicting too few events in the high-n_{ch} region while QGSJET-II, which implements a model without colour-reconnection, describes the data poorly in this case also.

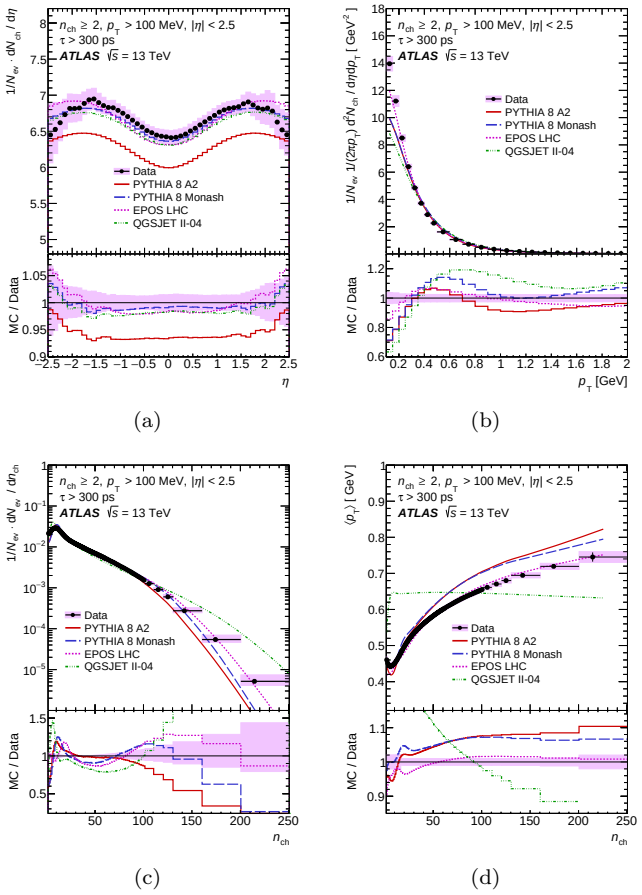

Figure 3: 13 TeV data, from Ref. [10]: Primary charged-particle multiplicities as a function of (a) pseudorapidity η and (b) transverse momentum p_{T}, (c) the primary charged-particle multiplicity n_{ch} and (d) the mean transverse momentum $\langle p_{\mathrm{T}} \rangle$ versus n_{ch} for events with at least two primary charged-particles with $p_{\mathrm{T}} > 100$ MeV, with $|\eta| < 2.5$, and with a lifetime $\tau > 300$ ps.

Figures 2(d) and 3(d) show how the mean transverse momentum, $\langle p_{\mathrm{T}} \rangle$, rises versus the charged-particle multiplicity. This rise is expected because of colour coherence effects in dense parton environments and is modelled by a colour reconnection mechanism in PYTHIA 8 or by the hydrodynamical evolution model used in EPOS. EPOS describes the data better than PYTHIA 8, which predicts a steeper rise of $\langle p_{\mathrm{T}} \rangle$ with n_{ch} than the data. If the high-n_{ch} region is assumed to be dominated by events with a large number of parton interactions within the same pp collision (MPI), without colour coherence effects, the $\langle p_{\mathrm{T}} \rangle$ should be independent of n_{ch}, as predicted by QGSJET-II.

4 Highlights from 8 TeV measurements

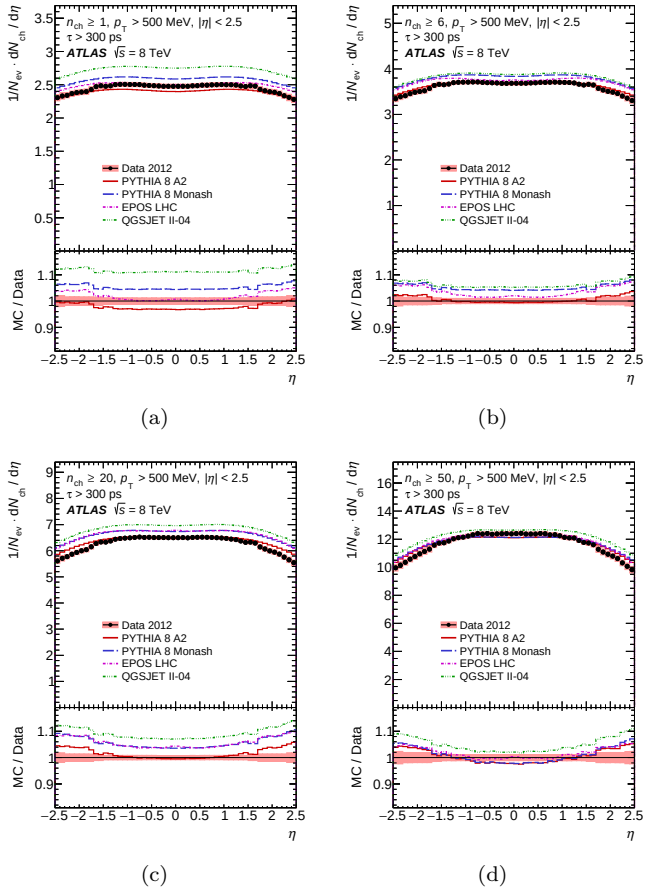

Figure 4: 8 TeV data, from Ref. [11]: Primary charged-particle multiplicities as a function of pseudorapidity η for events with at least (a) 1, (b) 6, (c) 20 or (d) 50 primary charged-particles with $p_{\mathrm{T}} > 500$ MeV, with $|\eta| < 2.5$, and with a lifetime $\tau > 300$ ps.

In the context of the 8 TeV analysis, high multiplicity phase spaces with $n_{\mathrm{ch}} \geq 20$ and 50 were studied for the first time. Figure 4 shows the multiplicity of charged-particles as a function of η for different multiplicity phase spaces with $n_{\mathrm{ch}} \geq 1$, 6, 20, 50. When requiring $n_{\mathrm{ch}} \geq 1$, EPOS gives a good description of the data for $|\eta| < 1.5$, while at higher $|\eta|$, PYTHIA 8-A2 describes the data better. For $n_{\mathrm{ch}} \geq 6$ or 20, the generator which describes data best is PYTHIA 8-A2. In the $n_{\mathrm{ch}} \geq 50$ case, PYTHIA and EPOS give similar descriptions for $|\eta| > 1.5$ and overestimate the data, while for $|\eta| < 1.5$ the best description is given by EPOS.

The spectra for the other *phase spaces* studied at $\sqrt{s} = 8$ TeV can be found in [11].

5 Charged-particle measurements at different $\sqrt{s}$

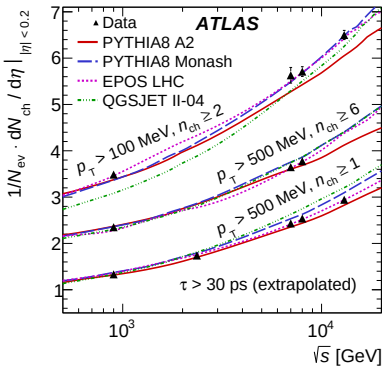

Figure 5: The average primary charged-particle multiplicity in pp interactions per unit of pseudorapidity η for $|\eta| < 0.2$ as a function of the centre-of-mass energy $\sqrt{s}$, from Ref. [10]. The results at 8 and 13 TeV have been extrapolated to include charged strange baryons in order to compare the values with previous studies.

Figure 5 shows the mean number of primary charged-particles in the central region of the detector as a function of $\sqrt{s}$. It is obtained by averaging over $|\eta| < 0.2$ and by correcting the 8 and 13 TeV data for the contribution from strange baryons in order to compare the results with lower centre-of-mass energies at which these particles were included. The mean number of primary charged-particles increases by a factor of 2.2 when $\sqrt{s}$ increases by a factor of about 14 from 0.9 TeV to 13 TeV. EPOS describes the dependence on $\sqrt{s}$ very well in several phase spaces, while PYTHIA 8-A2 and PYTHIA 8-Monash give a reasonable description, respectively for $p_{\mathrm{T}} >$ 500 MeV and $p_{\mathrm{T}} > 100$ MeV. QGSJET-II predicts a steeper rise in multiplicity with $\sqrt{s}$ than that shown by the data.

6 Conclusions

Primary charged-particle multiplicity measurements with the ATLAS detector using proton-proton collisions delivered by the LHC at the centre-of-mass energy of 13 TeV are presented, with a particular emphasis on the tracking-related aspects. Some highlights from the high charged-particle multiplicity regions studied at the 8 TeV centre-of-mass energy are also given. The results show clear differences between MC models and the measured distributions. Among the models considered, EPOS

reproduces best the data, PYTHIA 8-A2 and PYTHIA 8-Monash give reasonable descriptions of the data and QGSJET-II fails to describe most of the features of the data.

References

[1] ATLAS Collaboration, *Charged-particle multiplicities in pp interactions measured with the ATLAS detector at the LHC* (New J. Phys. 13, 053033 (2011). doi:10.1088/1367-2630/13/5/053033. arXiv:1012.5104 [hep-ex])

[2] CMS Collaboration, *Charged particle multiplicities in pp interactions at $\sqrt{s}$ = 0.9, 2.36 ,and 7 TeV* . (JHEP 1101, 079 (2011). doi:10.1007/JHEP01(2011)079. arXiv:1011.5531 [hep-ex])

[3] CMS Collaboration, *Transverse momentum and pseudorapidity distributions of charged hadrons in pp collisions at $\sqrt{s}$ = 7 TeV* (Phys. Rev. Lett. 105 (2010) 022002, arXiv:1005.3299 [hep-ex])

[4] CMS Collaboration, Transverse momentum and pseudorapidity distributions of charged hadrons in pp collisions at $\sqrt{s}$ = 0.9 and 2.36 TeV (JHEP 1002 (2010) 041, arXiv:1002.0621 [hep-ex])

[5] ALICE Collaboration, K. Aamodt et al., *Charged-particle multiplicity measured in proton?proton collisions at $\sqrt{s}$= 7 TeV with ALICE at LHC.* (Eur. Phys. J. C 68, 345?354 (2010). doi:10.1140/epjc/s10052-010-1350-2. arXiv:1004.3514 [hep-ex])

[6] CDF Collaboration, *T. Aaltonen et al., Measurement of Particle Production and Inclusive Differential Cross Sections in $p\bar{p}$ Collisions at $\sqrt{s}$=1.96 TeV* (Phys. Rev. D 79 (2009) 112005, arXiv:0904.1098 [hep-ex])

[7] CMS Collaboration, *Pseudorapidity distribution of charged hadrons in proton-proton collisions at $\sqrt{s}$ = 13 TeV* (Phys. Lett. B 751 (2015) 143, arXiv:1507.05915 [hep-ex])

[8] ATLAS Collaboration, *The ATLAS Experiment at the CERN Large Hadron Collider* (JINST 3 (2008) S08003)

[9] ATLAS Collaboration, *Charged-particle distributions in $\sqrt{s}$ = 13 TeV pp interactions measured with the ATLAS detector at the LHC* (Phys. Lett. B 758, 67?88 (2016). doi:10.1016/j.physletb.2016.04.050. arXiv:1602.01633)

[10] ATLAS Collaboration, *Charged-particle distributions at low transverse momentum in $\sqrt{s}$ = 13 TeV pp interactions measured with the ATLAS detector at the LHC* (Eur. Phys. J. C (2016) 76: 502. doi:10.1140/epjc/s10052-016-4335-y)

[11] ATLAS Collaboration, *Charged-particle distributions in pp interactions at $\sqrt{s}$ = 8 TeV measured with the ATLAS detector at the LHC* (arXiv:1603.02439 [hep-ex] (2016))

[12] CMS Collaboration, *The CMS experiment at the CERN LHC*, (JINST 3 (2008) S08004)

[13] ALICE Collaboration, *The ALICE experiment at the CERN LHC* (JINST 3 (2008) S08002)

[14] T. Sjöstrand, S. Mrenna and P. Z. Skands, *A Brief Introduction to PYTHIA 8.1* (Comput. Phys. Commun. 178 (2008) 852, arXiv:0710.3820 [hep-ph])

[15] S. Porteboeuf, T. Pierog and K. Werner, *Producing Hard Processes Regarding the Complete Event: The EPOS Event Generator* ((2010), arXiv:1006.2967 [hep-ph])

[16] S. Ostapchenko, *Monte Carlo treatment of hadronic interactions in enhanced Pomeron scheme: QGSJET-II model* (Phys. Rev. D 83 (2011) 014018, arXiv:1010.1869 [hep-ph])

[17] ATLAS Collaboration, Further ATLAS tunes of Pythia 6 and Pythia 8. ATL-PHYS-PUB-2011-014 (2011). http://cds.cern.ch/record/1400677

[18] A.D. Martin, W.J. Stirling, R.S. Thorne, G. Watt, Parton distributions for the LHC. Eur. Phys. J. C 63, 189 (2009). doi:10.1140/epjc/s10052-009-1072-5. arXiv:0901.0002 [hep-ph]ADSCrossRef

[19] P. Skands, S. Carrazza, J. Rojo, *Tuning PYTHIA 8.1: the Monash 2013 Tune* (Eur. Phys. J. C 74, 3024 (2014). doi:10.1140/epjc/s10052-014-3024-y. arXiv:1404.5630 [hep-ph])

[20] NNPDF Collaboration, R.D. Ball et al., *Parton distributions with LHC data* (Nucl. Phys. B 867, 244 (2013). doi:10.1016/j.nuclphysb.2012.10.003. arXiv:1207.1303 [hep-ph])

[21] T. Pierog, Iu. Karpenko, J.M. Katzy, E. Yatsenko, K. Werner, *EPOS LHC: test of collective hadronization with LHC data* (Phys. Rev. C 92, 34906 (2015). doi:10.1103/PhysRevC.92.034906. arXiv:1306.0121 [hep-ph])

[22] S. Agostinelli et al., GEANT4 Collaboration, *GEANT4 – a simulation toolkit* (Nucl. Instrum. Methods A 506, 250 (2003). doi:10.1016/S0168-9002(03)01368-8)

[23] ATLAS Collaboration, *The ATLAS simulation infrastructure* (Eur. Phys. J. C 70, 823?874 (2010). doi:10.1140/epjc/s10052-010-1429-9. arXiv:1005.4568 [physics.ins-det])

[24] G. Piacquadio, K. Prokofiev, A. Wildauer, *Primary vertex reconstruction in the ATLAS experiment at LHC* (J. Phys. Conf. Ser. 119, 032033 (2008). doi:10.1088/1742-6596/119/3/032033)

[25] ATLAS Collaboration, *ATLAS Insertable B-Layer Technical Design Report*, (CERN-LHCC-2010-013. ATLAS-TDR-19 (2010), url: http://cdsweb.cern.ch/record/1291633, CERN-LHCC-2012-009. ATLAS-TDR-19-ADD-1)
ATLAS Collaboration, *ATLAS Insertable B-Layer Technical Design Report Addendum,* (CERN-LHCC-2012-009. ATLAS-TDR-19-ADD-1 (2012), Addendum to CERN-LHCC-2010-013, ATLAS-TDR-019, url: http://cdsweb.cern.ch/record/1451888)

[26] ATLAS Collaboration, *Track Reconstruction Performance of the ATLAS Inner Detector at* $\sqrt{s} = 13$ *TeV* (ATL-PHYS-PUB-2015-018 (2015), http://cdsweb.cern.ch/record/2037683)

[27] ATLAS Collaboration, *Studies of the ATLAS inner detector material using* $\sqrt{s} = 13$ *TeV pp collision data* (ATL-PHYS-PUB-2015-050 (2015) https://cds.cern.ch/record/2109010)

[28] ATLAS Collaboration, *Early inner detector tracking performance in the 2015 data at* $\sqrt{s} = 13$ *TeV* (ATL-PHYS-PUB-2015-051 (2015). https://cds.cern.ch/record/2110140)

[29] ATLAS Collaboration, *A study of the material in the ATLAS inner detector using secondary hadronic interactions* (JINST 7 (2012) P01013, arXiv:1110.6191 [hep-ex])

[30] ATLAS Collaboration, *A measurement of material in the ATLAS tracker using secondary hadronic interactions in 7 TeV pp collisions* (CERN-EP-2016-137, e-Print: arXiv:1609.04305 [hep-ex])

[31] G. D'Agostini, *A multidimensional unfolding method based on Bayes' theorem*. (Nucl. Instrum. Methods A 362, 487?498 (1995). doi:10.1016/0168-9002(95)00274-X)

Diphoton production in lead-lead and proton-proton UPC

M. Kłusek-Gawenda[1], A. Szczurek[1]*

[1]Institute of Nuclear Physics Polish Academy of Sciences, Radzikowskiego 152, PL-31-342 Kraków, Poland

Abstract

We discuss diphoton semi(exclusive) production in ultraperipheral $PbPb$ collisions at energy of $\sqrt{s_{NN}} = 5.5$ TeV (LHC). The nuclear calculations are based on equivalent photon approximation in the impact parameter space. The cross sections for elementary $\gamma\gamma \to \gamma\gamma$ subprocess are calculated including three different mechanisms: box diagrams with leptons and quarks in the loops, a VDM-Regge contribution with virtual intermediate hadronic excitations of the photons and the two-gluon exchange contribution (formally three-loops) to elastic photon-photon scattering in the high-energy approximation. We got relatively high cross sections in $PbPb$ collisions (306 nb). This opens a possibility to study the $\gamma\gamma \to \gamma\gamma$ (quasi)elastic scattering at the LHC. We find that the cross section for elastic $\gamma\gamma$ scattering could be measured in the lead-lead collisions for the diphoton invariant mass up to $W_{\gamma\gamma} \approx 15 - 20$ GeV. We identify region(s) of phase space where the two-gluon exchange contribution becomes important ingredient compared to box and nonperturbative VDM-Regge mechanisms. We perform a similar analysis for the $pp \to pp\gamma\gamma$ reaction at energy of $\sqrt{s_{NN}} = 7$ and 100 TeV.

*Also at University of Rzeszów, PL-35-959 Rzeszów, Poland.

1 Introduction

In classical Maxwell theory photons/waves/wave packets do not interact. In contrast, in quantal theory they can interact via quantal fluctuations. So far only inelastic processes, i.e. production of hadrons or jets via photon-photon fusion could be measured e.g. in e^+e^- collisions or in ultraperipheral collisions (UPC) of heavy-ions. It was realized only recently that ultraperipheral heavy-ions collisions can be also a good place where photon-photon elastic scattering could be tested experimentally [1, 2].

2 Theory

2.1 Elementary cross section

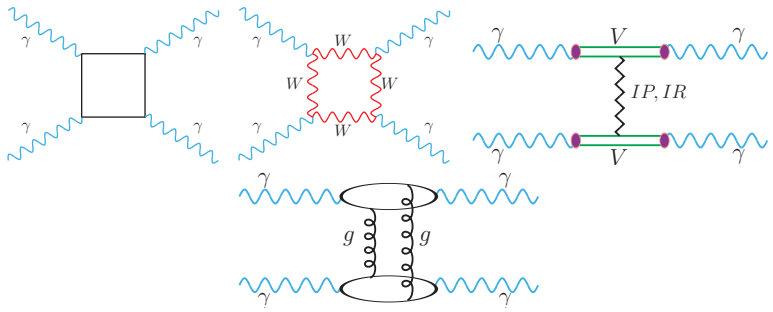

Figure 1: Light-by-light scattering mechanisms with the lepton and quark loops (first diagram) and for the intermediate W-boson loop (second diagram). Third diagram represents VDM-Regge mechanism and the last diagram is for two-gluon exchange.

One of the main ingredients of the formula for calculation of the nuclear cross section is elementary $\gamma\gamma \to \gamma\gamma$ cross section. The lowest order QED mechanisms with elementary particles are shown in two first diagrams of Fig. 1. The first diagram is for lepton and quark loops and it dominates at lower photon-photon energies ($W_{\gamma\gamma} < 2m_W$) while the next diagram is for the W (spin-1) boson loops and it becomes dominant at higher photon-photon energies ([3, 4]). The one-loop box amplitudes were calculated by using the Mathematica package `FormCalc` and the `LoopTools` library. We have obtained good agreement when confronting our result with those in [3, 5, 6]. Including higher-order contributions seems to be interesting. In Ref. [6] the authors considered both the QCD and QED corrections (two-loop Feynman diagrams) to the one-loop fermionic contributions in the ultrarelativistic limit ($\hat{s}, |\hat{t}|, |\hat{u}| \gg m_f^2$). The corrections are quite small numerically so the leading order computations considered by us are satisfactory. In the last two diagrams of Fig. 1 we show processes that are the same order in α_{em} but higher order in α_s. Third diagram presents situation where both photons fluctuate into virtual vector mesons (here we include three different light vector mesons: ρ, ω, ϕ). The last diagram shows two-gluon exchange mechanism which is formally three-loop type. Its contribution to the elastic scattering of photons at high energies has been first considered in the pioneering work [7]. Indeed in the limit where the Mandelstam

variables of the $\gamma\gamma \to \gamma\gamma$ process satisfy $\hat{s} \gg -\hat{t}, -\hat{u}$, major simplifications occur and the three-loop process becomes tractable. This corresponds to a near-forward, small-angle, scattering of photons In our treatment, we go beyond the early work [7] by including finite fermion masses, as well as the full momentum structure in the loops, and we consider all helicity amplitudes [8].

2.2 Nuclear cross section

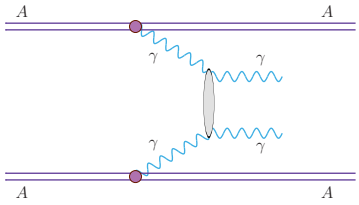

Figure 2: Diphoton production in ultrarelativistic UPC of heavy ions.

The general situation for the $AA \to AA\gamma\gamma$ reaction is sketched in Fig. 2. In our equivalent photon approximation (EPA) in the impact parameter space, the total (phase space integrated) cross section is expressed through the five-fold integral (for more details see e.g. [9])

$$\begin{aligned}\sigma_{A_1A_2\to A_1A_2\gamma\gamma}\left(\sqrt{s_{A_1A_2}}\right) &= \int \sigma_{\gamma\gamma\to\gamma\gamma}\left(W_{\gamma\gamma}\right) N\left(\omega_1, \mathbf{b_1}\right) N\left(\omega_2, \mathbf{b_2}\right) \\ &\times S^2_{abs}\left(\mathbf{b}\right) 2\pi b \mathrm{d}b\, \mathrm{d}\bar{b}_x\, \mathrm{d}\bar{b}_y \frac{W_{\gamma\gamma}}{2} \mathrm{d}W_{\gamma\gamma}\, \mathrm{d}Y_{\gamma\gamma}\ , \quad (1)\end{aligned}$$

where $N(\omega_i, \mathbf{b_i})$ are photon fluxes, $W_{\gamma\gamma} = \sqrt{4\omega_1\omega_2}$ and $Y_{\gamma\gamma} = \left(y_{\gamma_1} + y_{\gamma_2}\right)/2$ is a invariant mass and a rapidity of the outgoing $\gamma\gamma$ system. Energy of photons is expressed through $\omega_{1/2} = W_{\gamma\gamma}/2 \exp(\pm Y_{\gamma\gamma})$. $\mathbf{b_1}$ and $\mathbf{b_2}$ are impact parameters of the photon-photon collision point with respect to parent nuclei 1 and 2, respectively, and $\mathbf{b} = \mathbf{b_1} - \mathbf{b_2}$ is the standard impact parameter for the A_1A_2 collision.

The photon flux ($N(\omega, b)$) is expressed through a nuclear charge form factor. In our calculations we use two different types of the form factor. The first one, called here realistic form factor, is the Fourier transform of the charge distribution in the nucleus and the second one is a monopole form factor which leads to simpler analytical results. More details can be found e.g. in [2, 9].

2.3 $pp \to pp\gamma\gamma$ process

We can study the mechanism of elastic photon-photon scattering also in $pp \to pp\gamma\gamma$ reaction. In our calculations we neglect the gap survival factor. Then the cross section of $\gamma\gamma$ production in proton-proton collisions takes the simple parton model form

$$\frac{\mathrm{d}\sigma}{\mathrm{d}y_1 \mathrm{d}y_2 \mathrm{d}^2p_t} = \frac{1}{16\pi^2\hat{s}^2} x_1\gamma^{(el)}(x_1) x_2\gamma^{(el)}(x_2) \overline{|M_{\gamma\gamma\to\gamma\gamma}|^2}\ . \quad (2)$$

Here $y_{1/2}$ is the rapidity of final state photon, p_t is the photon transverse momentum and $x_{1/2} = p_t/\sqrt{s}\left(\exp\left(\pm y_1\right) + \exp\left(\pm y_2\right)\right)$. In the numerical calculations for

the elastic fluxes we shall use a practical parametrization of Ref. [10]. Detailed description of Eq. 2 one can be found in our paper [8].

3 Results

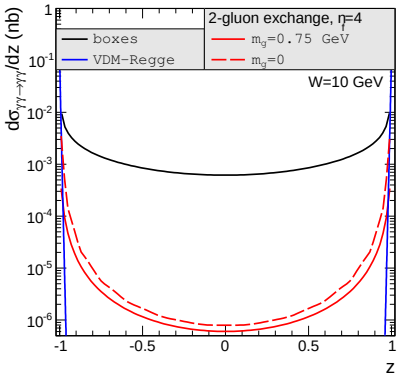

Figure 3: Statement of the three considered processes for $W = 10$ GeV.

In Fig. 3 we show contributions of mechanisms presented in Fig. 1 for fixed value of energy $W = 10$ GeV. The differential cross section is shown as a function of $z = \cos\theta$, where θ is the scattering angle in the $\gamma\gamma$ cms. The contribution of the VDM-Regge is concentrated at $z \approx \pm 1$. In contrast, the box contribution extends over a broad range of z. The two-gluon exchange contribution occupies intermediate regions of z. We need to add though, that the approximations made in the calculation of the two-gluon exchange are justified in a small angle region only. At small z the error can easily be 100%. In addition we show the difference between results when we include gluon mass ($m_g = 750$ MeV - solid line) and for massless particle ($m_g = 0$ - dashed line).

The elementary angle-integrated cross section for the box and VDM-Regge contributions is shown in the first panel of Fig. 4 as a function of the photon-photon subsystem energy. Lepton and quark amplitudes interfere enhancing the cross section. For instance in the 4 GeV $< W <$ 50 GeV region, neglecting interference effects, the lepton contribution to the box cross section is by a factor 5 bigger than the quark contribution. Interference effects are large and cannot be neglected. At energies $W > 30$ GeV the VDM-Regge cross section becomes larger than that for the box diagrams. The right panel of Fig. 4 shows results for nuclear collisions for the case of realistic charge density (red lines) and monopole form factor (blue lines). The difference between the results becomes larger with larger values of the kinematical variables. The cross section obtained with the monopole form factor is somewhat larger.

A lower cut on photon transverse momentum $p_t > 1$ GeV is necessary to get rid of the soft region where the VDM-Regge contribution dominates. In Ref. [8] we observed that the bigger distance between photons, the larger two-gluon to box contribution ratio is. Therefore we consider also a possibility to observe photons with forward calorimeters (FCALs). In Fig. 5 we show differential distribution as

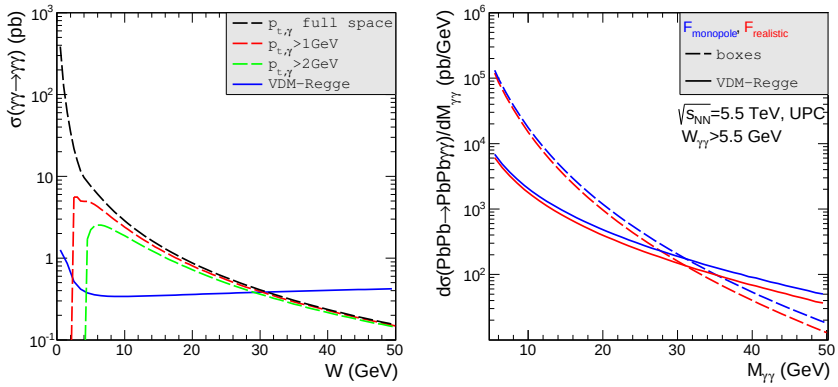

Figure 4: Elementary and nuclear cross section for light-by-light scattering. The dashed lines show the results for the case when only box contributions (fermion loops) are included and the solid lines show the results for the VDM-Regge mechanism. Left panel: integrated elementary $\gamma\gamma \to \gamma\gamma$ cross section as a function of the subsytem energy. Right panel: differential nuclear cross section as a function of $\gamma\gamma$ invariant mass at $\sqrt{s_{NN}} = 5.5$ TeV. The distributions with the realistic charge density are depicted by the red (lower) lines and the distributions which are calculated using the monopole form factor are shown by the blue (upper) lines.

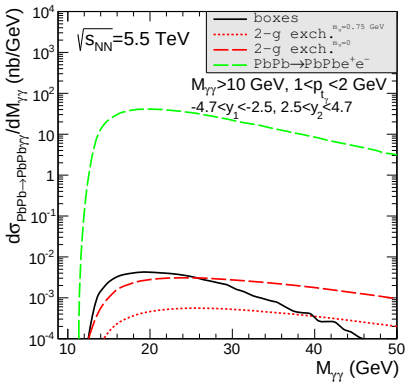

Figure 5: Distribution in invariant mass of photons for $M_{\gamma\gamma} > 10$ GeV, 1 GeV $< p_t <$ 2 GeV and $-4.7 < y_1 < -2.5$, $2.5 < y_2 < 4.7$. In addition, we show (top dashed, green line) a similar distribution for $AA \to AAe^+e$.

a function of invariant mass of photons. The results are shown both for box and two-gluon exchange mechanisms. For comparison we also show cross section for the $\gamma\gamma \to e^+e^-$ - subprocess. We emphasise that this subprocess is, however, a reducible background to the light-by-light scattering.

If we try to answer the question whether the reaction can be measured with the help of LHC detectors then we have to generalize Eq. (1) by adding extra integration over additional parameter related to angular distribution for the subprocess [2].

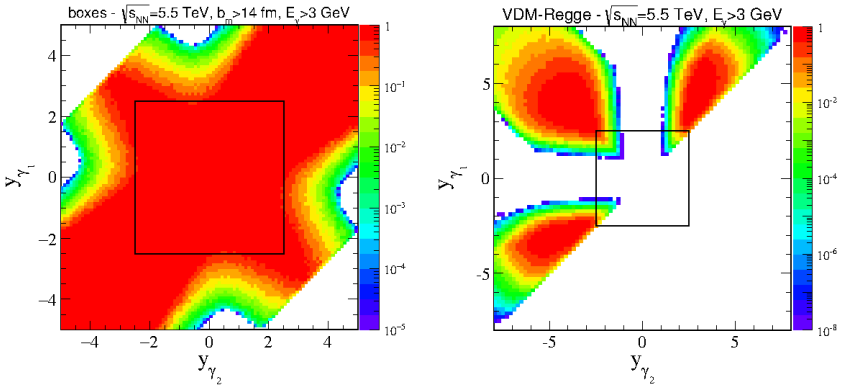

Figure 6: Contour representation of two-dimensional ($\mathrm{d}\sigma/\mathrm{d}y_{\gamma_1}\mathrm{d}y_{\gamma_2}$ in nb) distribution in rapidities of the two photons in the laboratory frame for box (left panel) and VDM-Regge (right panel) contributions. Nuclear calculations are done for $\sqrt{s_{NN}} = 5.5$ TeV.

Fig. 6 shows two-dimensional distributions in photon rapidities in the contour representation. The calculation was done at the LHC energy $\sqrt{s_{NN}} = 5.5$ TeV. Here we impose cuts on energies of photons in the laboratory frame ($E_\gamma > 3$ GeV). Very different distributions are obtained for boxes (left panel) and VDM-Regge (right panel). In both cases the influence of the imposed cuts is significant. In the case of the VDM-Regge contribution we observe as if non continues behaviour which is caused by the strong transverse momentum dependence of the elementary cross section (see Fig. 4 in Ref. [2]) which causes that some regions in the two-dimensional space are almost not populated. Only one half of the $(y_{\gamma_1}, y_{\gamma_2})$ space is shown for the VDM-Regge contribution. The second half can be obtained from the symmetry around the $y_{\gamma_1} = y_{\gamma_2}$ diagonal. Clearly the VDM-Regge contribution does not fit to the main detector ($-2.5 < y_{\gamma_1}, y_{\gamma_2} < 2.5$) and extends towards large rapidities. In the case of the VDM-Regge contribution we show much broader range of rapidity than for the box component. We discover that maxima of the cross section associated with the VDM-Regge mechanism are at $|y_{\gamma_1}|, |y_{\gamma_2}| \approx 5$. Unfortunately this is below the limitations of the ZDCs ($|\eta| > 8.3$ for ATLAS ([11]) or 8.5 for CMS ([12])).

The nuclear distribution in the diphoton invariant mass is shown in Fig. 7. The two-gluon distribution starts to dominante over the box contribution only above $M_{\gamma\gamma} > 50$ GeV for 1 GeV $< p_t < 2$ GeV. However, the cross section in this region is rather small. The situation for LHC (left panel) and for Future Circular Collider (FCC) energy (right panel) is rather similar. The dominance of the two-gluon exchange over the box contribution takes place more or less at the same diphoton invariant masses.

Finally in Fig. 8 we show numbers of counts in the 1 GeV intervals expected for assumed integrated luminosity: $L_{int} = 1$ nb^{-1} typical for UPC at the LHC. We have imposed cuts on photon-photon energy and (pseudo)rapidities of both photons. It looks that one can measure invariant mass distribution up to $M_{\gamma\gamma} \approx 15$ GeV.

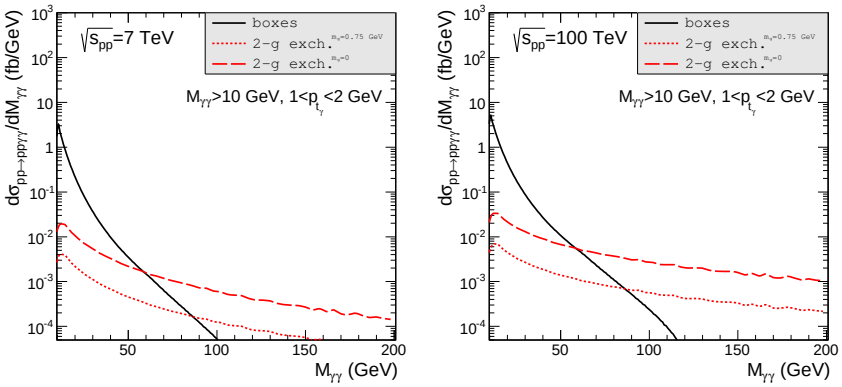

Figure 7: Distribution in invariant mass of the produced photons for $\sqrt{s_{pp}} =$ 7 TeV (LHC) and $\sqrt{s_{pp}} = 100$ TeV (FCC) for cuts on photon transverse momenta specified in the figure legend. No cuts on photon rapidities are applied here.

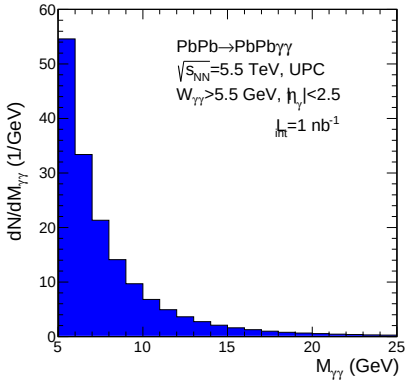

Figure 8: Distribution of expected number of counts in 1 GeV bins for cuts on $W_{\gamma\gamma} > 5.5$ GeV and $\eta_\gamma < 2.5$.

4 Summary

In our recent papers [2, 8] we have studied in detail how to measure elastic photon-photon scattering in ultrarelativistic ultraperipheral lead-lead collisions and in $pp \to pp\gamma\gamma$ reaction. The nuclear calculations were performed in an equivalent photon approximation in the impact parameter space. The calculation for proton-proton collisions were done as usually in the parton model with elastic photon distributions expressed in terms of proton electromagnetic form factors. The cross section for photon-photon scattering was calculated taking into account well known box diagrams with elementary standard model particles (leptons and quarks), a VDM-Regge component which was considered only recently [2] in the context of $\gamma\gamma \to \gamma\gamma$ scattering as well as a two-gluon exchange, including massive quarks, all helicity configurations of photons and massive and massless gluon. Several distributions in

different kinematical variables were calculated. For $AA \to AA\gamma\gamma$ and $pp \to pp\gamma\gamma$ reactions we identified regions of the phase space where the two-gluon contribution should be enhanced relatively to the box contribution. The region of large rapidity difference between the two emitted photons and intermediate transverse momenta 1 GeV $< p_t < 2 - 5$ GeV seems optimal in this respect.

Using the monopole form factor we get similar cross section to that found in [1] (after the correction given in Erratum of [1]). Nevertheless, we think that application of realistic charge distribution in the nucleus gives more precise results. We have shown an estimate of the counting rate for expected integrated luminosity. We expect non-zero counts for subprocess energies smaller than $W_{\gamma\gamma} \approx$ 15-20 GeV.

We have considered also an option to measure both photons by the forward calorimeters. It is rather difficult to distinguish photons from electrons in FCALs. In heavy-ion collisions, in addition, the cross section for $AA \to AAe^+e^-$ is huge, so this option seems not realistic. In $pp \to pp\gamma\gamma$ case the corresponding background would be smaller but the signal is also reduced.

Recently, the ATLAS Collaboration published a note [13] about evidence for light-by-light scattering signatures in quasi-real photon interactions from ultraperipheral lead-lead collisions at $\sqrt{s_{NN}} = 5.02$ TeV. The data set was recorded in 2015 and corresponds to 480 μb. The measured fiducial cross section which includes limitation on photon transverse momentum, photon pseudorapidity, diphoton invariant mass, diphoton transverse momentum and diphoton acoplanarity, has been measured to be 70 ± 20 (stat.) ± 17 (syst.) nb, which is compatible with our predicted value of 49 ± 10 nb.

References

[1] D. d'Enterria and G. G. da Silveira, Phys. Rev. Lett. 111 (2013) 080405, Erratum: Phys. Rev. Lett. 116 (2016) 129901,

[2] M. Kłusek-Gawenda, P. Lebiedowicz and A. Szczurek, Phys. Rev. **C93** (2016) 044907,

[3] D. Bardin, L. Kalinovskaya and E. Uglov, Phys. Atom. Nucl. **73** (2010) 1878,

[4] P. Lebiedowicz, R. Pasechnik and A. Szczurek, Nucl. Phys. **B881** (2014) 288,

[5] G. Jikia and A. Tkabladze, Phys. Lett. **B323** (1994) 453,

[6] Z. Bern, A. De Freitas, L. J. Dixon, A. Ghinculov and H. L. Wong, J. High Energy Phys. 11 (2001) 031,

[7] I. F. Ginzburg, S. L. Panfil and V. G. Serbo, Nucl. Phys. **B284** (1987) 685,

[8] M. Kłusek-Gawenda, W. Schäfer and A. Szczurek, Phys. Lett. **B761** (2016) 399,

[9] M. Kłusek-Gawenda and A. Szczurek, Phys. Rev. **C82** (2010) 014904,

[10] M. Drees and D. Zeppenfeld, Phys. Rev. **D39** (1989) 2536,

[11] P. Jenni, M. Nessi and M. Nordberg, Report No. LHCC-I-016, CERN-LHCC-2007-001,

[12] O. A. Grachov et al. (CMS Collaboration), J. Phys. Conf. Ser. 160 (2009) 012059,

[13] The ATLAS collaboration, *Light-by-light scattering in ultra-peripheral Pb+Pb collisions at* $\sqrt{s_{NN}} = 5.02$ *TeV with the ATLAS detector at the LHC* (ATLAS-CONF-2016-111).